DEVELOPMENT OF A NOVEL HIGH PERFORMANCE ELECTROLYTE SUPPORTED SOLID OXIDE FUEL CELL

by

Paul Steven Gentile

A thesis submitted in partial fulfillment
of the requirements for the degree

of

Master of Science

in

Mechanical Engineering

MONTANA STATE UNIVERSITY
Bozeman, Montana

November 2007

© COPYRIGHT

by

Paul Steven Gentile

2007

All Rights Reserved

APPROVAL

of a thesis submitted by

Paul Steven Gentile

This thesis has been read by each member of the thesis committee and has been found to be satisfactory regarding content, English usage, format, citation, bibliographic style, and consistency, and is ready for submission to the Division of Graduate Education.

Stephen W. Sofie, Ph.D.

Approved for the Department of Mechanical Engineering

Christopher H. M. Jenkins Ph. D.

Approved for the Division of Graduate Education

Dr. Carl A. Fox

STATEMENT OF PERMISSION TO USE

In presenting this thesis in partial fulfillment of the requirements for a master's degree at Montana State University, I agree that the Library shall make it available to borrowers under rules of the Library.

If I have indicated my intention to copyright this thesis by including a copyright notice page, copying is allowable only for scholarly purposes, consistent with "fair use" as prescribed in the U.S. Copyright Law. Requests for permission for extended quotation from or reproduction of this thesis in whole or in parts may be granted only by the copyright holder.

Paul Steven Gentile

November 2007

ACKNOWLEDGEMENTS

I would like to express my deep and sincere gratitude to Dr. Stephen W. Sofie for his generosity, guidance and support throughout my research. His enthusiasm for advanced research of engineered ceramics, extensive knowledge base and continuous encouragement proved to be an invaluable inspiration. My gratitude also goes to Dr. Alexandre Lussier, Dr. Max Deibert, Dr. Richard Smith, Dr. Paul Gannon and the entire MSU HiTec Fuel Cell Research Group for their innovative ideas, feedback and support throughout my tenure. The assistance from this diverse team of engineers and physicists was irreplaceable.

My appreciation extends to the entire staff of the Department of Mechanical and Industrial Engineering, as well as to my fellow graduate students. I would also like to thank Dr. Chris Jenkins and Dr. Ahsan Mian for their support as committee members. This work was supported by the US Department of Energy.

TABLE OF CONTENTS

1. INTRODUCTION....1

Fuel Cell Research Motivation....1
UniCell Development....2
Ceramic Processing....2
Analytical Techniques....2
Experimental Overview....3
Results Summary....4

2. BACKGROUND....6

Fuel Cell Overview....6
Unit Fuel Cell....6
Interconnect....9
Balance of Plant....9
Solid Oxide Fuel Cells....10
SOFC Advantages....11
SOFC Design Challenges....13
SOFC Applications....14
SOFC Electrochemical Performance....14
Gibbs Free Energy & the Nernst Potential....16
Polarization Effects....18
SOFC Efficiency....21
SOFC Operation Variables:....23
SOFC Unit Cell Components....25
Anode....25
Cathode....26
Electrolyte....27
SOFC Unit Cell Architectures....29
Planar Anode Supported Cell (ASC):....30
Planar Electrolyte Supported Cell (ESC):....31
Tubular SOFC:....32
Planar Metallic Bi-Polar Plate Supported:....33
Micro Tubular SOFC:....34
Engineering of Advanced Ceramics....35
Ceramic Powders....36
Uniaxial Dry Pressing:....37
Electrolyte Slurry....39
Solvent....39
Dispersant or Deflocculant....40
Binder....41
Plasticizers....42

TABLE OF CONTENTS - CONTINUED

Organic Interactions....44
Ball Milling....45
Slurry De-Airing....47
Tape Casting....48
Equipment....49
Physics & Procedures....51
Drying....54
Surface Contouring....56
Laser Micromachining....56
Photoresist Machining (PRM)....60
Alternative Methods Considered....61
Firing Process....61
Pre-Sinter Firing Stage....62
Solid State Sintering....63
Ceramic Mechanical Properties....64
Ceramic Bonding....65
Mechanical Failure....65
Ceramic Microstructure....67
Analysis Techniques....68
Field Emission Microscopy (FEM)....68
Thermal Gravitational Analysis (TGA)....69
Dilatometer Analysis....69
Instron Materials Testing Machine....70
Fuel Cell Performance Testing....70

3. UNICELL DESIGN....71

Problem Overview....71
Design Approach & Concept....71
Design Objectives....71
Minimize Area Specific Resistance....71
Minimize Activation Polarization....72
Minimize Concentration Polarization....73
Design Constraints....73
Provide Adequate Mechanical Strength....73
Permit Feasible Fabrication....74
SECA SOFC Design Specifications....74
Design Alternatives....74
Interleaved Hole Pattern....75
Interleaved Channels....76

4. EXPERIMENTAL PROCEDURE....81

TABLE OF CONTENTS - CONTINUED

Experimental Problem Definition 81
Particle Dispersion Sedimentation Study 81
Sintering Study....82
Effect of Maximum Sintering Temperature on Microstructure 82
Sintering Pressure....87
Tape Cast Optimization Studies....88
Starting Materials 88
Slurry Preparation....89
Tape Casting....89
Thermal Gravimetric Burnout Study....90
Dilatometer Studies 91
Surface Contouring Investigation 92
Mechanical Strength Study....93
ESL 3 mol % YSZ Samples....94
MSU YSZ Samples 94
Concentric Ring Sample Holder 95
Test Procedure....97
Calculation of Results....98
Fuel Cell Performance Study....99
Sample Punching....99
Sintering....99
Electrode Application....99
Fuel Cell Test Stand 100
Solid Oxide Unit Cell Mounting 101
Operating Conditions....102

5. RESULTS & DISCUSSION 104

Particle Dispersion Sedimentation Study 104
Sintering Study....106
LSM Sintering Study....106
YSZ Sintering Study....111
Tape Sintering Study 114
Tape Cast Optimization....116
Dilatometer Studies 119
Thermal Gravimetric Burnout Study....122
Surface Contouring 126
Interleaved Hole Patterns....126
Interleaved Concentric Channels....129
Single Sided Linear Channels 132
Mechanical Strength Study....133
Preliminary Data....133

TABLE OF CONTENTS - CONTINUED

Reported Data....134
Fuel Cell Performance Study....138

6. CONCLUSION....144

Results Summary....144
Future Considerations & Recommendations....147

BIBLIOGRAPHY....151

APPENDIX A: Concentric Ring Machine Shop Drawings....156

LIST OF TABLES

Table Page

1. Fuel Cell Type Overview [(1)] 8
2. SOFC Half Cell Reaction Equations 15
3. Channel Surface Area Comparison 79
4. Electrolyte Tape Concentrations 88
5. Tape Recipe Used for TGA Study 91
6. Surface Contour Methods Explored 92
7. MSU Concentric Ring Samples 95
8. Fuel Cell Testing Temperature Profile 103
9. Fuel Cell Testing Operating Conditions 103
10. Boiling Point of Organic Constituents in MSU YSZ Tape 124
11. Equibiaxial Strength Test Conditions and Results 137
12. Fuel Cell Performance Test Results 139

LIST OF FIGURES

Figure Page

1. Fuel Cell Stack Diagram....6
2. Schematic of the Unit Fuel Cell [1] 7
3. Rudimentary fuel cell system schematic [1] 10
4. Subsystem comparison of SOFC versus PEM....11
5. Electrical efficiency comparison [2] 12
6. Solid oxide fuel cell schematic [3]....15
7. Gibbs Free Energy Change of Reaction 17
8. Fuel Cell V-I Curve [1] 19
9. ASR of YSZ Electrolytes as a Function of Temperature 21
10. Thermodynamic Efficiency of Reactants at Elevated Temperatures [5] 22
11. Fuel Utilization vs. Cell Efficiency [1] 23
12. Power Curve Demonstrating Peak Power vs. Current Density....24
13. Phase Diagram of YSZ [6] 27
14. Pure Zirconia and Partially Stabilized Zirconia Lattice Diagrams....28
15. Planar fuel cell design....29
16. Tubular fuel cell design [7] 29
17. Anode supported SOFCs [9]....31
18. Hionic™ electrolyte supported SOFC [10] 31
19. Tubular SOFC Design [7] 32
20. Tubular SOFC Process [11] 32
21. Tubular Fuel Cell Design (7) 33
22. Argonne National Lab's TuffCell (13) 34

LIST OF FIGURES - CONTINUED

Figure Page

23. Portable Micro-Tubular SOFC [14] 34
24. UniCell Electrolyte with Interleaved Channels 35
25. Uniaxial Dry Press 3 Stage Compaction Process [16] 38
26. Stress Strain Curve Plasticizer Comparison [15] 43
27. Tape Casting Schematic [15] 48
28. Double Doctor Blade Assembly [15] 49
29. Laser Pulse in Dense Ceramic Substrate [19] 57
30. Laser Pulse in Green Ceramic Substrate [19] 58
31. Photoresist machining etching nozzle diagram 60
32. Photoresist machining station[21] 60
33. Photoresist Texturing of Alumina Substrates [21] 61
34. UniCell Ultimate Design Parameters Diagram 72
35. UniCell Linear Interleaved Hole CAD Model 75
36. UniCell Interleaved Hole Patterns (Left: Linear & Right: Checkerboard) 76
37. UniCell Channels Designs 77
38. Channel Design Detail Views 77
39. UniCell Channel Ionic Path Diagram 77
40. Seal Area Neglecting in Surface Area Calculations 79
41. Sintering Cycle Temperature Profile (1400 °C) 85
42. Linear Intercept Method 87
43. FEM Image of Electrolyte Displays a Macroscopically Isotropic Material after Sintering 94

LIST OF FIGURES - CONTINUED

Figure Page

44. Section View of Basic Fixturing and Test Specimen for Equibiaxial Testing [25] 96

45. Illustrations of Failure Patterns in Concentric Ring Test Specimens [25] 98

46. Fuel Cell Test Rig Furnace and Mass Flow Controllers....101

47. Fuel Cell Test Rig Inconel Platens 102

48. MFO Particle Dispersion Specimens After 66 hours 105

49. MFO Particle Dispersion Specimens After 18 (left) & 24 (right) Hours 105

50. FEM Images of Inframat LSM 40 Micron Spherical Granules (Left 250 X & Right 2,500 X Magnifications)....107

51. FEM Images of NexTech LSM 100 Micron Spherical Granules (Left 250 X & Right 5,000 X Magnifications)....107

52. LSM Geometric vs. Archimedes Density Measurements Comparison 108

53. Relative Densities of LSM Pellets Sintered from 1100 – 1400 °C as a Function of Granule Size 109

54. Grain Size in LSM Pellets Sintered from 1100 – 1400 °C as a Function of Granule Size 110

55. FEM Image of the Microstructure of NexTech LSM Sintered at 1300 °C....110

56. FEM Image of YSZ Micron (Left) and Nano (Right) Particles at 5,000 X....111

57. Relative Densities of YSZ Pellets Sintered from 1100 – 1550 °C as a Function of Particle Size....112

58. FEM Images of Nano YSZ Powders Sintered at 1100, 1300 and 1400 °C 112

59. FEM Images of Micro YSZ Powders Sintered at 1300, 1350, 1400, 1450, 1500 & 1550 °C....113

60. Grain Size in YSZ Pellets Sintered from 1100 – 1550 °C as a Function of Particle Size....114

LIST OF FIGURES - CONTINUED

Figure Page

61. Sintering Shrinkage of YSZ Electrolyte Tape 115

62. Micro YSZ Tape Cast Specimens Sintered at 1400 (top left), 1450 (top right), 1500 (bottom left) & 1550 (bottom right) °C 115

63. FEM Images of Linear Laser Drilled Fracture Caused During Sintering Due to Excess Pressure 116

64. Shrinkage during Tape Drying 118

65. YSZ Micro Particle Pellets Dilatometer Sintering Study from 1200 to 1500 °C 120

66. YSZ Nano Particle Pellets Dilatometer Sintering Study from 1200 to 1400 °C 120

67. Sintering Shrinkage Rate as a Function of Temperature 121

68. Dilatometer measurement of YSZ CTE up to 800 °C 122

69. TGA Curves of YSZ Electrolyte Tapes at Varying Sintering Temperature Profiles 123

70. TGA Optimized 24 Hour Sintering Temperature Profile 124

71. TGA Curves of Organic Burnout Rates in Electrode Inks at the Utilized Co-Sintering Rate 125

72. FEM Top Views of Blind Holes Laser Drilled in A Sintered Disc Reference # (1) Top Left (2) Center (3) Right (4) Bottom Left (5) Center (6) Right 126

73. FEM Images of the Linear Interweaving Pattern of Blind Holes in a Green Electrolyte Tape via Laser Pulsing and CNC Controlled Translation 128

74. FEM Top & Cross Sectional Views of a Blind Hole Laser Drilled in Green Electrolyte Tape 128

75. Digital (Left) and Optical 50X (Right) Images of Green UniCell Electrolyte with Concentric Channels Prior to Initial 129

LIST OF FIGURES - CONTINUED

Figure Page

76. Cross Section of Concentric Channel Features in the Complete UniCell Including Electrodes (Anode on Left) After Co-Sintering and Electrochemical Testing (From top left to bottom right: Magnifications 22 and 75, 150 and 200) 130

77. Digital Images of UniCell LSM Cathode (Left) and Ni-YSZ Anode (Right) Prior to Co-sintering 131

78. FEM Images of the Top of the Anode Side Channels Post Electrochemical Testing (75, 5,000 and 10,000 Magnifications) 131

79. FEM Images of the Bottom of the Anode Side Channels Post Electrochemical Testing (100, 5,000 and 10,000 Magnifications) 131

80. FEM Images of the Top of the Cathode Side Channels Post Electrochemical Testing (100, 500 and 5,000 Magnifications) 132

81. FEM Images of the Top of the Cathode Side Channels Post Electrochemical Testing (100, 500 and 5,000 Magnifications) 132

82. FEM Images of the UniCell Cross Section (Left), Cathode/Electrolyte (Center) and Electrolyte/Anode (Right) Interfaces after Electrochemical Testing 132

83. FEM Cross Section of Linear Channels Laser Drilled in a Green Electrolyte (23, 100 & 239 Magnifications) 133

84. Monotonic Equibiaxial Flexural Strength of MSU 8 mol % YSZ Electrolyte Tape 134

85. Concentric Ring 8 mol % Flexural Strength Test Data Distribution....135

86. Monotonic Equibiaxial Flexural Strength of ESL 3 mol % YSZ Electrolyte Tape 135

87. Stress - Strain Curve of MSU 8 mol% Electrolyte Tape Obtained via Concentric Ring Equibiaxial Strength Test 136

88. UniCell Power Density 139

89. Commercial Indec ESC FC Performance Tests 140

LIST OF FIGURES - CONTINUED

Figure Page

90. MSU 100 Micron Thick ESC FC Performance Tests 141

91. MSU 400 Micron Thick ESC FC Performance Tests 142

LIST OF EQUATIONS

Equation Page

1. Gibbs Free Energy [4] 16
2. Unit Cell Reaction 16
3. Unit Cell Gibbs Free Energy Balance 17
4. Gibbs Free Energy Change of Reaction [1] 17
5. Maximum Electrical Work [1] 17
6. Nernst Equation [4] 18
7. SOFC Voltage 18
8. Ohm's Law 20
9. Internal Cell Resistance 20
10. Area Specific Resistance 20
11. Ideal Fuel Cell Efficiency 21
12. Voltage Efficiency 22
13. Cell Efficiency 23
14. Solids Loading 46
15. Reservoir Hydrostatic Pressure 53
16. Ionic Path Distance through the Bottom of UniCell Channels 78
17. Ionic Path Distance through the Walls of UniCell Channels 78
18. Path Area of the UniCell Channel Wall per Unit Thickness 78
19. Path Area of UniCell Channel Floor per Unit Thickness 78
20. Total UniCell Path Area per Unit Thickness 78
21. Normalized Ionic Path Distance through UniCell Electrolyte 78

LIST OF EQUATIONS - CONTINUED

Equation Page

22. Percentage Surface Area Increase 79
23. Surface Area Ratio 79
24. Geometric Density.....85
25. Relative Density 86
26. Achimedes Volume 86
27. Achimedes Density.....86
28. Equibiaxial Strength of a Circular Plate in a Concentric Ring Load Test [25].....99

NOMENCLATURE

AFC	Alkaline Fuel cell
A_{floor}	Path Area of UniCell Channel Floor per Unit Thickness
APU	Auxiliary Power Unit
ASC	Anode Supported Cell
ASR	Area Specific Resistance
A_{total}	Total Path Area of UniCell Channels per Unit Thickness
A_{wall}	Path Area of UniCell Channel Wall per Unit Thickness
CH_4	Methane
CHP	Combine Heating & Power
CO	Carbon Monoxide
CO_2	Carbon Dioxide
CTE	Coefficient of Thermal Expansion
D	Concentric Test Sample Diameter (mm)
D_L	Concentric Load Ring Diameter (mm)
D_s	Concentric Support Ring Diameter (mm)
DTA	Differential Thermal Analysis
e^-	Electron
E	Ideal Cell Potential Voltage
ESC	Electrolyte Supported Cell
E_{SOFC}	SOFC Voltage
F	Concentric Breaking Load (N)

F ..... Faraday's Constant (96,487 Coulombs/(mole of electrons))

FEM ..... Field Emission Microscopy

h ..... Concentric Test Sample Height (mm)

H_2 ..... Hydrogen

HAV ..... Heat Affected Zone

i ..... Current Through the Unit Cell

KD-1 ..... Polyester/Polyamide Copolymer Dispersant

LHV ..... Lower Heating Value

LSM ..... Lanthanum Manganese Oxide Doped with Strontium

MCFC ..... Molten Carbonate Fuel Cell

MFO ..... Menhaden Blown Fish Oil

n ..... Number of Electrons

$O^{=}$ ..... Oxygen Ion

O_2 ..... Oxygen

OCV ..... Open Circuit Voltage

PAFC ..... Phosphoric Acid Fuel Cell

Path ..... Approximate Ionic Path Length through UniCell Electrolyte

PEM ..... Polymer Exchange Membrane

PRM ..... Photoresist Machining

R ..... Universal Gas Constant [8.314 $J*K^{-1}*mol^{-1}$]

$R_{contact}$ ..... Contact Cell Resistance

$R_{electronic}$ ..... Electronic Cell Resistance

R_{ionic} ..... Ionic Cell Resistance

R ..... Total Cell Resistance

SEM ..... Scanning Electron Microscope

SOFC ..... Solid Oxide Fuel Cell

T ..... Temperature

$t_{bot_channels}$ ..... Thickness of Material at Bottom of UniCell Electrolyte Channels

T_g ..... Glass Transition Temperature

TGA ..... Thermal Gravitational Analysis

t_{wall} ..... Thickness of Material in Walls of UniCell Electrolyte Channels

VDW ..... van der Waals Force

YSZ ..... Yttria Stabilized Zirconia

δ_e ..... Electrolyte Thickness

ΔG ..... Gibbs Free Energy

ΔG° ..... Gibbs Free Energy of Reaction

ΔH ..... Enthalpy Change

ΔS ..... Entropy Change

η_{act} ..... Activation Polarization Losses (V)

η_{cell} ..... Overall Cell Efficiency

η_{conc} ..... Concentration Polarization Losses (V)

η_{ideal} ..... Ideal Thermodynamic Efficiency

η_{ohm} ..... Ohmic Polarization Losses (V)

η_{volt} ..... Cell Voltage Efficiency

σ_e ..... Electrolyte Ionic Conductivity

σ_f ..... Equibiaxial Strength (MPa)

υ ..... Poisson's Ratio

ABSTRACT

High power solid oxide fuel cell (SOFC) stacks are based on the planar design concept to yield high specific power densities. The key engineering challenges to planar stack reliability and robust operation is attaining low resistance interconnection of individual cells in series and hermetic sealing of interconnects. While stack design and contact paste development is paramount to address this issue, the basic design of the fuel cell introduces limitations. State-of-the-art anode supported cells (ASC) yield high power densities due to low ASR thin electrolytes, however, the asymmetrical design, anode/electrolyte CTE mismatch, and thick support anode yields undesirable cell camber and fuel transport issues. These deficiencies lead to poor interconnect contact, non-optimal sealing surfaces, and poor fuel utilization, which can mitigate the key benefit of the ASC. Conversely, the electrolyte supported cell (ESC) presents a host of advantages from ease of processing, large diameter scale-up potential, mechanical robustness, optimal seal contact surface, thin electrodes, and minimal cell curvature with the key obstacle arising from high cell ASR due to the thick structural electrolyte.

MSU has developed a novel cell concept that merges the benefits of the ASC and ESC designs. The "UniCell" concept has been designed to effectively lower the ASR of thick electrolyte supports while maintaining the traditional advantages of the ESC technology utilizing innovative, post ceramic processed, engineering techniques. SOFC fabrication methods of the electrolyte substrate established on xylene/ethanol solvent based yttria stabilized zirconia (YSZ) slurry include thin film tape casting and high temperature sintering. Photo-resist machining and laser drilling of interleaved electrolyte texture introduced into both surfaces of the YSZ green tapes and sintered substrates have been investigated. The findings of a dispersion study, thermo gravitational analysis performed to minimize microstructure defects due to rapid organic burnout, dilatometer investigation of sintering shrinkage and FEM microstructure analysis of electrolytes will be discussed. Mechanical strength testing via concentric ring on ring tests, and fuel cell performance data will be reported and compared to an ESC baseline to establish the feasibility of this concept. Alternative methods explored to introduce features during ceramic processing to reduce the process cost will be reviewed.

INTRODUCTION

Fuel Cell Research Motivation

A fuel cell electrochemically converts fuel and an oxidant into electrical energy without combustion. Several advantages of fuel cells have inspired extensive fundamental and industrial research and development. The electrochemical conversion produces near zero undesirable products such as NO_x, SO_x, particulate emissions and noise pollution. Fuel cells have no moving parts, reducing the likelihood of mechanical failure and yielding the potential for highly reliable and long-lasting systems. Fuel cell systems include the added advantages of quietly running 24 hours a day with the capacity to be compactly installed where wind turbines or solar panels often cannot. Designated onsite SOFC power generation systems eliminate the dependence on grid availability.

Fuel cells are capable of being run on pure hydrogen, eliminating all byproducts waste. However hydrogen is never found in nature in its elemental form, instead it must be decomposed from compounds that are found in nature which contain hydrogen, such as water (H_2O). This decomposition process requires energy input into the system. Therefore hydrogen is only an energy carrier, not an energy source.

Several traditional fossil and renewable fuels which include hydrocarbons are being considered as the energy source for fuel cells. Due to the high operating temperatures, solid oxide fuel cells (SOFCs) are fuel flexible, capable of internally reforming a wide variety of hydrocarbon based fuels such as liquefied natural gas, pipeline natural gas, coal syngas, methanol, propane and biogases. Stationary fuel cell systems with heat recovery have

demonstrated efficiencies up to 85% LHV[(1)], a drastic improvement over combustion technology because they are not limited by thermodynamics limitations of heat engines such as the Carnot efficiency.

UniCell Development

The development of a novel SOFC unit cell utilizing post ceramic processing techniques designed to improve the power density was explored. Fabrication of the unit cells required investigation and optimization of the ceramic processing and post processing techniques. Several experiments were conducted utilizing state of the art analysis equipment to study the effects of varying the processing parameters. The fabrication of a UniCell proof of concept model was successfully completed, and electrochemical test results reported show further investigation and optimization is warranted.

Ceramic Processing

The SOFC electrolyte layer provides mechanical support for the electrodes in the UniCell design. To create this base layer the electrolyte slurry was prepared and ball milled. The slurry was cast into a sub-millimeter thick, flexible green tape via standard tape casting techniques. The green tapes were sintered at high temperatures in a furnace utilizing silicon carbide elements to reach temperatures up to 1550°C. Thin anode and cathode electrode layers were applied on the electrolyte employing aerosol spray techniques and then the entire unit cell was co-sintered.

Analytical Techniques

Extensive optimization of the fabrication techniques was required to develop a working model. The following state of the art analytical techniques described were all employed during

the fabrication of the UniCell. Field emission microscopy (FEM) with energy dispersive x-ray spectroscopy was utilized to map the surface of materials. Thermal gravitational analysis technology highly accurately measured the weight gain and loss of samples throughout a temperature cycle due to effects such as organic burnout. A dilatometer measured the change in sample length during thermal cycles due to sintering shrinkage and thermal expansion effects. An Instron equipped with a concentric ring sample mount accurately measured the maximum brittle failure strength of ceramics. The electrochemical performance of fuel cells was characterized based on the voltage, amperage and power outputs as a function of temperature and gas flow rates.

Experimental Overview

A dispersion study was conducted to characterize the effectiveness of two different dispersant agents at several different concentration levels. A comprehensive sintering study correlated the yttria stabilized zirconia (YSZ) particle size and maximum sintering temperature to the grain formation, necessary for SOFC fabrication. FEM allowed the characterization of the microstructure.

Several tape casting methodology studies were conducted throughout the entire development process. One study measured the effects of binders and plasticizer concentrations on the flexibility, strength and profile of tape casts. The solids loading levels were experimentally varied to maximize the green tape density, which in turn minimized cell curvature, shrinkage and CTE stresses in the unit cell. Several tape cast parameters were systematically varied to obtain a consistent thickness profile of the green tape and ensure post processing was possible.

A thermal gravimetric study was performed to measure burnout rates of the organics in the electrolyte tapes as a function of sintering cycle profile in attempt to reduce the likelihood of forming internal voids for which cracks can be initiated. Dilatometer experiments calculated the shrinkage of green tapes during sintering and the coefficient of thermal expansion (CTE) of sintered samples at standard fuel cell operating temperatures. The mechanical brittle failure strength of electrolytes was characterized with a custom fabricated concentric ring mounting apparatus on an Instron. Finally electrochemical performance of the UniCell operated on hydrogen was characterized with a single cell SOFC test stand.

Results Summary

Tape casting of SOFC electrolytes is complex in nature due to the extensive list of variables which can drastically affect the end product. The broad range of experiments conducted has resulted in the ability to produce a more consistent end product. However it is clear that several factors which are either difficult or impossible to control in a laboratory setting can have undesired and unpredictable affects on the tape.

The optimization of the thermal sintering cycles through several TGA and dilatometer studies resulted in the ability to consistently produce an electrolyte supported cell with minimum cell curvature and voids. The cell's mechanical integrity and durability was improved due to the elimination of the internal stresses caused by the cell curvature. Mechanical strength testing was not conducted on the UniCell due to fabrication costs and the destructive nature of this test. However electrolyte layers without the post processing modifications were studied and the consistency of these results exceeds those obtainable through a simple three point bending test investigated.

Fuel cell performance was characterized for a set of single cell samples fabricated out of the UniCell electrolyte without post processing modifications. A comparison with the UniCell sample demonstrated the potential benefits of post processing, warranting further investigation. A commercial ESC sample was evaluated to serve as an industry performance comparison.

BACKGROUND

Fuel Cell Overview

A fuel cell system consists of the fuel cell stack(s) and the balance of plant equipment. The unit cell, consisting of the anode, electrolyte and cathode, is the fundamental fuel cell building block. Unit cells are combined in series with interconnect plates to form a fuel cell stack. These fuel cell stacks are then arranged in series and parallel to achieve the desired output voltage and power, respectively.

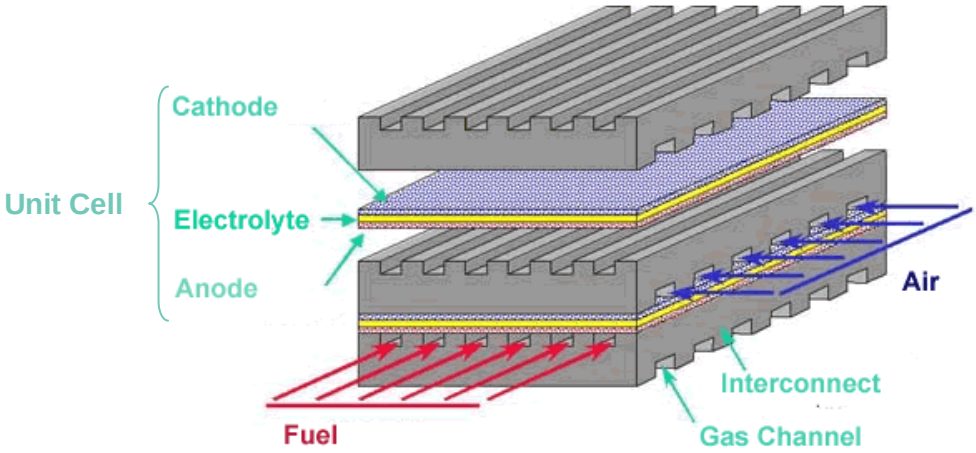


Figure 1 Fuel Cell Stack Diagram

The remaining fuel cell system components are commonly referred to as the balance of plant equipment. These items provide functions such as thermal management, fuel conditioning and electric power conditioning. They are all parasitic loads on the fuel cell, consuming power output from the stack to operate and reducing the system's overall efficiency.

Unit Fuel Cell

The smallest building block of a fuel cell system, the unit cell, is comprised of a three layer membrane where the electrochemical reactions take place. The electrolyte layer is

sandwiched between the anode and cathode. The simplest scenario to explore is a fuel cell operated on pure hydrogen and oxygen. The hydrogen fuel is introduced on the anode side and the oxygen is introduced on the cathode side. In the anode the hydrogen fuel is catalyzed into protons (hydrogen ions) and electrons. The electrons flow out of the negatively charged anode, through an external electrical circuit to power a load and then are reintroduced in the cathode where they react with the oxygen molecules.

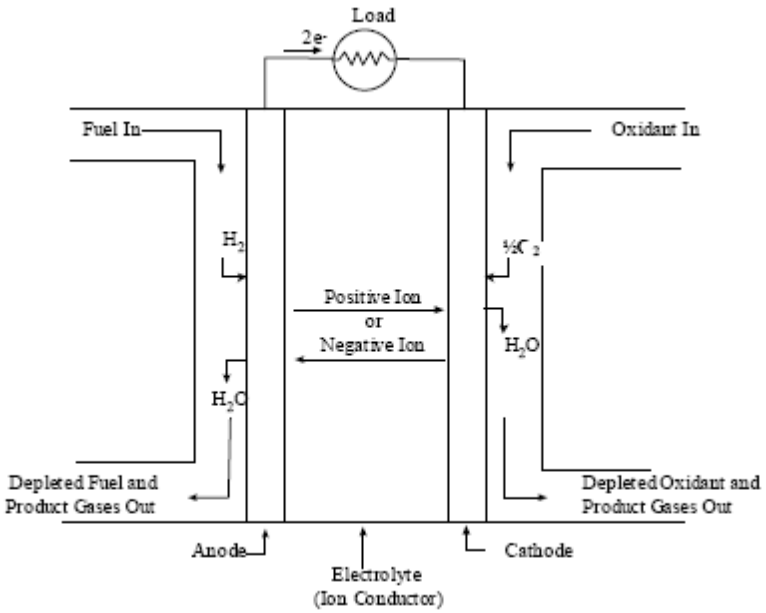


Figure 2 Schematic of the Unit Fuel Cell [(1)]

The electrolyte is an ionic conductor, where positive ionic conductors transport the hydrogen ions across the membrane from the anode to the cathode and negative ionic conductors transport the oxygen ions from the cathode to the anode. In a fuel cell with a negative ionic conductor for the electrolyte layer, the oxidant reacts with the extra electrons in the cathode allowing it then to be conducted as a negatively charged ion across the electrolyte. The oxygen ions react with the hydrogen ions at the anode – electrolyte interface (commonly referred to as

the three phase boundary) to create water as the only byproduct. If the electrolyte is a proton conductor the hydrogen ion is transported across to the cathode to react with the oxygen and create water byproduct. As long as the fuel and oxidant are supplied the fuel cell will continue to operate at a steady power output.

The dense electrolyte is not only an ionic conductor, it also acts as a physical barrier to prevent fuel and oxidant streams from mixing directly, thus diluting the concentration gradient essential to generate a Nernst Potential, and ultimately causing a potential explosion. The electrolyte is an insulator and does not conduct electrons to ensure the cell is not shorted out. Dependant on the design the electrolyte layer may provide mechanical support to the anode and cathode. Fuel cells are primarily classified by the kind of electrolyte material utilized.

Table 1 Fuel Cell Type Overview [(1)] lists the different types of fuel cells commercially available or currently under development. The electrodes must remain physically and chemically stable while performing several different critical functions within the fuel cell. Electrodes are porous throughout to enable the diffusion of hydrogen and oxygen through to the electrolyte, simultaneously permitting the water to diffuse away from the electrolyte, in the case of the anode. At the electrolyte interface, under operating temperatures, the anode also must effectively catalyze the fuel. To transport the ions to and from the electrolyte and to extend the electrochemical region beyond a planar interface, electrode materials must have adequate ionic conductivity. Electrodes also must contain a continuous network of electrically conductive particles to enable current collection of the free electrons. Dependant on the cell design the electrode may provide the mechanical support for the electrolyte and other electrode.

Interconnect

A single unit cell must be modularly stacked in series to achieve the desired voltage. The unit cells are connected together through interconnects with two functions: connect the adjacent cells electrically in series and separate the fuel and oxidant of the adjacent cells to avoid the potential for an explosion. In a stack the repeat unit (single fuel cell/interconnect assembly) is the operational building block. In order to ensure there is a hermetic seal between the fuel and oxidant gas chambers the interconnect plate is bonded around the edges of the electrodes and electrolyte with electrically insulating materials. Low temperature fuel cells can combine the stacks together under compressive force with airtight gaskets to eliminate the need for sealing. Significant research and development efforts are currently underway to address high temperature sealing problems during thermal cycling; however this remains a key challenge to long duration operation of high temperature, planar cell technologies.

Balance of Plant

The remaining balance of plant equipment in the fuel cell system has many vital functions. All fuel cell systems require various levels of fuel conditioning to ensure the fuel composition and purity required for stack operation is continually available. The fuel cell stack will only output a varying dc voltage that must be conditioned with a power conditioner to allow grid intertie and direct AC or DC connectivity. The excess heat produced at the operating temperature of the fuel cells is recycled through the addition of cogeneration balance of plant equipment. A fuel cell system also commonly requires monitoring and electrical control through the use of digital sensory and control board equipment.

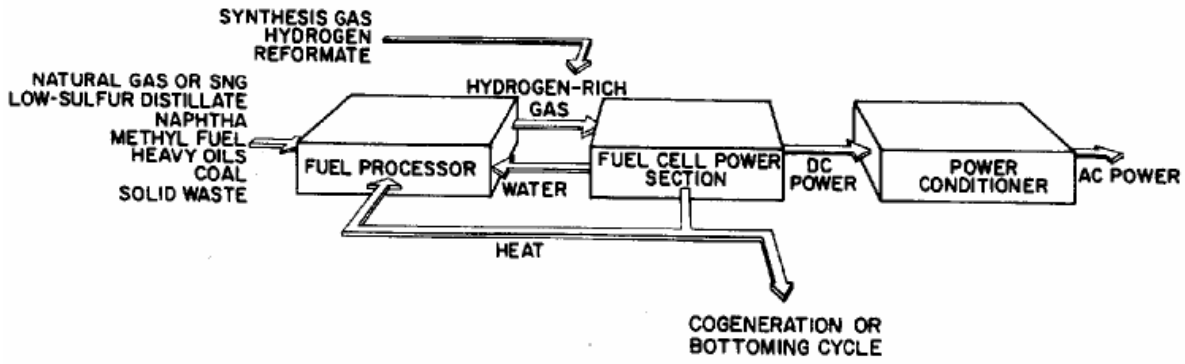


Figure 3 Rudimentary fuel cell system schematic [(1)]

Solid Oxide Fuel Cells

A solid oxide fuel cell (SOFC) consists of a dense ceramic oxide electrolyte. SOFCs are operated at very high temperatures where various ceramic materials are ionic and/or electronic conductors. Operating temperatures are significantly high enough to allow internal fuel reforming and waste heat recovery. However, these high temperatures pose several materials and mechanical design challenges.

SOFCs have a wide range of potential applications, but currently the majority of development is aimed at large stationary power generation and auxiliary power unit (APU) applications. The solid electrolyte layer permits extensive materials and fabrication engineering of the unit cell. Therefore between industry and research there are several successful unit cell and stack designs. The UniCell SOFC seeks to combine the benefits of two different industry accepted designs without compromise.

Electrochemical testing of SOFCs relates the affects of the varying the ceramic processing methods, cell design and operating conditions on performance. Overall efficiency of the fuel cell's ability to convert the available energy stored within the fuel source into electricity

is maximized through limitation of the internal cell losses. The sources for various polarization losses in fuel cells have been identified and characterized over the past century, allowing the fuel cell engineer to reduce the losses by altering the cell architecture, functional materials and test environment.

SOFC Advantages

SOFCs are receiving an increasing amount of attention amongst industrial and academia professionals due to their extensive list of potential advantages. Significant challenges are still being currently addressed to improve lifetime and performance, but commercial installations are becoming more common.

> "Indeed, both simple-cycle and hybrid SOFC systems have demonstrated among the highest efficiencies of any power generation system, combined with minimal air pollutant emissions and low greenhouse gas emissions." (1)

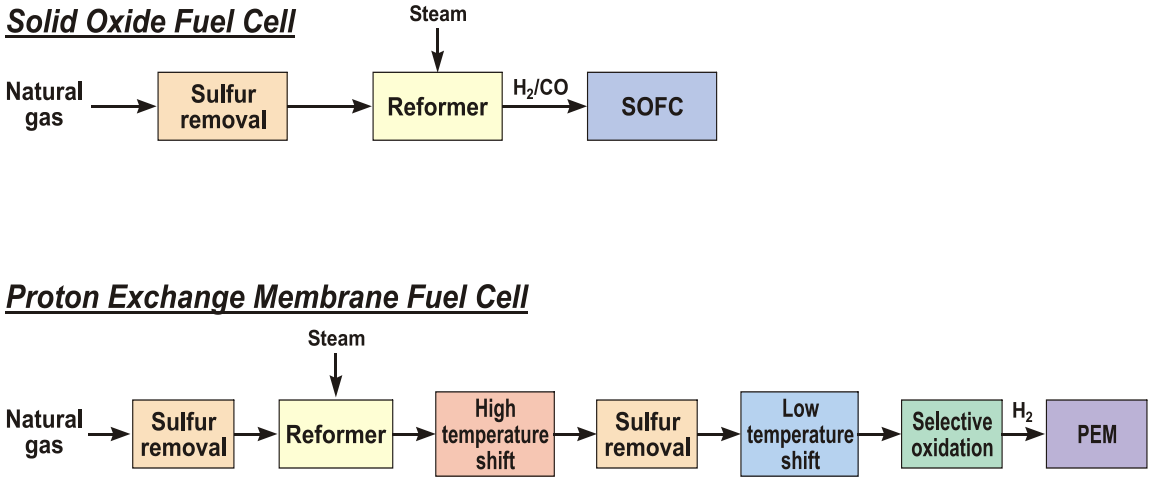


Figure 4 Subsystem comparison of SOFC versus PEM

The high operating temperatures of SOFCs have several advantages. Internal reforming of hydrocarbons inside high temperature fuel cells to produce H_2 and CO_2 allows the flexible use

of several different fuel sources. Low temperature fuel cells utilize high purity hydrogen gas only, requiring a more extensive fuel processing and conditioning of a hydrocarbon fuel source. The high temperatures can also increase the overall fuel cell system efficiencies when the waste heat is recycled for cogeneration or use in a steam bottoming cycle.

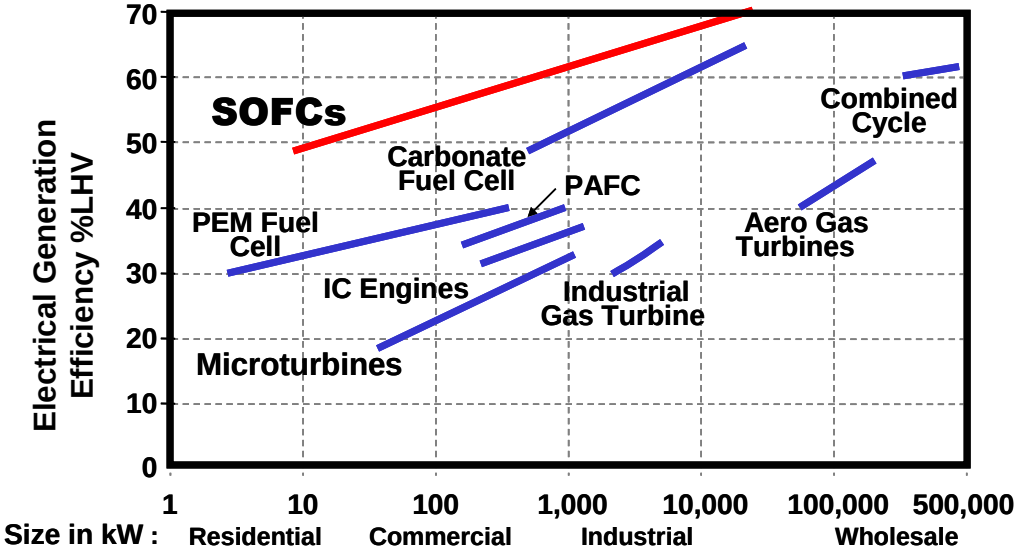


Figure 5 Electrical efficiency comparison [2]

Low operating temperature fuel cells require the use of platinum as the catalyst due to its corrosion resistance and outstanding catalytic properties at the low temperatures. The high catalytic activity is required for the reaction to sustain itself at the desired rate. Platinum is a precious metal, making it a rare and expensive material undesirable for use in a fuel cell. High temperature fuel cells have a much wider range of catalytic materials to choose from which are adequate to promote the reaction and resist corrosion.

Materials science can be applied extensively in SOFC design and fabrication due to the use of solid oxide components. This permits the use of a broad range of innovative engineering techniques to improve cell power densities, efficiency and lifecycle performance.

SOFC Design Challenges

The high operating temperatures of SOFCs also have some negatives effects that have driven many researchers to explore the use of different materials and designs. Several scientists and groups are trying to reduce operating temperatures to as low as 450 - 650 °C to aid in start-up time, insulation requirement and sealing.

Fuel cells typically undergo thermal cycling for systems with on/off cycle applications, such as a car. SOFC thermal cycle start-up and cool-down periods are long and slow to avoid thermal shock to the system throughout the large temperature range. Thermal cycling also increases the internal CTE stresses, causing a decline in lifecycle durations. These interlayer stresses due to the mismatches in the CTE anode, cathode, electrolyte, interconnect and seal materials can even cause catastrophic failure. PEM fuel cells are currently more predominantly considered the choice for applications with regular thermal cycling due to their quick startup times and lower thermal cycle degradation levels.

The high temperatures limit the choice of materials to select from when trying to match CTEs. The use of non-ceramic materials for other reasons, such as stainless steel interconnects and metallic brazes to reduce the material and manufacturing costs, is also desired. However the list of material choices suitable for these applications at high temperatures is limited by oxidation and chromium evaporation effects. Engineered composite materials are therefore being investigated for use in brazes and interconnects, however this has only been implemented in component level studies.

SOFCs are fuel flexible and permit internal reforming, however they are easily poisoned by trace amounts of sulfur pollutants found in most fuels. Alternative materials are being

investigated to improve sulfur tolerance but fundamental mechanisms are still not completely understood.

The brittle nature of ceramic materials results in poor mechanical strength of SOFCs. The increase in material thickness to increase the strength of unit cell layers has a significant negative effect on electrochemical performance.

SOFC Applications

SOFCs are suitable for use in a number of applications that utilize heat. They are best suited for stationary power applications to provide residential and commercial grid augmentation when combined with heating and cooling systems. SOFCs can also be coupled with an energy storage system, which provides peak power transient load demands, and used for remote power supply, assuming a fuel such as propane, biofuel or diesel is easily available.

Auxiliary power applications are well suited to SOFCs due to their high efficiency, fuel flexibility and scalability. A large market potential of APUs in long-haul tractor trailers to supply temperature control and other electrical services is forecasted. SOFCs offer a clean and quiet fuel savings alternative to running a diesel generator for extended periods.

SOFC Electrochemical Performance

A simplified SOFC system run on pure hydrogen and oxygen is depicted in Figure 6. The three phase boundary region within the solid oxide unit cell is where the hydrogen gas meets the electrolyte and anode to react with the oxygen ion. The reaction creates water and causes the release of electrons to the external circuit.

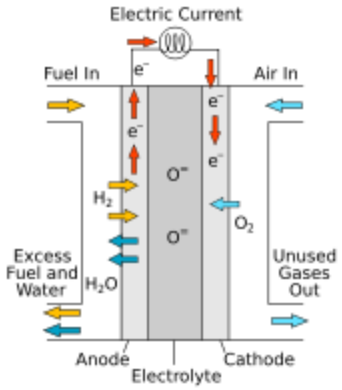


Figure 6 Solid oxide fuel cell schematic [3]

Table 2 SOFC Half Cell Reaction Equations

Anode Reactions	Cathode Reaction
$H_2 + O^{=} \rightarrow H_2O + 2e^-$ Internal Reforming of Methane $CO + H_2O \rightarrow H_2 + CO_2$ Water Gas Shift $CH_4 + H_2O \rightarrow 3H_2 + CO$ Steam Reforming	$\frac{1}{2} O_2 + 2e^- \rightarrow O^{=}$
Unit Cell Reaction (No Methane Present)	
$H_2 + \frac{1}{2}O_2 \rightarrow H_2O$	

The electrochemical performance of an SOFC is dictated by several factors within design, fabrication and operation. The reversible cell model performs ideally without accounting for the true operating losses. Chemical and thermodynamic relations govern the effects of operating conditions on electrochemical performance of the reversible cell model. However, the Gibbs free energy and the Nernst Potential thermodynamic relations do not take into account the irreversible effects due to reaction kinetics. They define the ideal performance of an SOFC determined from reversible thermodynamic properties only.

The actual cell performance deviates from ideal performance during fuel cell operation due to three polarization effects that are observed: concentration, ohmic and activation. It is the

objective of the design engineer to minimize the overall sum of polarization effects throughout the cell. The electrical performance of a non-reversible fuel cell with polarization losses can be described through a mass and energy balance around a fuel cell which accounts for the loss of enthalpy in the fuel, heat generated, heat loss to the surroundings and the electrical energy generated by the fuel cell. The thermal efficiency of a fuel cell is defined as the amount of electrical energy generated versus the change in enthalpy in the fuel feed and product streams. The overall efficiency is the thermal efficiency adjusted for the fuel utilization losses.

Gibbs Free Energy & the Nernst Potential: Gibbs free energy (ΔG) is the maximum amount of electrical work (W_{el}) obtainable due to an enthalpy change in a reversible system from a well defined initial state to a different, well defined final state. In a fuel cell it is the chemical potential of the reactants feed stream minus the product stream. Thermodynamics defines Gibbs free energy as the change in enthalpy minus the irrecoverable energy lost due to entropy change within the system.

$$\Delta G = \Delta H - T\Delta S$$

Equation 1 Gibbs Free Energy [4]

In the simple model where an SOFC is run on pure hydrogen and oxygen, the unit cell reaction equation is:

$$H_2 + \tfrac{1}{2}O_2 \rightarrow H_2O$$

Equation 2 Unit Cell Reaction

To calculate the standard state Gibbs free energy of reaction (ΔG°), the partial molar Gibbs free energy for each species (G°_i) at temperature T are weighted identically as in the reaction equation and summed together. For example:

$$\Delta G^{\circ} = G^{\circ}_{H_2} + \tfrac{1}{2} G^{\circ}_{O_2} - G^{\circ}_{H_20}$$

Equation 3 Unit Cell Gibbs Free Energy Balance

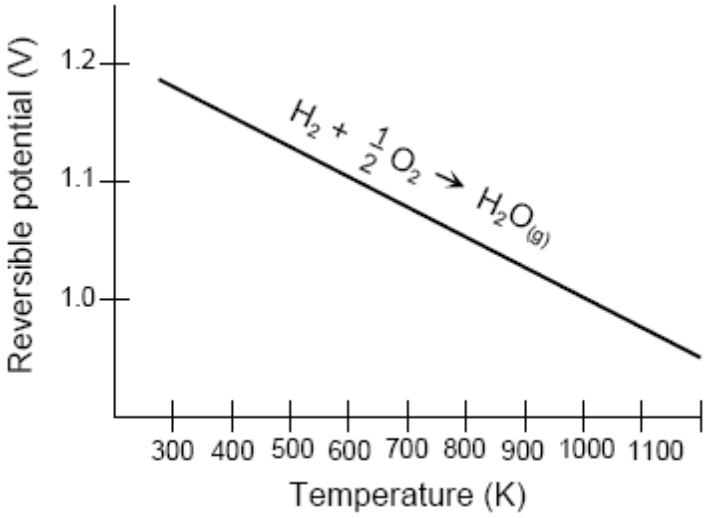


Figure 7 Gibbs Free Energy Change of Reaction

The Gibbs free energy change of reaction is related to the standard state Gibbs free energy of reaction (ΔG°) by the equation:

$$\Delta G = \Delta G^{\circ} + \frac{RT}{nF} \ln(\Pi[reactant\ fugacity]/\Pi[product\ fugacity])$$

Equation 4 Gibbs Free Energy Change of Reaction [1]

Due to the low operating pressures in SOFCs, typically less than 5 psi, the fugacity can be approximated with the partial pressures. The maximum allowable work (W_{el}), or Gibbs free energy (ΔG), is correlated back to the ideal potential of the cell (E) through Faraday's constant (**F**) and the number of electrons (n) in the reaction.

$$W_{el} = \Delta G = -nFE$$

Equation 5 Maximum Electrical Work [1]

The Nernst equation calculates the open circuit potential of the unit cell (E) as a function of the ideal standard open circuit potential (E°), Faraday's Constant (**F**), number of electrons (n), temperature (T) and gas composition partial pressures in the electrodes.

$$E = E^{\circ} - \frac{RT}{n\mathbf{F}} \ln\left(\frac{partial\ pressure\ H_20}{partial\ pressure\ of\ H_20 * partial\ pressure\ of O_2^{0.5}}\right)$$

Equation 6 Nernst Equation [4]

The voltage of an SOFC, E_{SOFC}, is the open circuit potential voltage (E) minus the polarization losses.

$$E_{SOFC} = E - (\eta_{act} + \eta_{ohmic} + \eta_{conc})$$

Equation 7 SOFC Voltage

Polarization Effects: Actual fuel cell performances deviate from the ideal performance due to the three types of irreversible losses: (1) activation polarization (η_{act}), (2) ohmic polarization (η_{ohmic}) and (3) concentration polarization (η_{conc}). The fuel cell voltage-current (V-I) curve can be used to quantify the contribution of each type of polarization to the overall losses. Activation polarization is dominant at low current density and increases with increasing current density. Ohmic losses vary linearly with current and are seen throughout the entire range of current, increasing with increasing current density. Gas transport losses occur throughout the entire current density range but are dominant at high densities.

The rate of electrochemical reaction at the electrode surface is controlled by kinetics. There is an activation energy barrier that must be overcome to promote the reactions. If the kinetics are too slow, the desired rate of electrochemical reactions to overcome the activation energy barrier can't be sustained. Activation polarization is the extra potential required to

overcome the barrier. At high temperature, SOFC materials' catalytic properties are enhanced. SOFCs therefore typically have low levels of activation polarization.

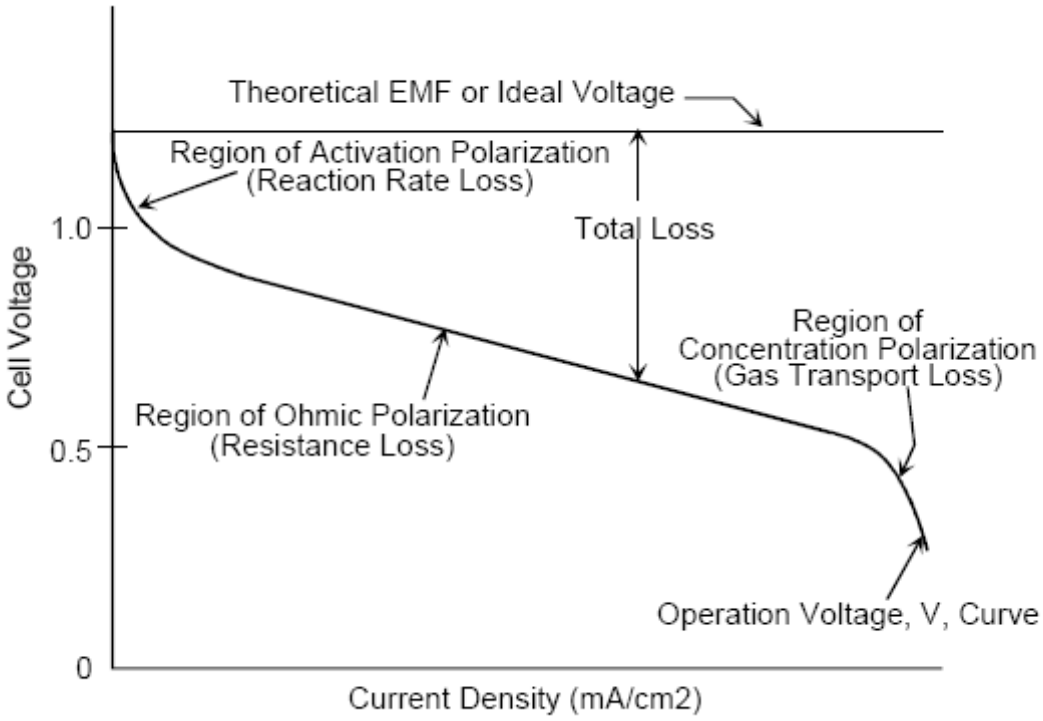


Figure 8 Fuel Cell V-I Curve [1]

Concentration polarization is dominant at high current densities where mass transport limitations prevent enough reactant from being delivered to the three phase boundary to sustain the high reaction rates. There are three dominant sources of concentration polarization within the solid oxide unit cell due to mass transport of the products and gas-phase reactants: (1) gas diffusion from the gas channels into the electrodes (2) reactant diffusion through the electrodes to the three phase boundary and (3) diffusion of the product (H_2O) away from the electrolyte interface. The tortuous gas diffusion paths through the electrodes must be minimized to limit concentration polarization. Engineered pore structures in the electrodes can help facilitate gas

transport to the electrolyte interface and are being investigated throughout the fuel cell community.

SOFC ohmic polarization in the unit cell is due to the resistance to flow of ionic and electronic charge carriers, in the electrolyte and electrodes respectively. The ohmic polarization is directly related to the SOFC cell design, material choices, manufacturing process and operating conditions. Ohm's law equates the ohmic losses (η_{ohm}) in the unit cell components to the current (i) flowing through the cell multiplied by the total internal cell resistance (R).

$$\eta_{\text{ohm}} = iR$$

Equation 8 Ohm's Law

The total internal cell resistance is a combination of the electronic, ionic and contact cell resistances.

$$R = R_{electronic} + R_{ionic} + R_{contact}$$

Equation 9 Internal Cell Resistance

In the planar ESC ionic resistance dominates the total resistance due to the thick electrolyte layers. Area Specific Resistance (ASR) can be used to correlate the ionic resistance to electrolyte's conductivity ($\sigma_{electrolyte}$) and layer thickness ($\delta_{electrolyte}$).[4]

$$ASR = \delta_{electrolyte} / \sigma_{electrolyte}$$

Equation 10 Area Specific Resistance

The ionic conductivity of the solid oxide electrolyte is strongly affected by operating temperature and thickness (ionic path distance through the material) when fabricated out of 8 mol% yttria stabilized zirconia (YSZ).

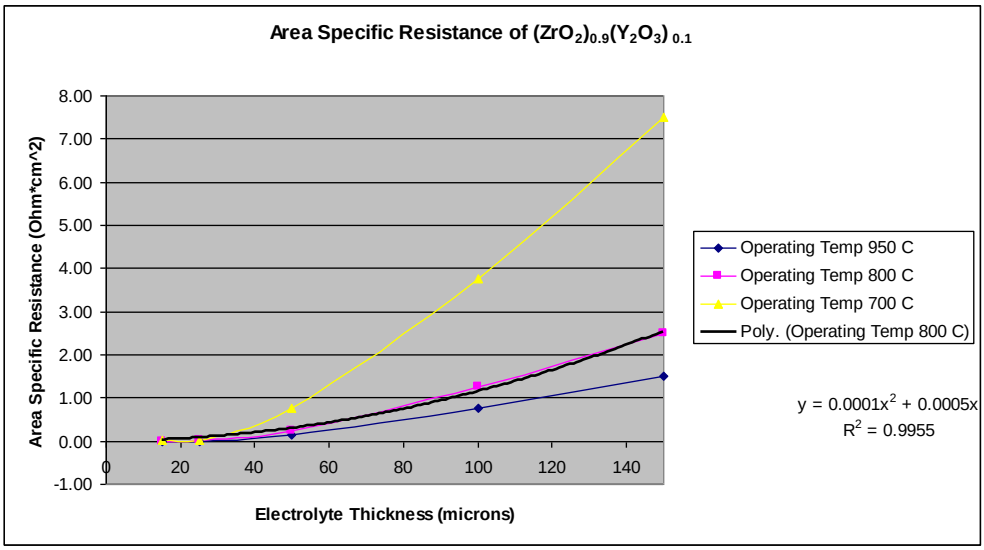


Figure 9 ASR of YSZ Electrolytes as a Function of Temperature

SOFC Efficiency: Since fuel cells electrochemically convert fuel directly into electricity they are not limited by the Carnot efficiency. The thermodynamic efficiency is the maximum efficiency a fuel cell can obtain by converting all of Gibbs free energy into electricity.

$$\eta_{ideal} = \Delta G / \Delta H$$

Equation 11 Ideal Fuel Cell Efficiency

Consider a fuel cell operated on pure hydrogen and oxygen at 25 °C where the product water is in liquid form. Gibbs free energy (ΔG) is calculated utilizing the "Unit Cell Gibbs Free Energy Balance" equation (page 17) to be 237.1 kJ/mole. The thermal enthalpy change of this reaction (ΔH) is 285.8 kJ/mole. Therefore this fuel cell's ideal efficiency under these conditions is 0.83 [(1)]. A fuel cell model is considered reversible if it can achieve its ideal efficiency.

In SOFCs where the operating temperature is well above ambient, the efficiency is further decreased due to the temperature effect on Gibbs free energy. As operating temperatures increase, the available Gibbs free energy is decreased and more energy is lost to heat.

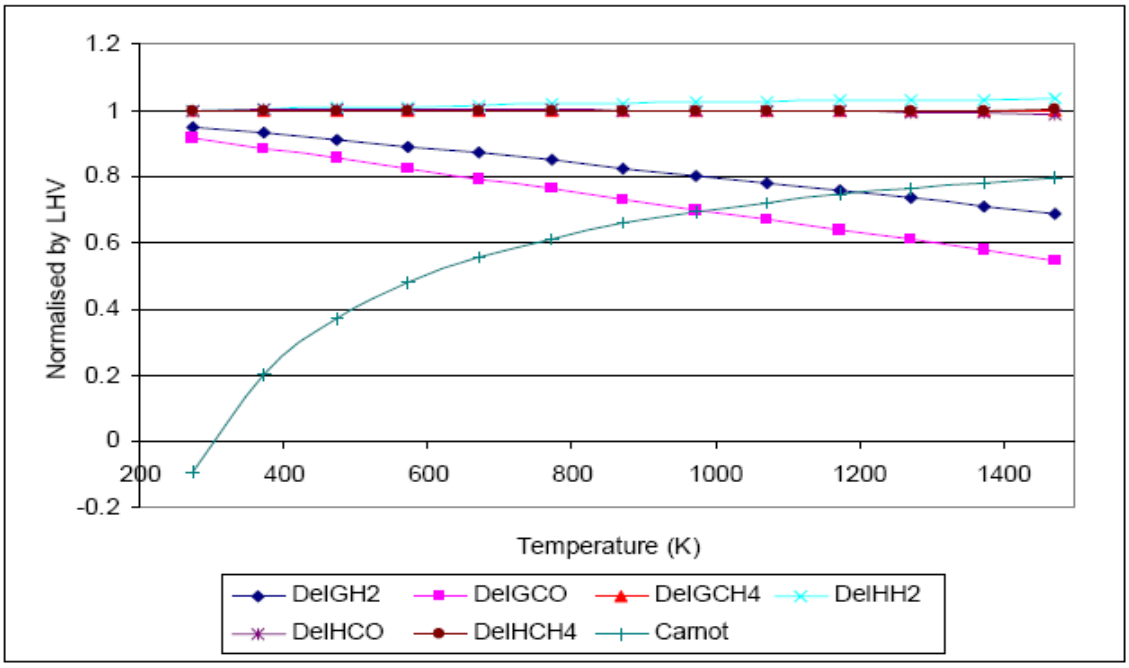


Figure 10 Thermodynamic Efficiency of Reactants at Elevated Temperatures [5]

The voltage efficiency is the actual open cell voltage (E_{SOFC}) divided by the theoretical open cell voltage (E).

$$\eta_{volt} = E_{SOFC} / E$$

Equation 12 Voltage Efficiency

SOFCs do not electrochemically react all of the fuel delivered to the cell. When high levels of fuel utilization are attempted the concentration of the fuel at the three phase boundary is diluted, increasing the concentration polarization effect. Fuel utlilization is computed as the fraction of the fuel that enters the cell and reacts electrochemically.

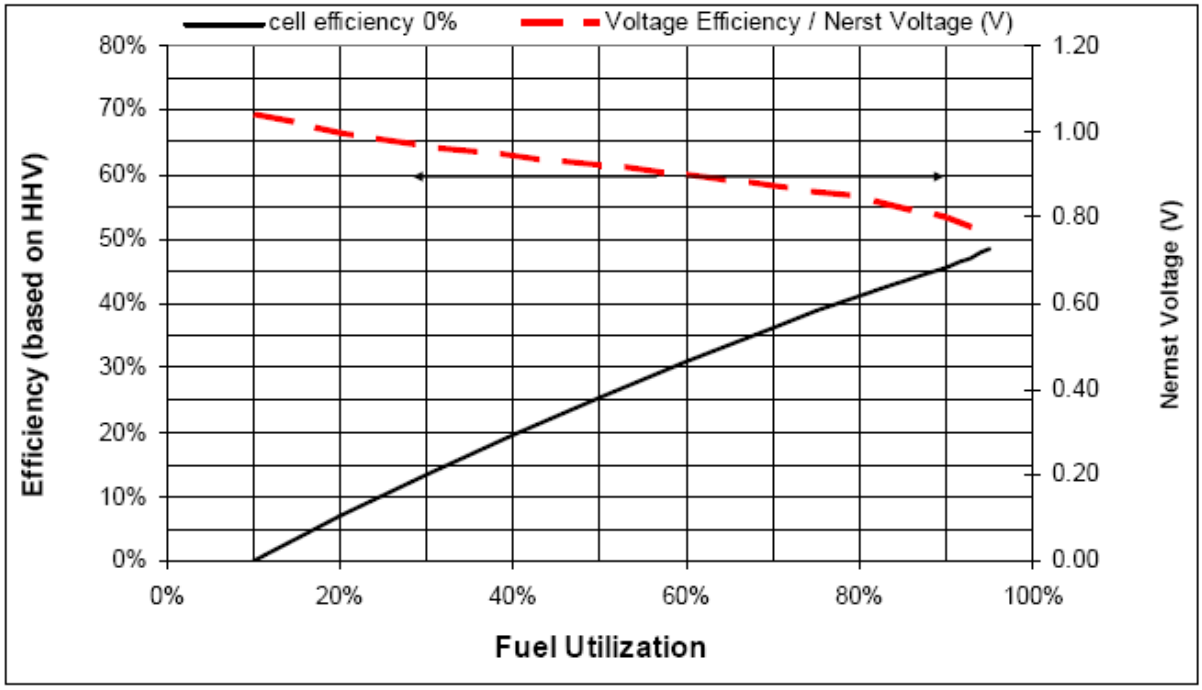


Figure 11 Fuel Utilization vs. Cell Efficiency [1]

The overall cell efficiency can be calculated by multiplying the voltage efficiency by fuel utilization.

$$\eta_{cell} = \eta_{volt} * \text{Fuel Utilization}$$

Equation 13 Cell Efficiency

This does not take into consideration BOP and gas flow losses encountered in complete fuel cell systems.

SOFC Operation Variables: The varying of fuel cell performance testing variables (operating temperature, pressure, fuel utilization, feed compositions and current density) alter the ideal cell voltage and polarization contributions. Current density affects the contribution levels of all three polarization losses. The optimum current density can be determined by plotting the cell output power density as a function of current.

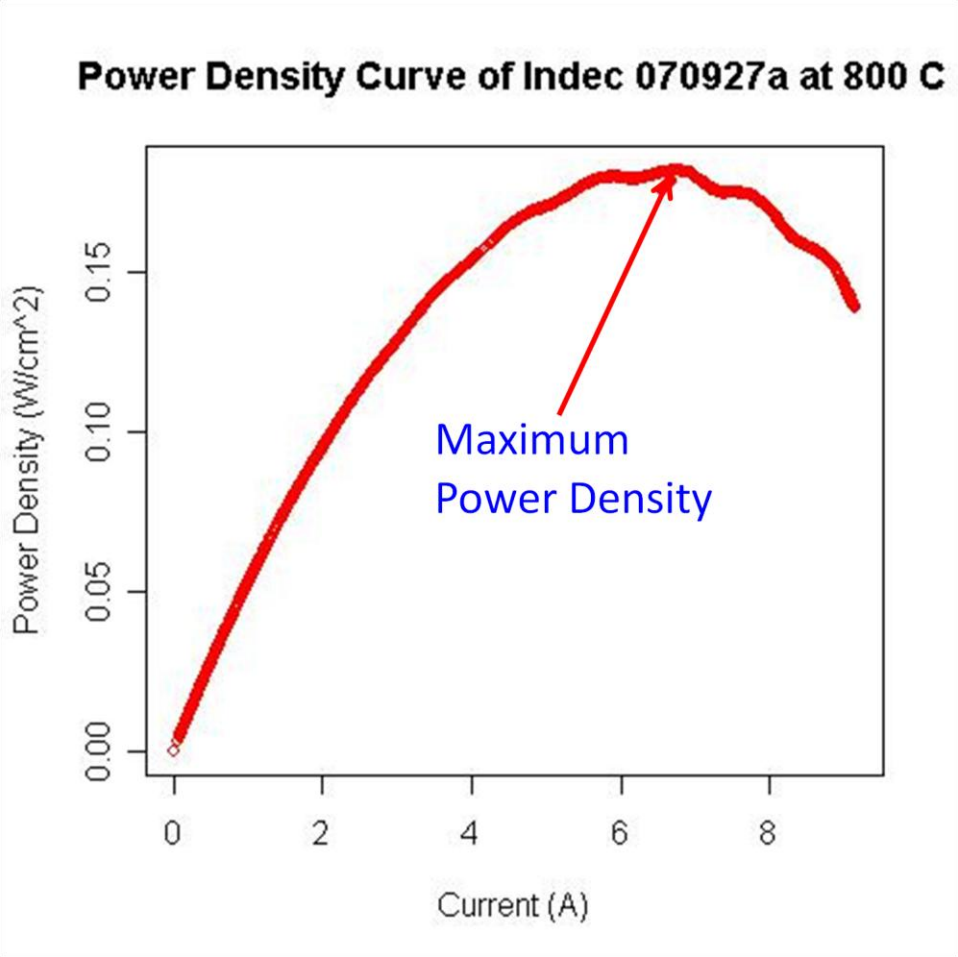


Figure 12 Power Curve Demonstrating Peak Power vs. Current Density

Increasing the operating temperature improves the ionic conductivity of the electrolyte, in turn minimizing the ohmic polarization. Higher operating temperatures also increase the catalytic activity in the electrodes, decreasing the activation polarization effects to a negligible level in SOFCs. However the increase in temperature decreases the potential open circuit voltage (OCV). This is directly due to the decrease in the Gibbs free energy with increased temperatures as discussed earlier.

The Nernst Potential is a function of the reactants' partial pressures. Increases in the partial pressures increases the OCV, improves mass transport (reducing concentration

polarization) and gas solubility. System seals and fuel handling equipment must be capable of withstanding higher pressures, increasing the initial fabrication costs and constraining the seal material selection.

Fuel utilization is a direct multiplier to the fuel cell's overall net efficiency and can therefore have drastic effects on the operating costs (refer to page 21 for more details). The gas compositions in high temperature fuel cells can affect fuel utilization rates due to internal reforming producing additional fuel via the water gas shift.

SOFC Unit Cell Components

The SOFC unit cell consists of an electrolyte, anode and cathode fabricated from solid oxide materials. The use of solid oxide components enables materials science to be applied extensively in SOFC design and fabrication. Ceramic layers reduce the undesirable power degradation effects seen in liquid fuel cells over time due to the migration of the electrolyte into the electrodes. However elemental migration is possible in SOFC due to the high energy levels encountered at operating temperatures. There are industry standard materials commonly used for the electrolyte and electrodes. However developers and researchers are investigating new materials to improve performance, lifetime, poisoning tolerance, etc. The ceramic material processing methods and unit cell design offers a host of avenues to optimize the SOFC's performance. In order to remain within the scope of this document a detailed description of only the industry standard materials utilized in the UniCell will be covered.

Anode: The anode material commonly used in SOFCs is Ni-YSZ. The nickel must form a continuous network throughout the anode layer because it serves two purposes: electrical

conductivity path and catalyst of the hydrogen. The reduction of the NiO powder to Ni results in a feasible porosity of the anode. However, several processing techniques and compositions are currently utilized or being developed to improve the efficiency of water and gas transport through the pore structure of the anode. The YSZ is an ionic conductor used to transport the ions away from the electrolyte, thus extending the triple phase boundaries. The Ni-YSZ is more physically stabile, and less prone to corrosion than pure Ni.

Despite the wide acceptance of Ni-YSZ anodes several disadvantages remain. The nickel network is corroded and decomposed in the presence of sulfur. The nickel is easily re-oxidized, especially at elevated temperatures, when in the presence of air. This oxidation and reduction cycles results in a large volumetric change and severe stress levels. In anode supported designs this could result in catastrophic failure, therefore SOFCs typically require a reducing atmosphere on the anode side at all times. The mismatch of CTE with the interconnect layer and electrolyte layer also creates high levels of internal stresses.

Cathode: Lanthanum manganese oxide doped with strontium (LSM) is widely used for SOFC cathodes due to several reasons. LSM is chemically and physically stable at operating temperatures, with a CTE near that of YSZ. Electronic and ionic conductivity levels are fair at 800°C. To limit the ionic and electrical resistance of the LSM cathode the overall thickness is minimized, and commonly an interlayer of LSM and YSZ is placed between the YSZ electrolyte and the LSM cathode. The LSM has proven to be sufficiently stable when in contact with the standard interconnect materials. For low temperature SOFCs alternative materials are being investigated.

Electrolyte: Solid oxide fuel cells (SOFCs) are constructed with a solid, non-porous ceramic electrolyte, usually yttria (Y_2O_3) stabilized zirconia (ZrO_2). The yttria is added to stabilize the zirconia oxide during cooling because this process causes the zirconia to undergo a phase transformation in the crystal structure. This phase transformation has a volume change associated with it that causes the structure to shatter during a heating process.

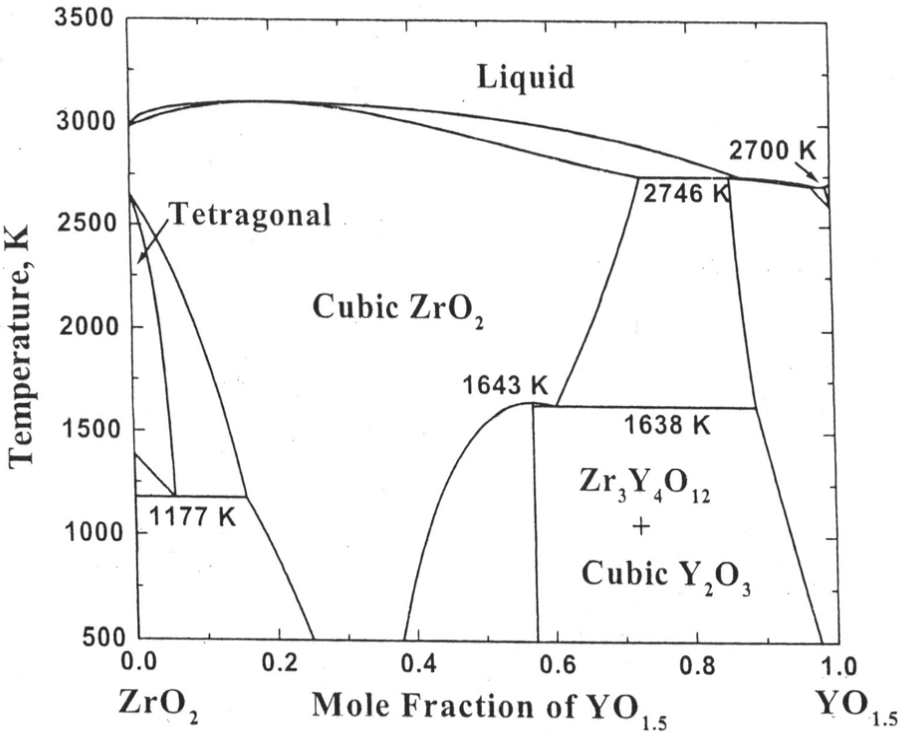


Figure 13 Phase Diagram of YSZ [6]

At 3 mol% yttria, a partially stabilized mixture of zirconia polymorphs exists because an insufficient amount of the cubic phase forming oxide has been added. At 8 mol % it is fully stabilized and its structure becomes a cubic solid solution. However 3 mol % YSZ structure is 4 times stronger than 8 mol % YSZ structure. Reasoning for this is discussed later in "Ceramic Mechanical Properties" on page 64.

The electrolyte material of an SOFC is a negative ionic conductor of the oxygen ions from the cathode to anode. Cells must operate at high temperatures between 600 to 1000°C where the conduction of oxygen ions through the electrolyte is feasible. The addition of yttria to zirconia results in vacancies within the lattice that transport oxygen ions. The yttria, Y^{+3}, substitutes for the zirconia, Zr^{+4}, in the lattice structure. There are more oxygen ions per zirconia ions, than oxygen ions per yttria ions, and therefore the higher the concentration of yttria oxide added the more oxygen vacancies that are produced, improving the materials ionic conductivity. Take for example a 100 mol sample of 8 mol% YSZ. In the 8 mol% Y_2O_3 there are 16 moles of Y^{+3} and 24 moles of $O^{=}$. In the 92 mol% ZrO2 there are 92 moles of Zr^{+4} and 184 moles of $O^{=}$. Therefore there are a total of 108 cations and 208 oxygen sites full. However the lattice of pure zirconia oxide would have 2 oxygen sites per cation, or 216 total sites. Therefore there are 8 oxygen sites vacant per 100 moles of 8 mol% YSZ for the ionic conduction of oxygen.

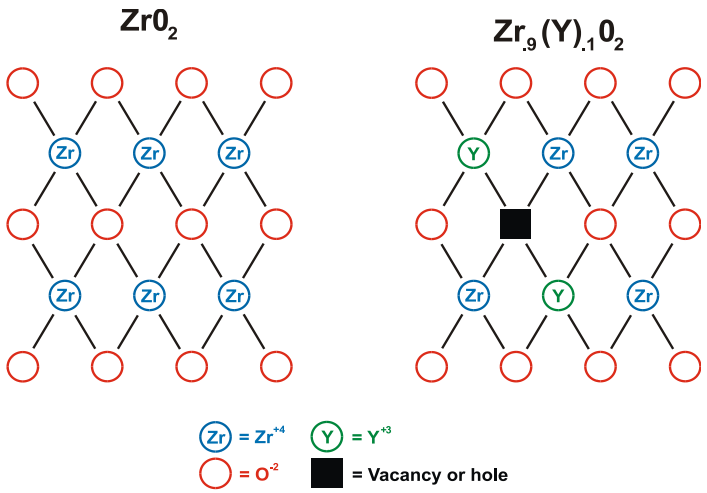


Figure 14 Pure Zirconia and Partially Stabilized Zirconia Lattice Diagrams

The increase in mol % of yttria in YSZ increases ionic conductivity but decreases mechanical strength. In utilizing 8 mol% YSZ, the fuel cell designer compromises the

electrolyte layer's overall mechanical strength to obtain adequate levels of ionic conductivity within the desired operating temperature range.

SOFC Unit Cell Architectures

There are two predominate architecture designs of the solid oxide unit cell, planar (Figure 15) and tubular (Figure 16). A planar fuel cell is assembled with the anode, electrolyte and cathode combined to form a flat plate cell. As the naming convention implies, the electrolyte layer provides the mechanical support for the electrodes in planar electrolyte supported cells (ESC), whereas the anode provides the mechanical support for the unit cell in planar anode supported cells (ASC). The fuel and oxidant are delivered to the electrodes through gas channels in the interconnect plates. The tubular fuel cell design consists of concentric tubes assembled in a bundle. If the cathode is on the inside the oxidant is flowed down the middle of hollow tube and the fuel is flowed around the outside.

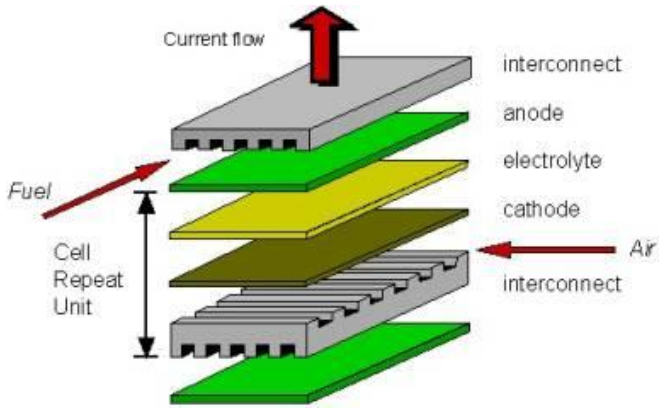


Figure 15 Planar fuel cell design

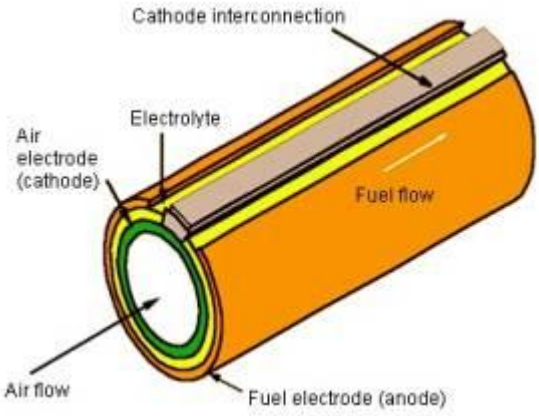


Figure 16 Tubular fuel cell design [7]

Planar metallic bi-polar supported SOFCs utilize a metallic layer to provide the mechanical support for the electrodes and electrolyte. Although significant benefits arise from this design chromium poisoning is currently a design limiting challenge. Micro tubular SOFCs

are gaining attention throughout industry due to the combination of standard tubular benefits with high volumetric power densities.

Concentration polarization is the dominate source for efficiency loss in the ASC design due to the thick anode. Gas transport losses are negligible in ESC cells due to the thin anodes. Instead, the ESC irreversible losses are dominated by the high ionic polarization from the thick electrolyte. Tubular SOFCs losses are dominated by ohmic polarization due to extensive electrode current path lengths. The UniCell design is an ESC with decreased ionic polarization.

Planar Anode Supported Cell (ASC): The planar ASC is currently widely utilized by SOFC manufacturers. The anode layer, typically Ni-YSZ, is 0.5 to 1.0 mm thick to provide the mechanical support for the thin electrolyte (3 to 15 μm thick) and cathode (~50 μm thick). The thin electrolyte limits the ionic polarization and allows the cell to be operated at lower temperatures (600 – 800 °C). Power densities as high as 1.8 W/cm^2, at 800°C, have been reported (8).

The thick anode layer presents a host of problems. The concentration polarization dominates due to the tortuous gas diffusion paths. This results in poor fuel utilization which can mitigate the key benefit of the ASC. Compression loading of the unit cell is impossible due to the low mechanical strength of the anode, leading to poor interconnect contact. Sealing to the porous anode is very difficult and can result in gas leakage or electrical short circuiting. The asymmetrical design, anode/electrolyte CTE mismatch, and thick support anode yield undesirable cell camber. Nano thin electrolytes have demonstrated instabilities under operating conditions.

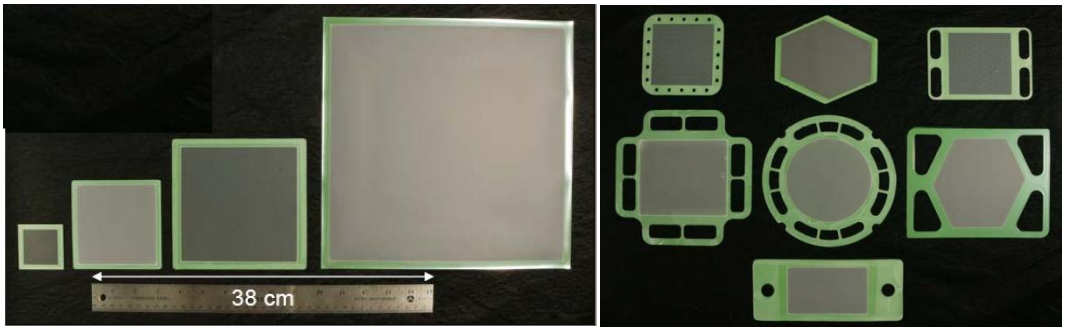


Figure 17 Anode supported SOFCs [9]

Planar Electrolyte Supported Cell (ESC): The electrolyte supported cell (ESC) presents a host of advantages. The planar ESC is based on the 100 to 150 µm thick YSZ electrolyte which provides increased mechanical support for the 10-50 µm thick anode and cathodes. The decrease in anode thickness by an order of 10 from the ASC limits the gas diffusion polarization. Tape casting of the electrolyte permits large diameter scale-up potential with minimal cell curvature. The dense YSZ electrolyte provides an optimal seal contact surface.

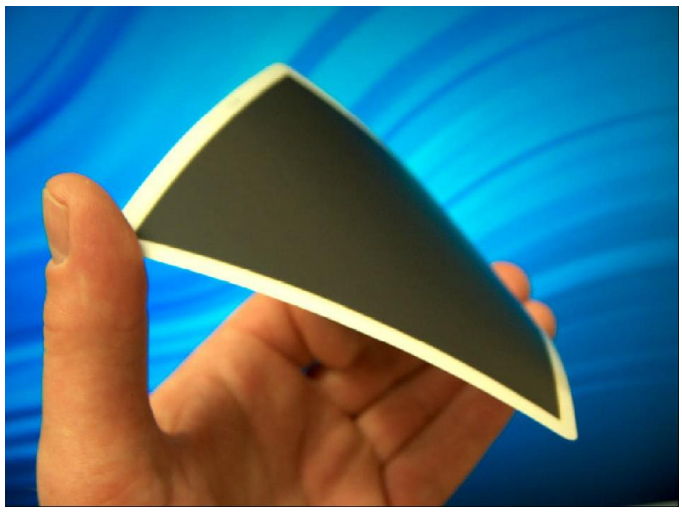


Figure 18 Hionic™ electrolyte supported SOFC [10]

The key design obstacle in the ESC arises from high cell ASR due to the thick structural electrolyte. Ionic conductivity of the electrolyte is a function of temperature and thickness. To

limit ohmic polarization in the ESC the operating temperatures must be raised to 1000 °C where significant materials challenges limit the design, or the ionic path length must be decreased to 50 µm as shown above (SOFC Polarization, page 18).

Tubular SOFC: The Tubular SOFC design consists of three concentric cylindrical tubes: (1) anode (2) electrolyte (3) cathode. The tubular architecture eliminates the needs for sealing of the unit cells and easily permits internal reforming. The circular tubes radially disperse the interlayer thermal stresses due to mismatches in CTE, resulting in a thermally robust cell design. However, the tubular design requires the electrodes to carry the electrons along the length of the tube to the interconnect. Therefore ohmic polarization due to electrical resistance dominates the tubular cell polarization effects. Tubular SOFCs are also manufactured utilizing extrusion & plasma spray technology, increasingly the overall production costs.

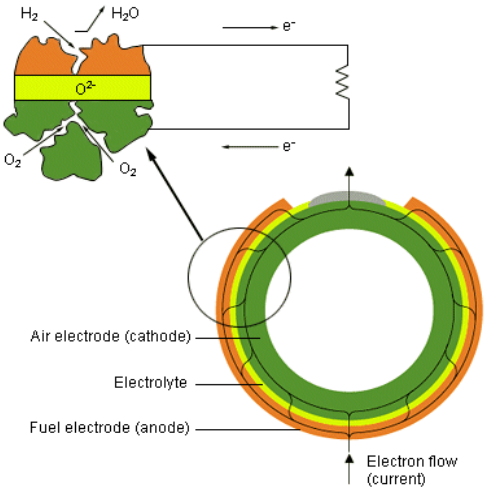


Figure 19 Tubular SOFC Design [7]

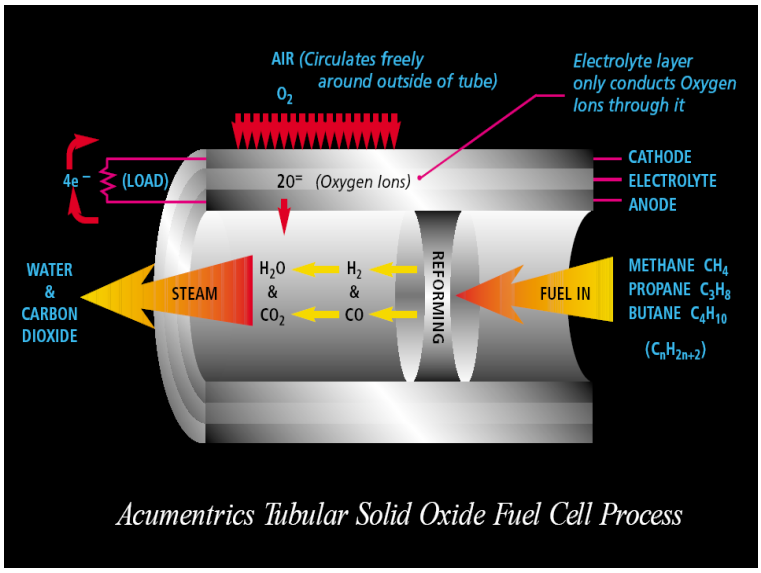


Figure 20 Tubular SOFC Process [11]

The tubular SOFC has been commercialized by Siemens, amongst others, demonstrating long life cycles with limited power degradation. A stationary Siemens SOFC system demonstrated operating time of > 69,000 hours (~8years). Thermal cycle robustness of tubular SOFCs design was also demonstrated with more than 100 thermal cycles from ambient to 1000 °C. Minimum degradation effects, < 0.1% per 1,000 hours, demonstrate lifecycle voltage stability in the tubular SOFC design. [12]



Figure 21 Tubular Fuel Cell Design [7]

Planar Metallic Bi-Polar Plate Supported: SOFC engineers developed the planar metallic bi-polar plate supported unit cell design to limit the ionic, ohmic and diffusion polarization. The mechanical support is provided to the anode, electrolyte and cathode by a metallic mesh interconnect. Therefore the design permits the use of a thin anode and electrolyte, limiting diffusion and ionic polarization respectively. The planar design limits electronic path lengths and ohmic polarization which dominate tubular designs. The inexpensive metals replace the ceramic materials, lowering the overall materials cost. Co-sintering of all the layers has been demonstrated, decreasing production costs.

The manufacturers of metallic plate supported cells are plagued by the detrimental release of chromium. Chromium poisoning of the unit cell corrodes the nickel network, shutting off catalytic properties. The metal mesh also decreases the volumetric power density.

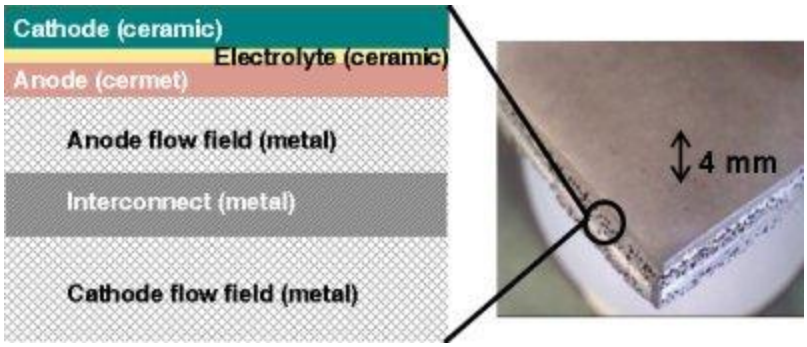


Figure 22 Argonne National Lab's TuffCell [13]

Micro Tubular SOFC: The micro tubular SOFC utilizes cold drawn tubes with a diameter less than 1mm, resulting in much higher volumetric power densities for bundles than tubular SOFCs. Yet the design preserves the tubular benefits: thermal cycling robustness, seal less design, rapid fuel cell startup. Electron path lengths are improved, decreasing the overall effect of ohmic electric polarization. The processing techniques have been successfully demonstrated but currently remain expensive.



Figure 23 Portable Micro-Tubular SOFC [14]

Engineering of Advanced Ceramics

The UniCell electrolyte supported cell design utilizes a thick YSZ electrolyte layer to provide support to the electrodes. The UniCell electrolyte differs from a standard ESC with the inclusion of interleaved channels. The UniCell design is described in detail in on page 71.

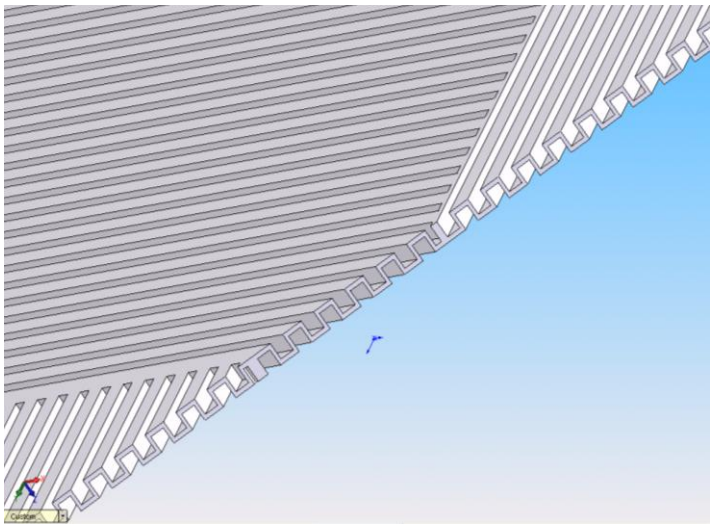


Figure 24 UniCell Electrolyte with Interleaved Channels

The UniCell electrolyte layer was fabricated utilizing standard ceramic processing techniques combined with laser drilling. The SOFC fabrication process began with a previously prepared ceramic powder dissolved into a solvent based solution consisting of a series of binders, plasticizers and dispersants. Ball milling of the media ensured proper suspension of the ceramic powder in the slurry solution. The slurry was then formed into a flexible thin film via tape casting. Upon drying the green ceramic tape was altered through laser drilling to include the interleaved channels (see page 56 for more details). The UniCell electrolyte was sintered at high temperature to remove all the additives, leaving behind only the dense ceramic structure. Electrode inks were prepared and applied to the electrolyte layer as thin films less than 15

microns thick. A chemical bond was formed between the pre-sintered electrolyte, and the green anode and cathode layers, during the final co-sintering step.

Ceramic Powders

The ceramic powders are the most important ingredient in the batch recipe used to produce the SOFC components. The final sintered SOFC parts consist of only the ceramic constituent. The remaining ingredients from the slurry facilitated the fabrication of the layers with the desired form but were then burned out. The ceramic powder utilized for the UniCell electrolyte is 8 mol% YSZ due to the functional properties as discussed in "SOFC Unit Cell Components" on page 25.

The processing method utilized in the transformation of raw materials into the inorganic ceramic powders determines the particle size, homogeneity of particle size distribution, surface area and impurity levels. There are several ways to synthesize ceramic powders including but not limited to solid-solid, solid-gas and solution processes. YSZ and LSM powders from different manufactures, who utilize varying processing procedures to produce powders with different average particle size and surface area, were studied to determine the effect on microstructure and processing parameters.

The reduction in surface energy of the high energy small particles through conglomeration into larger particles with less surface area per volume is the driving force in the sintering process. Therefore use of small particles decreases the required sintering temperature and/or cycle duration to obtain the desired grain growth. The sintering process is discussed in detail later.

The particle size and homogeneity of particle size also affect the green density of the tape due to the packing configuration. Small particles allow a denser packing configuration, however the poor flow characteristics of the small particles counteract the benefit. In a conglomeration of different particle sizes the small particles can fit in the interstitial vacancies between the larger particles and cause undesired secondary grain growth during sintering.

"From the processing standpoint, the materials scientist should be interested in the surface area of a powder because surface area is the most significant factor in its interaction with organic additives such as surfactants and binders." [15] The interactions with the surfactants and binders are discussed later in "Electrolyte Slurry" on page 39. The density of the ceramic powder effects the dispersion and suspension stability of the solution.

In order to develop a proof of concept UniCell prototype it was unnecessary to fully optimize the powder size morphology. Also due to the increased costs of finer particle size powders the effect of powder morphology on sintering cycles was the only test conducted. However the ceramic powder morphology does affect the final product drastically and should not be neglected in continued development.

Uniaxial Dry Pressing: YSZ and LSM dry powders were pressed into dense pellets with a uniaxial press to investigate the effect of powder morphology on the sintering process. Uniaxial dry pressing is a forming process used to manufacture simple, dense parts that can be handled and sintered easily. The simple process consists of three steps: (1) fill the die with the ceramic powder (2) compaction of the powder and (3) ejection of the part.

The ceramic powder can be mixed with plasticizers, binders and die lubricants to improve the properties and facilitate the production of the parts. This mixture comprised mostly of the

ceramic powder occupies 25-35% [16] of the die volume prior to pressing. The compaction of the powder first evacuates the air, followed by a three stage densification of the powder illustrated in Figure 25.

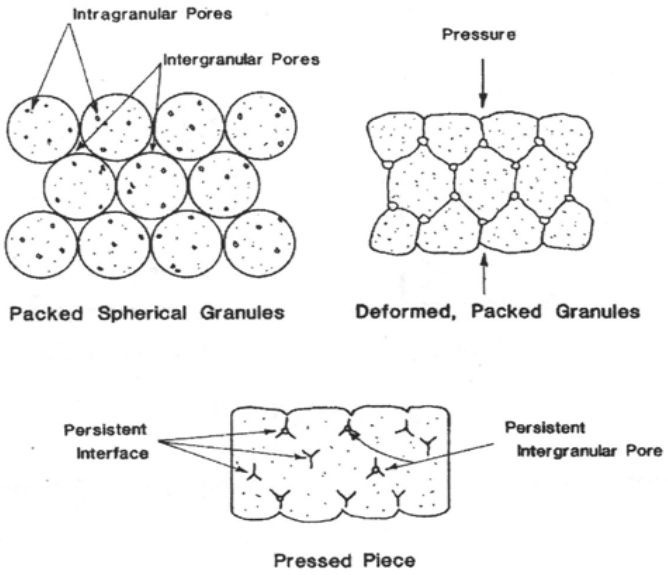


Figure 25 Uniaxial Dry Press 3 Stage Compaction Process [16]

The first stage is the flowing of the particle granules into an arranged structure. If the ceramic powder particle granule size is too small it will limit the ability to flow into a higher packing order. Once the maximum packing order has been reached primary densification occurs and the spherical shaped granules deform under pressure to fill the void interstices. The final stage involves the rearrangement of the individual powder particles into a higher packing order.

Elastic energy is absorbed in the compacted powder and released as the pressure is released, separating the pressed pellet from the die walls. A die lubricant is utilized to facilitate the release of the formed part and reduce the frictional forces. Defects commonly encountered in uniaxial pressing include density gradients from high frictional forces, laminations from unsteady pressure application and fracture due to rapid release of stored elastic energy.

Electrolyte Slurry

Prior to tape casting the electrolyte slurry must be prepared. The electrolyte slurry is a viscous solution that flows onto a moving mylar surface and is then pulled under a doctor blade into a thin film. The composition of the slurry consists of the base powder dissolved in a solvent with a dispersant, binders and plasticizers. Tape cast slurries have a higher concentration of binders and plasticizers than in dry pressing. Two-stage milling of the slurry disperses the powder in the solvent first, and then introduces the binder system. Electrolyte slurry composition and preparation drastically drives the properties of the tape cast.

Solvent: The YSZ ceramic powders are suspended in an organic liquid, the solvent, to allow the forming of an electrolyte thin film via tape casting. The powder is homogeneously dispersed throughout the solvent to create a uniform liquid mixture. The solvent must dissolve the remaining slurry constituents (dispersant, binders and plasticizers). Once the tape has been formed into the desired thin film shape the solvent must evaporate quickly enough to sustain the desired drying rate. The evaporation of the solvent leaves void spaces behind. Some of the void spaces are eliminated during the shrinkage of the tape, and the rest is left as void space. The solid's loading level of ceramic powder to solvent affects the green tape density after drying. A high green density is desired to minimize shrinkage during sintering.

Water and nonaqueous liquids are common solvents for ceramic tape casting. In fabrication of SOFC components, where the powder dispersion and drying rate are of particular concern, nonaqueous solvents are commonly used. The solvent is a polar liquid which gets physically and chemically absorbed onto the surface of the ceramic particles while dispersing the particles homogeneously. Nonaqueous solutions are less polar than water and used with the less

polar YSZ ceramic powders. The binders available to produce a suitable electrolyte thin film from an aqueous based solution via standard tape casting all have significant drawbacks.

A multiple component solvent aids in the absorption of the other slurry ingredients, and can be used to prevent the formation of a skin layer on the reservoir surface. This skin layer is a result of the slurry drying prematurely on the outside and creating a barrier for the evaporation of the solvent from the body, slowing down overall drying. The addition of ethanol slows the evaporation process to ensure the skin doesn't form and the bulk film dries quicker and more evenly throughout the entire thickness. A homogenizer agent can aid in keeping the drying surface liquid to retard skin formation. Xylene is a highly volatile solvent added to improve the drying time, evaporating quickly. The balance of the high and low volatile solvents is therefore critical.

Dispersant or Deflocculant: A dispersant agent, or deflocculant, reduces the surface tension between individual particles to eliminate the formation of particle clusters, or flocs. The even dispersion of the particles in a homogeneous solution is critical in producing a consistent thin film. Large particle clusters will trap air within the structure, and when released will create flaws in the structure. The even dispersion of small particles also results in a denser green tape, reducing shrinkage and cell curvature during sintering.

The van der Waals (VDW) forces are the weak electrostatic binding forces that hold several particles together. A dispersant creates a repulsive force between the individual particles in one of two fashions: (1) coats the surface to prohibit particles from coming into physical contact or (2) ionic charging of the particles through desorption of ions at the surface. The ionic repulsion forces must exist at a higher level than the VDW forces to stimulate dispersion.

Two different dispersants were investigated for the manufacturing of the UniCell electrolyte: (1) Menhaden blown fish oil (MFO) and (2) Polyester/Polyamide Copolymer Hypermer KD-1. The MFO has a high deflocculating ability due to its high concentration of fatty acid esters. The long chain fatty acids attach to the ceramic particles and extend into the solvent. The blowing of the oil develops an active polar ester group, raises the fatty acid concentration and aids in the complete wetting of the particles. (15) The KD-1 is an anionic surfactant in polar liquids. It has an ability to withstand higher levels of solids loading and lowers the solution viscosity. [17]

Binder: Tape cast slurries utilize a high molecular weight binder to absorb onto the surface of the ceramic particles and bridge them together. The long-chain polymer binder forms a continuous complex matrix that surrounds all the ceramic particles completely, leaving only the binder matrix exposed. Different binder matrices are capable of varying impregnated solids loading levels. The binder choice and concentration has significant effects on the green tape's strength, flexibility, plasticity, toughness and surface finish. However during sintering the binder matrix is completely burned out. The processing atmosphere must react with the binder to ensure it is released from the structure. The binder composition will drive the mechanism and volatility of binder burnout. This can cause concern because when the release of the binders is too rapid because it causes the formation of internal voids.

The vinyl binder utilized to fabricate the UniCell electrolyte tape cast was polyvinyl butyral. The vinyl binder can be fired in a standard oxidizing air atmosphere. It burns out a relatively high temperature (140 – 200 °C)[18] leaving behind carbon which requires oxygen to react with and be transported away as CO and CO_2. Other binders common throughout tape

casting include but are not limited to acrylic, cellulose and aqueous polymers. The choice of vinyl binder for the UniCell tape is driven by a binder that can be released in a standard oxidizing atmosphere and has high strength and toughness to permit the extensive handling and manipulation of the green tapes.

Plasticizers: The plasticizer additive increases the green tape flexibility to prevent cracking during drying and handling. The plasticizer improves the ductility of the tape to prevent shattering during machining by allowing alteration of the tape matrix without failure. There are two types of plasticizers utilized in tape casting: (1) Type I: softens polymer chains to allow stretching more easily (flexibility), (2) Type II: permanent motion of the matrix (plastic deformation).

This is illustrated in stress strain curve of the tape in Figure 26. The Type I is represented by the linear portion of the stress strain curve, below which the tape will return back to its original shape without permanent deformation. The Type II plasticizer adds a curved section to the stress strain curve that represents the materials ability to plastically deform prior to failure. All stress applied above the material's yield strength induces a permanent strain that cannot be recovered, but plastic deformation will prevent the brittle failure (cracking) of the tape. The combined use of Type I and II plasticizers permits the manufacturing of a both flexible and plastic tape, respectively.

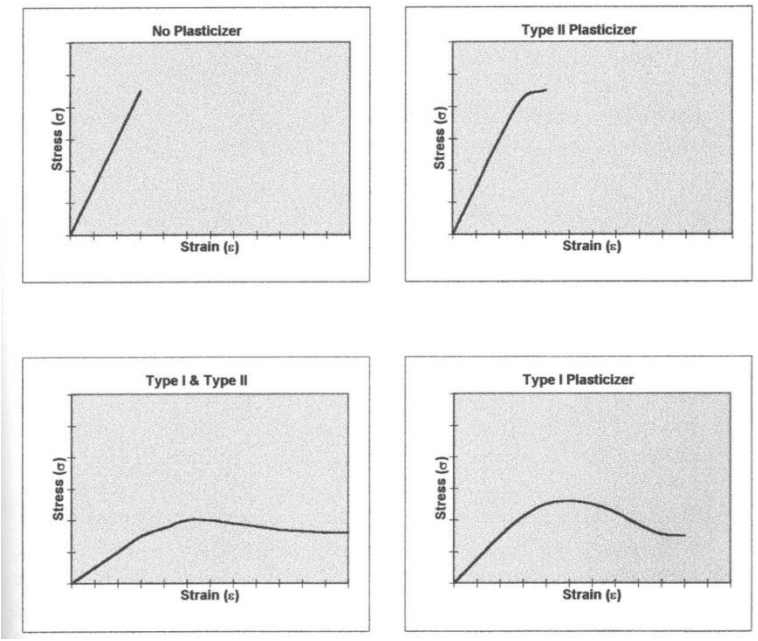


Figure 26 Stress Strain Curve Plasticizer Comparison [15]

The plasticizer's polymer chains are strings with a backbone of carbon atoms bonded together by strong covalent bonds. Hydrogen and potentially other elements are branched off the backbone. The weak VDW forces join the hydrogen bonds and hold together the polymer chains. Cross-linking of the polymer chains via covalent bonding makes the structure more rigid.

The glass transition temperature (T_g) of a polymer is the point at which the weak VDW bonds start to melt. The Type I plasticizer decreases the T_g of the solution to below the processing temperature. The T_g is influenced by the type of chain entanglement in the polymer binder matrix (linear or branched), molecular weight, cross linking strong covalent bonds and the weak VDW bonds. The elastomer tape's VDW bonds are essentially melted, and the structure is held together primarily by the cross-linked backbone. The cross-linked bonds, in the absence of the VDW bonds, permit the stretching of the matrix.

The Type II plasticizer prevents some of the strong cross-linked bonds from forming and acts as a lubricant to facilitate the movement of the polymer chains within the green tape. Without the domination of these cross linked bonds the polymer chains are easily ordered into an organized structure during plastic deformation.

The drying of the tape occurs when the solvent is evaporated out the top of the tape which is exposed to the air. The bottom surface is bonded to the carrier sheet, restraining the shrinkage of the material and causing internal stresses. These stresses can cause the tape to release from the mylar carrier prematurely, edges to curl and the green tape to crack. The Type II plasticizer lowers the yield stress to allow the material plastically to deform and alleviate the internal stresses.

The Type II plasticizer has also been reported to reduce shear thinning effects by lubricating the particles to facilitate sliding. "Type II plasticizer can aid flow under the doctor blade and avoid streaks or grooves in the green tape, since pseudo-plasticity, thixotropy, and even dilatancy are caused by binding forces in the fluid." [15] The lubricant can also aid in releasing the thin film from the Mylar carrier layer. Excessive levels of Type II plasticizers may result in phase separation and a stiff tape.

Organic Interactions: The binder also acts as a dispersant, joining the ceramic particles with long polymer chains in a matrix which also functions to hold the particles apart. It is critical to disperse the ceramic particles evenly throughout the solution prior to adding the binder to avoid the "zipper bag effect". The zipper bag effect is caused by an agglomeration of ceramic particles that were not broken up prior to being introduced to the binder. The binder will not break this agglomerate but rather form its matrix around the cluster locking them in with

permanent bonds. It gains its name from the correlation of putting an agglomeration of particles into a zipper bag. The particles can be broken into several pieces but cannot be removed from the zipper bag without breaking the seal. The particle agglomerates will not be re-dispersed into the bulk material. These larger particle clusters do not pack as effectively in the green tapes, lowering the green tape density. The particle clusters also require more energy to begin the sintering process due to the low surface area per unit volume.

When polyvinyl butyral binder is used with the MFO dispersant the binder will replace some of the dispersant on the particle surfaces, absorbing the binder and dissolving the dispersant back into the solution. The amount of binder available for forming the polymer matrix to absorb the ceramic solids is therefore diluted, and requires the addition of more binder to accomplish this same solids solubility level. The increased level of MFO in solution acts as a lubricant to allow the slipping of bonds (plastic deformation). The decreased level of binder in solution available to form the matrix weakens the structure, making the tape more prone to cracking.

The binder reacts with the plasticizer Type I but not the Type II. This reaction lowers the T_g of the slurry to improve the tape's flexibility. Minimal effects due to the dispersant and plasticizer interactions can be neglected due to the domination of the other organic interactions discussed.

Ball Milling: The electrolyte slurry is ball milled in a two stage process to ensure an evenly dispersed homogeneous solution is produced for tape casting. Ball milling spins a cylindrical bottle filled with the slurry and small, dense milling media balls on two rolling pins to mix the solution.

The shearing effects in ball milling are a factor of the milling media size, milling container diameter, rotational velocity and milling period duration. The milling media balls must be fabricated out of a dense material that will not react with the solution and contaminate the batch. A container with a larger radius and more rapid milling rotational velocity increases the acceleration of the milling media, and in turn the shearing force. The milling rotational velocity can be simply detected when the milling media hits the sides of the container during milling to create an audible sound.

The solvent, dispersant and ceramic powder are mixed in the first cycle separately, to ensure the proper dispersion of particles is obtained, prior to introducing the binder which sets the particles into permanent bonds. The solids loading in the slurry is calculated as the powder weight divided by the combination weight of the solids and solvent.

$$\%\, Solids = \frac{Powder\ Weight}{(Powder\ Weight + Solvent\ Weight)}$$

Equation 14 Solids Loading

The dispersion stage has three separate stages which the slurry goes through. First the ceramic particle surfaces are coated and the weak VDW electrostatic bonds are broken. Second the ball milling media breaks the primary bonds through the mechanical shearing of the balls falling through the liquid. The third and final stage is the wetting of the particles to continually prevent the reformation of the VDW bonds.

Time is a critical factor in ball milling due to the organic interactions within the slurry. In the dispersion stage it is essential to mix the solution long enough to ensure all the ceramic particle clusters' VDW bonds are broken. The second milling stage must be sufficiently long enough to allow the homogeneous distribution of all constituents and allow the binder matrix to

be constructed. It must also be long enough to facilitate the reaction between the plasticizer and the binder, lowering the slurry T_g to improve tape flexibility. A second stage too short will result in a stiff and weak tape. However a long second stage milling period will result in the replacement of the small dispersant polymer on particle surfaces with the larger binder polymer, breaking down the binder matrix and weakening the slurry bonds. The excessive second stage will then introduce the dispersant to the bulk solvent to act as a lubricant facilitating plastic deformation, resulting in a tape too conducive to plastic flow. The ideal second stage milling period will completely dissolve the binders and plasticizers and then be stopped to avoid dispersant displacement.

Slurry De-Airing: The preconditioning of the electrolyte slurry is required to ensure a batch free of large particles and air bubbles is poured into the tape cast reservoir. The large particles are removed by simply pouring the slurry from the ball milling container through a fine mesh filter into an open mouth container. This open mouth container is then immediately inserted into a vacuum chamber to degas the slurry. The removal of air bubbles and particles are essential to avoid streaks and thin regions to form in strips in the casting direction due to obstructions under the doctor blade. The air bubbles can become trapped within the bulk material and will result in a void during sintering. The voids and flaws create regions for cracks to form and propagate from. Agitation of the slurry during de-airing of the slurry can assist in the evacuation of air bubbles. The volume cannot be pumped too high as this will result in the loss of material that is transported away with the violent release of air bubbles.

Tape Casting

Tape casting is a process which produces flat, thin film ceramic substrates on top of a carrier surface at the desired thickness. Figure 27 is a schematic of a continuous tape caster, where the carrier surface is pulled underneath the stationary doctor blade.

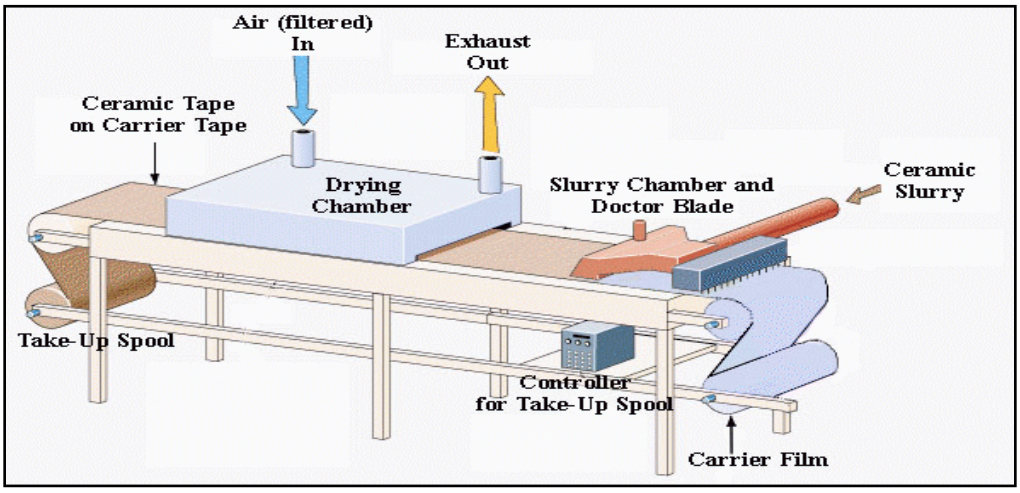


Figure 27 Tape Casting Schematic [15]

The ceramic slurry is poured into the doctor blade slurry reservoir (slurry chamber) on the carrier surface and is pulled underneath the precisely adjusted doctor blade to thin it to the desired thickness. The carrier surface and freshly applied thin ceramic film are then pulled over the tape casting bed and may pass under a drying bed when necessary.

The amount of slurry, doctor blade width and desired tape thickness will determine the length of tape that will be cast. If it is less than the length of the tape cast bed it can be stopped on the flat drying bed until all the solvent has evaporated and the drying process is complete. This is called batch tape casting and was used exclusively in the fabrication of the UniCell electrolyte tape. When the operator would like to cast a tape longer than the caster bed, and the bed length and feed rate permits complete drying of the tape prior to the end of the drying bed,

the carrier and the thin film ceramic layer can be rolled onto a take-up spool. This is continuous tape casting and is especially useful in industry when production rates are of great importance.

Equipment: The laboratory tape casting equipment resembles the industrial line utilizing the same general procedures; however they lack the production capability of extremely long tape casters, precise monitoring of reservoir level, exact control of the drying bed temperature and a sophisticated air ventilation system. The first step of the tape casting process involves the delivery of the previously prepared slurry. In the laboratory setting it is common to just pour the slurry directly into the doctor blade feed reservoir. Therefore the delivery of the slurry from a vacuum storage chamber to the feed reservoir will not be discussed despite its major role in commercial systems.

The doctor blade assembly sits stationary on top of the moving carrier surface with a precisely machined granite block below to ensure a smooth, flat support is provided to the carrier surface. The double doctor blade system utilizes an inclined surface that goes all the way to the surface, and the first doctor blade to form the reservoir to store the slurry.

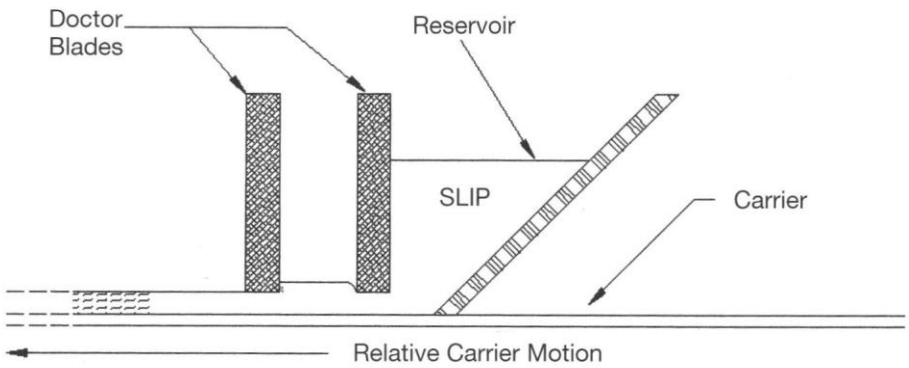


Figure 28 Double Doctor Blade Assembly [15]

Its reservoir stores the slurry in contact with the moving mylar carrier. The second doctor blade is placed after the first with a space between the two to create the casting pool. The second doctor blade and casting pool are utilized to control the fluid level. This will be discussed further in the proceeding section. The second doctor blade meters the slurry onto the moving carrier surface at a specified thickness.

The two doctor blade heights can be controlled with a micrometer or feeler gauge to alter the thickness of the tape cast film. The doctor blade is adjusted down to the flat surface below and then raised with the micrometer to obtain the desired blade gap. Several designs exist for the doctor blade tips with varying thicknesses and shapes. Doctor blades can also be constructed from a wide range of materials, but careful attention must be paid to ensure the material doesn't chemically or physically react with the slurry constituents and the bottom of a flat bottomed blade is ground flat and smooth. An in depth discussion of the varying doctor blade types and styles will not be discussed as it was not a parameter varied throughout the manufacturing of the UniCell electrolyte. However investigation of different tip styles and blade technology should not be neglected in the commercial development of a tape casting procedure for producing SOFC layers.

The tape casting bed provides a flat surface for the carrier surface to pass over during the continuous tape casting process to facilitate evaporation of the solvent. The bed temperature can be varied to obtain different tape microstructures due to the different evaporation mechanisms of the solvent. For example, freeze casting cools the bed with cooled liquid methanol to freeze the aqueous solvent which can be removed via freeze drying, creating a microstructure of aligned

pores. A heated bed can aid in the drying of the tape on the bottom to eliminate temperature gradients in thick tapes which can cause cracking.

The carrier material the thin film is cast on top of provides several critical functions. The carrier must have a smooth surface, prohibit chemical and physical interactions with the tape slurry and permit the release of the tape once it is dried. The MSU tape casting system utilizes a silicon coated mylar sheet as the carrier surface.

Physics & Procedures: The tape casting procedure is very simple in concept. However the extensive list of variables that need to be controlled to create the desired tape can be overwhelming. When the processing variables (doctor blade size and shape, blade height, casting speed, reservoir height, slurry-mylar wetting behavior and surface tension) are combined with the slurry variables (viscosity, homogeneity and rheological properties) a plethora of combinations exist. The homogeneous of the slurry mixture will translate directly to the homogeneous distribution of the slurry constituents in the tape cast film. Additional settling of the higher density constituents during the drying process may create a variation in the tape in the z direction.

The four variables that dominate the control of the wet tape thickness are: (1) doctor blade gap and thickness (2) reservoir height (3) slurry viscosity and (4) casting speed. The doctor blade gap and thickness dominate the wet tape thickness, but the effect of the other three parameters can be significant.

The height of the doctor blade is also referred to as the doctor blade gap as it measures the distance between bottom of the doctor blade and carrier surface. The size of orifice that is created determines the amount of slurry which can flow under the blade. As the carrier moves it

pulls a certain amount of the slurry under the doctor blade. When the velocity of the carrier (casting speed) is equal to the velocity of the slurry the wet tape thickness is equal to the blade gap. If the velocity of the carrier exceeds the slurry velocity the tape thickness will be less than the blade gap, and vice versa.

The carrier speed should remain consistent throughout the tape casting to ensure a consistent thickness. To ensure the speed is steady the tension in the carrier layer must not vary, otherwise the carrier velocity will vary to take up the tension despite a steady force pulling the carrier.

When the wet tape thickness is greater than the blade gap the phenomenon is called welling, where a boundary layer of the wet tape forms on the outside edge of the doctor blade. The blade gap is the dominant force in determining the thickness of the wet tape. However the doctor blade thickness and slurry viscosity determine the shearing force applied to the slurry during casting. The thicker the blade the more surface area acting on the fluid, and in turn the higher the shearing force is. As the shearing force increases, the likelihood of welling to be present decreases.

The height of the doctor blade can be set manually by human adjustment of a micrometer each time a tape is cast, controlled by a computer mechanical system or fixed permanently. Each time it is adjusted by a human it subjects the process to human error. Once a desired height for the doctor blade is determined it is recommended to utilize a fixed doctor blade to ensure consistent results.

The slurry that is stored in the reservoir creates a hydrostatic pressure, or head, in the fluid. It is this pressure which causes the fluid to want to flow through the doctor blade gap. As

this pressure increases more slurry is forced out the orifice and the slip velocity is increased, increasing the wet tape thickness. The hydrostatic pressure (P_{hydro}) is a function of the slurry volume (V_{slurry}), slurry specific gravity (γ_{slurry}) and orifice area ($A_{orifice}$). The volume is a function of the reservoir fluid height and mass of the slurry.

$$P_{hydro} = V_{slurry} * \gamma_{slurry} * gravity / A_{orifice}$$

Equation 15 Reservoir Hydrostatic Pressure

The slip friction, a function of slurry viscosity and blade thickness, counteracts this pressure. The effect of the hydrostatic pressure on the wet tape thickness can be minimized by increasing the blade friction to a level significantly above the hydrostatic pressure.

The exact control of the reservoir height is necessary to obtain a consistent wet tape thickness from batch to batch, but also within a single tape. Therefore the beginning and end of the tape is cast when the reservoir height varies from the middle of the tape, altering the tape thickness profile along the length of the tape in the cast direction. Long tapes with a large region where the reservoir height was consistent typically exhibit a stable tape thickness profile within this middle region.

The viscosity of the slurry is a measure of the liquid's ability to resist change in form and flow. The viscosity of the slurry is highly dependent on the processing temperature because it is based on the glass transition temperature (T_g). The T_g is modified by the plasticizer content and hence modifies the slurry viscosity. The viscosity is also a factor of the ceramic powder surface area and preparation methods as discussed previously. The viscosity affects the wet tape thickness due to its effect on the slip friction (which offsets the hydrostatic pressure to eliminate welling).

The viscosity of the slurry varies throughout the tape casting procedure since it is dependent on the shear forces applied. The slurry will have a lower viscosity under the doctor blade where shear forces are highest versus in the bulk tape after it has been pulled onto the casting bed to dry. This is important to ensure the tape resists motion due to a higher viscosity after it has been cast.

The surface tension between the carrier surface and the slurry film determine the behavior of the film after it has been formed. It is a balance of the forces acting on the fluid at the liquid/solid/air interface that is necessary to obtain a uniform layer prior to drying. If the forces are not balanced material on the edges will flow, causing the edge profile to vary and changing the overall tape's surface area and thickness profile. The slurry viscosity, specific gravity and rheology modify the contact angle between the carrier and the slurry, in turn the surface tension which holds the slurry in the form it was cast. Increases in any or all three of these material properties, increases the resistance to motion.

Drying: The drying of the tape on the casting bed is the solvent evaporating vertically away from the mylar sheet towards the air interface. Since the solvent can only evaporate from the top surface it must diffuse through the bulk material to the drying surface. The rate of evaporation at the surface and diffusion rate through the bulk material are the major driving mechanisms in tape drying. The diffusion through the bulk material is the rate limiting factor. When the evaporation rate far exceeds the diffusion rate a skin will form on the surface where the solvent has been totally evaporated from, slowing down the evaporation rate and increasing drying time. To avoid the skin formation the rate of diffusion and evaporation rates must be as

close to equal as possible. This allows a uniform distribution of the solvent in the bulk material to ensure all the parts dry at the same rate.

The rate of evaporation at the tape's surface is controlled by the choice of solvent (volatility level), concentration of the solvent vapor in the local atmosphere and temperatures of the air and solvent. The reaction to evaporate the solvent requires energy, and increases in temperature add energy to the system and increase the volatility of the solvent, therefore increasing the evaporation rate. As the concentration of the solvent in the local atmosphere increases and reaches saturation levels the rate of evaporation decreases. The concentration of the solvent in the sample will increase the magnitude of curling.

The diffusion rate through the material is altered by varying the binder concentration, ceramic particle size, temperature of the casting bed and pore structure. The solvent requires pathways to travel through to the surface, and as the tape dries and compresses these pathways shrink, slowing the diffusion rate. Increases in the casting bed temperature will increase the energy within the wet film to promote diffusion.

As the tape dries the bottom surface is restricted from shrinkage in the lateral directions by the carrier surface. The top surface is held in tension by motion along the cast direction if a continuous tape casting method is used, but in the UniCell batch casting there is no tension in the cast direction. The top surface is also free to shrink in the cross cast direction. This difference in shrinkage of the tape creates internal stresses that store energy in the form of strain. In batch tape casting the rate of drying is only important in the effect it has on the internal stresses, since it is not necessary to dry the tape quickly to allow the continuous production. When strain energy exceeds the bulk material's ability to store strain energy the tape will curl on the edges, and then

release from the mylar, crack, curl in the body and wrinkle. The Type I plasticizer stores elastic energy. The polymer matrix ability to store energy through plastic deformation is determined by the bulk material's T_g, which is controlled by the Type II plasticizer.

Surface Contouring

The surface of the UniCell electrolyte was altered to include the interleaved channels (see page 56 for more details). Laser micromachining and photoresist machining (PRM) in both the green and the dense sintered ceramic states were investigated to develop a working UniCell prototype model. Laser micromachining removes surface material with a high power, finely focused light beam. High quality laser micromachining of green SOFC electrolyte tapes is an excellent potential candidate for production of the UniCell. PRM coats a dense substrate with a photoresist film, treats it with ultraviolent light and solvent to remove the feature shapes and blasts the exposed surface with sand to remove the material. PRM is a simple process capable of rapidly machining blind features into dense sintered ceramics.

Laser Micromachining: Laser micromachining offers several advantages that make it appealing to the SOFC fabrication industry. A laser processing module can be integrated to sheet fed material handling systems, such as a tape cast system for production of green ceramic SOFC tapes, allowing inline process surface contouring. High precision laser micromachining is capable of surface contouring the ceramic body without the need to utilize tooling to die cut the part as in standard metallic machining. The tool free process allows for tighter arrangement of surface features. The replacement of the die with a finely tuned aperture laser, that produces short pulses of light, permits the removal of material in minuscule paths or holes.

A laser shoots electrons along a fine beam field of noble gases that do not react with their surroundings. Laser micromachining removes material from the bulk ceramic body with ultrafast pulses of light focused into a high power beam. The laser micromachining beam introduces energy to the system which vaporizes the material by breaking the molecular bonds on the surface with each pulse. The material's surface electrons are excited and evaporate first, followed by the ions. A strongly bonded dense material provides a high level of resistance against the laser beam, releasing wasted energy in the form of heat conducted into the bulk material. When excessive amounts of heat is produced the process no longer goes straight from the solid to vapor phase, but rather the ceramic melts from the solid to liquid phase and then boils from the liquid to vapor phase.

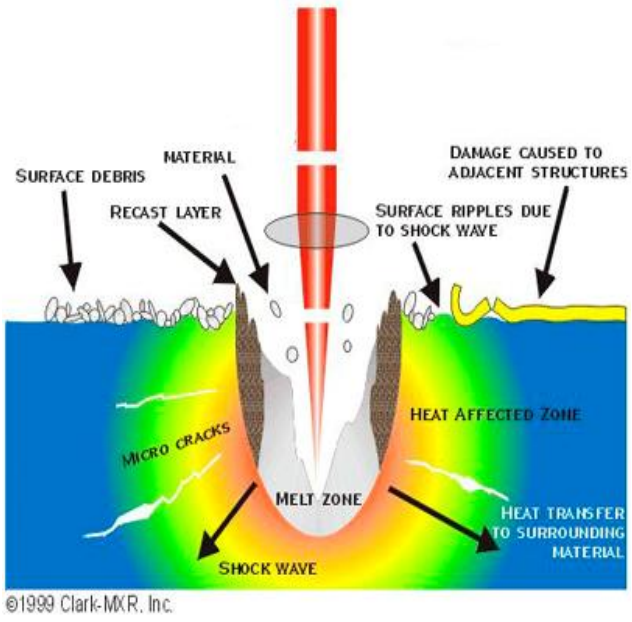


Figure 29 Laser Pulse in Dense Ceramic Substrate [19]

As the heat diffuses away from the feature through the bulk material it can cause damage as illustrated in Figure 29. The quality of the introduced laser drilled features is a function of the

amount of heat that is left behind in the material. The area around the edge of the laser drilled feature, when introduced to high amounts of heat diffusion, becomes the heat affected zone (HAZ). When the material enters the liquid phase boiling molten material will be ejected from the bulk material and contaminate the surface by bonding to it while still hot. These blemishes can be very difficult if not impossible to remove. The shape of the melted region is not limited to the laser beam spot size, making it very difficult to control the shape of the features and reducing the overall process accuracy.

The re-solidified material in the HAZ has a different microstructure, and in turn potentially different functional properties. The thermal stresses during rapid heating and cooling in the HAZ can also create micro cracks that are locked into the material during cooling. These micro cracks can cause premature failure of parts due to crack propagation. The heat diffusion rates can eventually reach such high levels shock waves will travel through the material.

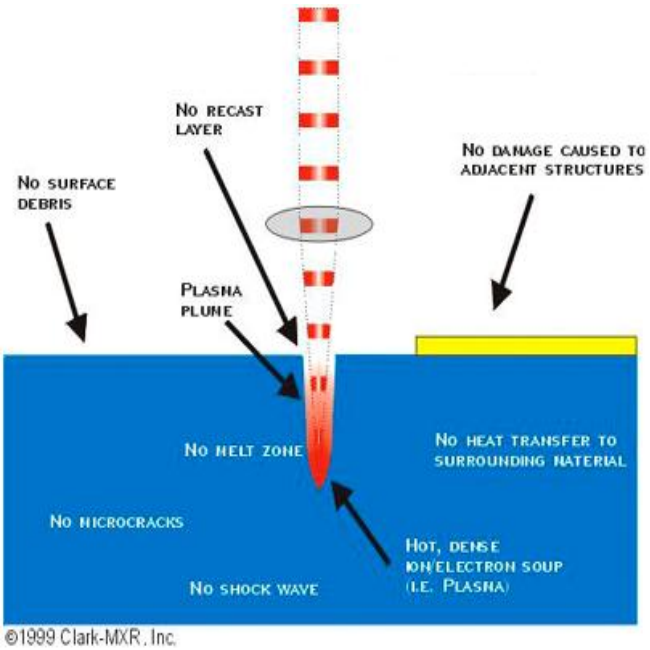


Figure 30 Laser Pulse in Green Ceramic Substrate [19]

To ensure the minimum amount of heat is diffused into the sample the required duration of laser machining pulses must be minimized and the resistance to transfer the heat into the material must be maximized. The required duration of laser machining is a function of the laser pulse energy, material bond strength and the machined feature's length, width and depth. Lasers with short wavelengths can deliver the same amount of energy in shorter pulses with more frequent breaks to allow additional time for cooling, and avoid the bulk material from heating up to its melting point. An efficient laser vaporizes all the material into a plasma plume, leaving behind only small amounts of heat that can be dissipated through the gas between pulses. The resistance to transfer heat into the bulk is dependent on the material's thermal conductivity, where materials with a higher thermal conductivity waste more energy due to heat absorbed during laser micromachining. Minimal heat diffusion into the body results in a more efficient, accurate and cleaner process without introducing thermal stresses to the part (see Figure 30).

Several different forms of lasers are used in industrial applications today. The excimer laser beam pulses excited electrons to the sample in 10 nanosecond pulses, limiting the amount of heat produced and making it conducive to micromachining. YAG lasers utilize Nd:$Y_3A_{l5}O_{12}$ as the gas medium to pump electrons in ~ 750 nm pulses and are the most popular form of lasers, but have poor tolerances compared to other micromachining lasers. A CO_2 laser pumps electrons through a beam of carbon dioxide in pulses as long as 1000 nm. A CO_2 laser is capable of drilling microvia holes with a minimum diameter of 50 microns, and an excimer laser can drill as small 2 micron diameter holes. These both can be accomplished at up to 140 microvias per second. [20]

Photoresist Machining (PRM): PRM removes material from the surface through sand blasting. A light sensitive photoresist film is placed on the surface of the substrate and then exposed to ultraviolet light through a photographic negative which blocks the passage of light in the desired feature profile areas. The photoresist material that is exposed to the light hardens, and the remaining area of the photoresist film is soluble to a solvent. The surface is treated with the solvent that removes the unhardened areas. An etching nozzle then passes over the substrate and blasts the surface with high intensity pulses of sand. (See Figure 31) The material removal rate is dependent on the abrasive material, substrate material, abrasive material beam intensity and desired feature profiles.

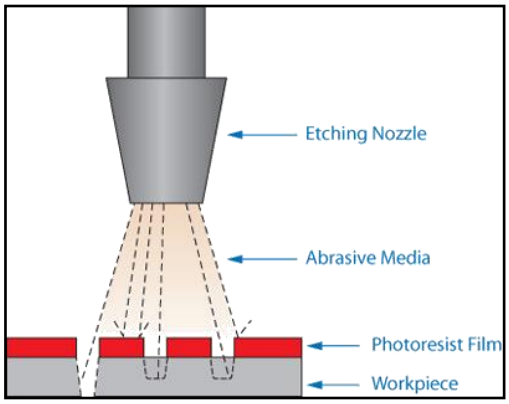


Figure 31 Photoresist machining etching nozzle diagram



Figure 32 Photoresist machining station[21]

PRM is used to remove material from hard and brittle surfaces such as the surface of a sintered SOFC electrolyte. Depth uniformities possible are within approximately 50 microns across a 30 cm length. PRM provides several advantages over other alternatives such as simplified operation, rapid processing speeds, profile uniformity and a low tendency for chipped edges and micro-cracking. Figure 33 displays a dense ceramic part that was easily textured with blind holes in the center section and then framed with PRM. The actual part was 4.5” square and

took about 15 min to etch. The entire process took about 30 min. To increase manufacturing productivity even further multiple parts could have been processed at the same time. [21]

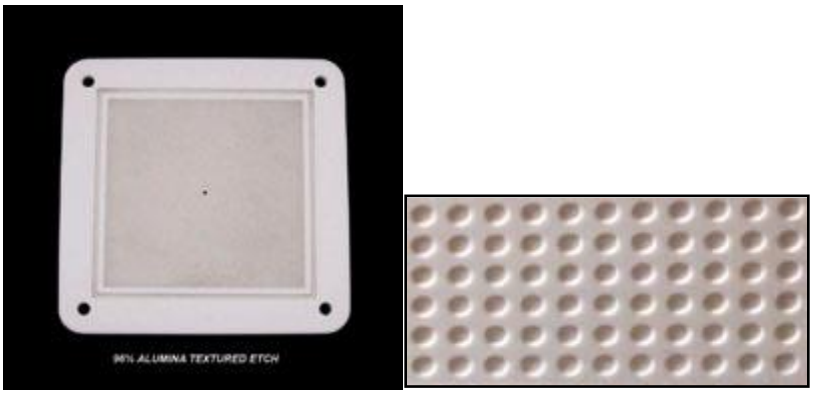


Figure 33 Photoresist Texturing of Alumina Substrates [21]

Alternative Methods Considered: Several additional techniques such as tape calendaring, ultrasonic machining, hot press stamping and slip casting are also potentially capable of manufacturing the UniCell with the surface inclusions.

Firing Process

Green ceramics are heat treated to obtain a part with the desired microstructure and properties. The UniCell was fired in two separate stages: (1) firing of the green electrolyte tape (2) co-firing of the green electrodes air brushed onto the pre-fired electrolyte. Both of the firing processes have three distinct stages the ceramic goes through: (1) pre-sintering reactions (2) sintering and (3) cooling. The pre-sintering stage decomposes the organic polymer binder matrix and burns out all of the additives required during tape casting and air brushing to manufacturer the ceramic powders into their desired form (binder, plasticizers, dispersant and solvent not evaporated during tape drying). The second stage sinters the ceramic powder, at a temperature

below the melting point, to adhere the ceramic particles to each other, altering the microstructure and increasing strength.

The heat cycle consists of a series of three stages, all of which affect the growth of grains and sample density: (1) Ramping up to a higher temperature at a controlled ramp rate (2) dwelling at a set point temperature for the desired dwell time and (3) cool down to a lower temperature at a controlled rate.

Pre-Sinter Firing Stage: The pre-sintering stage consists of three distinct reactions: (1) evaporation of excess liquid left behind (drying) (2) binder matrix decomposition and (3) organic burnout. The rates of binder decomposition and organic burnout are dependent on the binder composition and structure, the temperature and composition of the atmosphere and the gas within the pores of the part, and the heating rate. The decomposition of the binder starts with the melting of bonds in the polymer matrix at elevated temperatures. The increase in temperature introduces energy to the part to permit the reactions between the organic constituents and the gas in the chamber. Increasing the rate of energy introduced to the system is used to accelerate the ramp-up rate (°C/min) and decrease the overall firing time. The extra energy introduced to the system at rapid ramp-up rates results in the volatile organic burnout.

Internal stresses within the part during the first stage of firing are a result of two things: (1) the release of these organics creates a back pressure of the gas trying to evacuate the part and (2) difference in thermal expansion coefficients of the different phases present. The safe burnout rate of the organics also depends on the part's permeability, which determines the back pressure built up of gases trying to escape. The internal stresses can cause voids, a source for cracks to

form within the structure. The cracks can then propagate and fracture causing the part to fail during further handling or under normal operating stresses.

Solid State Sintering: Sintering converts the green ceramic bodies into the solid SOFC components by thermal treatment in the solid state (below the material's melting point). There are three distinct stages of sintering: (1) neck formation (2) densification and (3) grain growth. Sintering is driven thermodynamically by the reduction in total free energy in the system. In between the spherical particles of a green body is a solid-vapor interface with a high surface energy. With the introduction of a certain amount of heat energy to the system mass will transfer between particles in contact with one another. The particle surfaces will be smoothed and particles will deform shape and neck together to reduce the surface area per volume of ceramic material. Neck growth will lead to the formation of grain boundaries, which have a lower energy than the particle surfaces.

In the densification stage most of the porosity is removed as the interstitial vacancies migrate to the grain boundaries and are annihilated. The grain boundaries are unordered particles with a lower energy than the particle surfaces, but a higher energy than the grains. The final stage of sintering is the growth of the grains and overall reduction of grain boundaries. The final particle has no open porosity; the only remaining pores are contained in the grain boundaries. Eventually these pores will all shrink and disappear. The grains will finally start to grow rapidly. Ionic conductivity is improved with the increase in grain size, however the material becomes less resistant to brittle failure.

The homogeneity of the green body plays an important role in sintering. If large flocculants of particles exist within a structure with varying pore densities the body will sinter at

different rates. The large pores within a dense section of the small grains shrink much slower than the small pores surrounded by larger grains. As sintering occurs uneven shrinkage within the body can create large stress regions that can result in rapid propagation of a crack during thermal treatment.

In a SOFC the co-sintering of all three ceramic green bodies (anode, electrolyte and cathode) is very difficult to accomplish. The electrolyte and electrode layers require different microstructures to perform their functions. The electrolyte layer must be dense, without a continuous pore structures or any pin holes, to ensure the gas and air flows do not mix. This requires the high temperature processing to complete all three sintering stages. On the contrary, the electrodes must be porous to permit the transport of gas through to the electrolyte three phase boundary.

High temperature processing can also result in the undesired migration of electrode materials through the electrolyte interface. This can negatively affect the functional properties of the materials, sacrificing the cell's electrochemical performance. Migration of the LSM cathode into the YSZ is not encountered until approximately 1400°C. This is well above the operating temperature but below the required processing temperature of the electrolyte and therefore eliminates the ability to co-sinter the entire cell at once. Novel materials for the cathode have been developed to permit the co-sintering of the entire unit cell and reduce processing times and cost.

Ceramic Mechanical Properties

The ceramic materials used to fabricate the UniCell must exhibit adequate mechanical durability to withstand stress levels encountered in SOFC fabrication and normal operating

environments relative to: (1) thermal expansion (2) fabrication handling (3) vibration forces and (4) impact shock. The thermal expansion stresses build up between layers in the fuel cell stacks due to varying coefficients of thermal expansion for electrodes, electrolytes, seals and interconnects during high temperature fuel cell fabrication and operation. All ceramic material properties are dependent on the atomic, microscopic and macroscopic texture that is optimized by changing the fabrication process techniques. The atomic arrangement of the ceramic is based on the type of bonding, sizes of atoms and electrostatic charges.

Ceramic Bonding: Ceramic materials exhibit high yield strengths and low toughness against crack propagation. This is a direct result of the nature of ionic and covalent molecular bonds' ability to resist atom movement. An ionic bond is the electrostatic attraction of two oppositely charged ions, where one ion donates a valence electron to another ion. The strength of the bond is directly proportional to the electro-negativity of the atoms and distance between the atoms. Ceramic atoms with a higher electro-negativity have a strong tendency to form ionic bonds. Ionic bonds are typically highly symmetric and non-directional (isotropic). The covalent bonds are the strongest type of bonds, where two ions share valence electrons, because neither atom has a tendency to give up an electron completely. The overlapping of the outer valence shells results in a highly ordered and directional covalent bond.

Mechanical Failure: Ceramics exhibit a long linear section of the elastic stress strain curve, followed by little or no plastic deformation prior to brittle failure. The linear elastic behavior is related to the bonds ability to stretch and recover completely when loading is removed. The plastic deformation is caused by two rows of atoms slipping under stress and

dislocating to the next available position. Ceramics do not permit line dislocations due to the directionality of the covalent bonds. Significant plastic deformation is not possible at low temperatures in ceramics, but as the temperature increases the material becomes more ductile.

Dislocations start as a defect within the microstructure. There are two types of defects: (1) point defects and (2) line defects. Point defects are caused by vacancies in the crystal structure and impurities. For example YSZ has oxygen vacancies within the material due to the replacement of zirconia lattice sites with yttria. As the concentration of the yttria increases the concentration of oxygen vacancies increases decreasing the overall strength of the material, therefore 3 mol % YSZ is 4 times stronger than 8 mol % YSZ. Line defects, also referred to as dislocations, are deleterious to the material permitting deformation to occur at much lower stress state than in a perfect crystal. As the dislocation moves through the lattice it progressively breaks bonds. When too many bonds are broken from dislocation motion and plastic deformation reaches its maximum value the ceramic material will catastrophically fail.

Brittle failure, or cleavage, is commonly found in materials with high yield strength that do not permit plastic deformation, such as ceramics. A small, sharp crack starts in a material at line defect and propagates along a slip plane within the lattice structure. As the dislocation crack propagates it spreads between the atomic planes yielding an atomically smooth surface. The maximum stress applied to the material occurs at a 45 degree angle from the force vector. The material will fracture at the slip plane oriented closest to the 45 degree angle. The region of material at the crack tip can absorb the energy of the propagating crack by plastically deforming and work hardening the area. When the work hardening area strength exceeds the energy of the

crack it will be stopped. Ceramics are not conducive to plastic deformation, prohibiting the absorption of crack tip energy and causing brittle failure in tensile loading.

Ceramic Microstructure: The microscopic structure of ceramic grains has a profound effect on the mechanical behavior of the part. The single crystal grains are randomly oriented and combined by grain boundaries. The grain boundaries are intrinsically weaker than the grains however the part is much stronger than a single crystal due to the grain boundaries. Grain boundaries are a sink for structural defects, pores and second phases. The impurities within the material segregate to the grain boundary further weakening this region.

There are two distinct modes of failure through a sintered ceramic: (1) transgranual fracture and (2) intergranual fracture. Transgranual fracture is due to cracks propagating through the grain boundaries. This is the dominant mode of failure. Intergranual fracture is the crack propagating through the grains rather than the grain boundaries. The ceramic materials in SOFCs consist of randomly oriented grains. Since dislocations slide along slip planes and adjacent grains are not aligned, the dislocation cannot simply transfer from grain to grain. The grain boundaries provide an added resistance to dislocation motion forcing the dislocations to nucleate in the grain to travel in a new direction. As the crack propagates through the grain boundary a tortuous path can cause the crack to run into a grain perpendicularly. This will stop the crack until the energy is increased to a level higher than the intergranual resistance. Therefore the material toughness can be increased by engineering the grain size.

Analysis Techniques

Several state of the art analytical techniques have been applied to optimize the UniCell fabrication methods. Field emission microscopy allowed careful inspection of the component microstructures. Thermal gravitational analysis and dilatometer analysis techniques were employed to study the various effects of temperature on ceramic processing. Mechanical strength testing of brittle ceramics was accurately characterized in an Instron materials testing machine utilizing a concentric ring sample mount. Electrochemical testing was used to characterize the performance of unit cells under operating conditions. To provide the reader with a general understanding of these advanced technologies yet remain within the scope of this paper only a summary of these techniques will be presented. A detailed description of the application of these techniques is covered in 0 - Experimental Procedure.

Field Emission Microscopy (FEM)

Field emission microscopy (FEM) uses an electron microscope to analyze molecular surface structures. A scanning electron microscope (SEM) excites the low energy secondary electrons on the surface with a primary electron beam. An SEM produces an image map through rastering across the surface with the detector to measure the electron intensity as a function of position. An electron microscope can obtain images at extremely high magnifications of up to about two million times. FEM uses a sharp needle emitter and is frequently used in an SEM as the source of electrons due to the very small area over which the electrons are emitted. This leads to improved spatial resolution and minimized sample charging.

Thermal Gravitational Analysis (TGA)

Thermal gravitational analysis measures the change of mass of a small sample due to thermal treatment. The sample is stored in an aluminum oxide crucible centered in a vertical tube furnace. The TGA balances the sample holder with an arbitrary load on the opposite balance arm. A linear actuator measures the change in position of the balance arm due to a variation in the weight of the sample unbalancing the scale. This change in position is correlated to the change in mass of the sample.

A TGA is extremely responsive, allowing the detection of milligram weight changes as a result of oxidation, organic burnout, water evaporation, etc. Due to the nature of the balance design, the TGA is highly sensitive to the stability of the mounting table. Slight external forces can cause swaying of the balance and undesired test noise. TGA data is applied to materials engineering of the UniCell to limit reaction rates and stabilize ceramic processing techniques.

Dilatometer Analysis

A dilatometer detects the change in a samples length due to thermal treatment. The sample is sandwiched in the sample mount centered in the tubular furnace. The sample rod is held in place with a predetermined minimal force. During the introduction of heat to the system the sample will contract or expand dependant on its physical state. When the samples shrinks or contracts a linear actuator monitors the change in sample length. Dilatometer analysis data contains the material's CTE and can be used to optimize sintering cycles to minimize internal and interlayer stresses.

Instron Materials Testing Machine

An Instron universal materials testing machine is capable of conducting compressive and tensile strength tests. The force required to displace a sample is closely monitored and can be correlated to the ultimate yield strength. Due to the brittle nature of ceramics the ultimate yield strength tests are significantly affected by loading method. A concentric ring on ring sample mount evenly distributes the applied force over the rings, creating a more consistent failure distribution.

Fuel Cell Performance Testing

Fuel cell performance testing is an essential task in evaluating and comparing SOFC designs, materials and operating conditions. An electrochemical test stand is capable of characterizing the performance of solid oxide unit cells. Long duration SOFC operation allows the researcher to generate a V-I scan and collect ASR data. Electrochemical V-I scans characterize the polarization losses of the SOFC unit cell. For more details refer to "SOFC Electrochemical Performance" on page 14.

UNICELL DESIGN

Problem Overview

SOFC manufacturers require a stack configuration that increases cell power density, by minimizing ohmic polarization in the electrolyte and concentration polarization in the anode, while providing adequate mechanical strength to endure unit cell stress levels.

Design Approach & Concept

Design Objectives

The UniCell is based on the ESC design concept. The standard ESC design of SOFCs has adequately low levels of activation and concentration polarizations. However the ESC power density is plagued by ohmic polarization. The UniCell design conserves the benefits of the standard ESC while minimizing the ohmic polarization. An added benefit of the UniCell design is further reduction of the activation polarization by increasing the three phase boundary.

Minimize Area Specific Resistance: The ohmic polarization of the ESC design due to ionic resistance dominates the cell losses. The area specific resistance (ASR) correlates the thickness of the electrolyte (and in turn the path length of the oxygen ion) to the level of ohmic polarization present. To adequately reduce the ASR the ionic path length through the 8 mol% YSZ electrolyte must be less than or equal to 50 microns when operating at 800° C. See Figure 9 on page 21 for more details.

The extensive path length for an oxygen ion travelling through a relatively thick ESC electrolyte is minimized in the UniCell design by interleaving surface features.

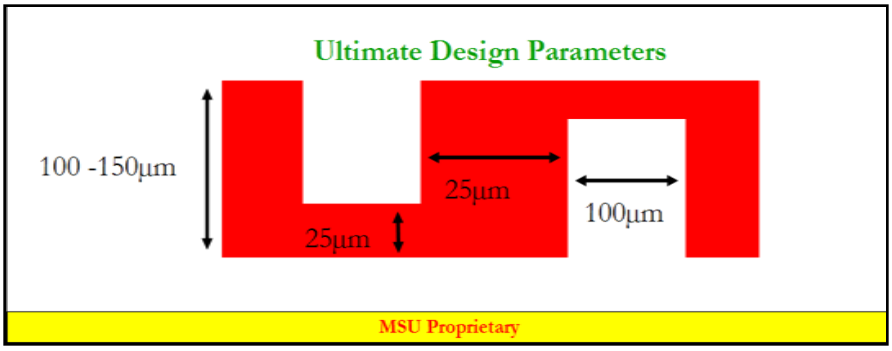


Figure 34 UniCell Ultimate Design Parameters Diagram

The ion will seek the path of least resistance through the electrolyte. The interleaved features permit the travel of the oxygen ion across the electrolyte through the interleaved feature walls and floors. The ultimate UniCell design reduces the path length of the oxygen ion in a 100-150 micron thick electrolyte to only 25 microns, however considerations of mechanical strength become substantial with such small cross sections.

Minimize Activation Polarization: The activation polarization of ESCs is controlled by the rate of electrochemical reaction between the hydrogen fuel and oxygen ions at the three phase boundary. The oxygen ions encounter the fuel at the anode/electrolyte three phase boundary interface and react catalytically, giving off water, heat, and electrons. Due to the high operating temperatures of SOFCs the activation losses are relatively low. However, the three phase boundary region within the solid oxide unit cell is increased in the UniCell design thus mitigating the affects of activation by means of increased active surface area. The walls of the interleaved surface feature walls are all additional surface areas not present in a flat electrolyte that enhance the catalytic activity and hence performance.

SOFCs also are capable of catalytically reforming fuels within the anode layer. There remains adequate surface area throughout the thin anode in an ESC to still promote this catalytic reforming and shift reaction.

Minimize Concentration Polarization: The ASC's thick anode support layer causes a high level of concentration polarization. The tortuous path through the anode limits the diffusion of fuel to the three phase boundary and water away from the electrolyte interface. The ESC and UniCell designs utilize thin electrodes (≤ 50 microns) to essentially negate concentration polarization.

Design Constraints

The UniCell must be capable of being manufactured utilizing commercial fabrication techniques that can be economically integrated into SOFC assembly lines under current standards. The surface contouring of the electrolyte support must not sacrifice the mechanical integrity of the unit cell to a level where failure is likely during fabrication or operation. All performance and design specifications must be in accordance with those established by the Solid State Energy Conversion Alliance (SECA).

Provide Adequate Mechanical Strength: The UniCell design must preserve adequate mechanical integrity to ensure the cell is capable of withstanding stress levels encountered in SOFC fabrication and normal operating environments relative to: (1) thermal expansion (2) fabrication handling (3) vibration forces and (4) impact shock.

Permit Feasible Fabrication: The fabrication of the UniCell prototype, to prove the effectiveness of the design concept, must utilize commercial manufacturing techniques. It is desired to adapt a set of standard manufacturing techniques to the UniCell production line in a cost effective method. However the prototype design does not need to optimize the process rather demonstrate feasibility of interleaving features into the electrolyte to improve electrochemical performance.

The surface contouring of the electrolyte cannot inhibit the application of continuous electrode layers. A feature with dimensions too small will prohibit the even dispersion of the electrode due to capillary forces and wall edge shadowing during electrode spraying.

SECA SOFC Design Specifications: All performance and design specifications must be in accordance with those established by the Solid State Energy Conversion Alliance (SECA). The unit cell must demonstrate a power density of 0.3 W/cm^2 with a total ASR less than 0.560 ohm-cm^2. The cell must demonstrate less than a 6% degradation rate per every 1,000 hours. At 0.7 operating volts the cell must be capable of utilizing at least 88% of the supplied fuel. The SOFC systems must be capable of being manufactured for $400/kW.

Design Alternatives

The UniCell design constraints and objectives permit the engineer to vary several diverse free variables: (1) electrolyte and electrode materials (2) cell geometry and architecture and (3) manufacturing methods. Two different design concepts were explored with several different subtypes: (1) interleaved hole patterns and (2) interleaved channel patterns. Materials were

selected based on industry standard choices that are compatible with the two designs in attempt to reduce the number of variables.

Interleaved Hole Pattern

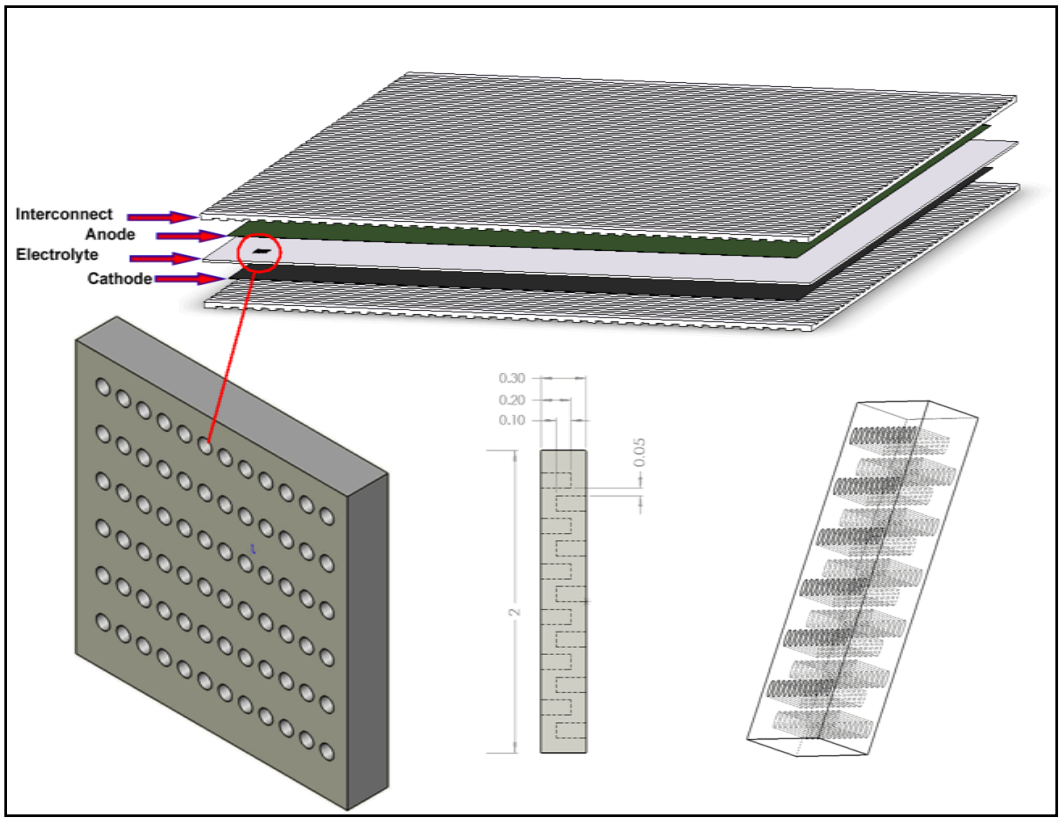


Figure 35 UniCell Linear Interleaved Hole CAD Model

The electrolyte was modified to include sets of blind micro-via hole patterns that were offset from one side to the other. The holes on the top side of the electrolyte interleave with the holes on the bottom side, reducing the overall ionic path length. Two different arrangements of holes were investigated: (1) interleaved holes arranged in a series of straight lines and (2) interleaved holes arranged in a checkerboard pattern.

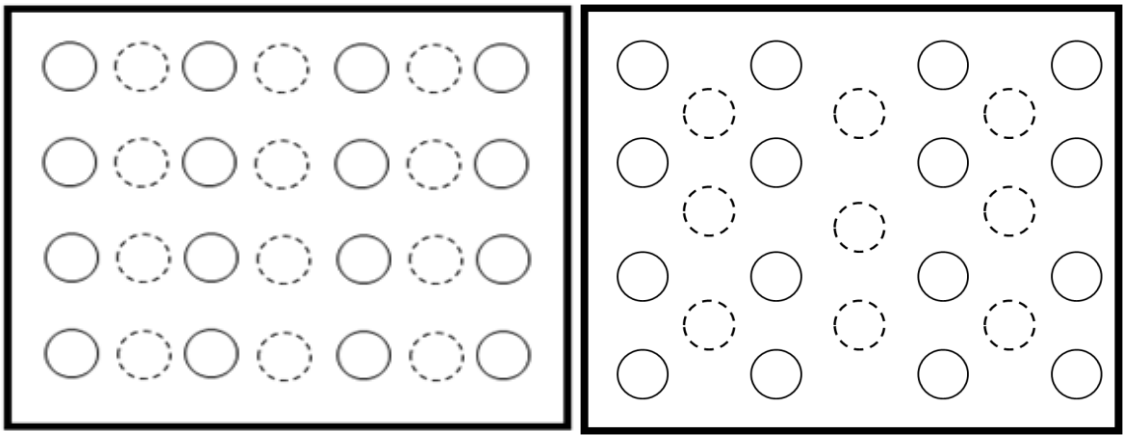


Figure 36 UniCell Interleaved Hole Patterns
(Left: Linear & Right: Checkerboard)

The shortest ionic path through the material is limited to traveling from one hole directly to an adjacent hole on the left or right. The checkerboard interweaving increases the number of ionic transport paths by providing four equal diffusion paths to the neighboring interleaved holes. The increase in three phase boundary area was calculated utilizing Solidworks and measured to approximately an increase of 77% based on 0.050 mm radius holes positioned 0.050 mm away from the nearest hole edge.

Interleaved Channels

To further improve the concentration of short ionic paths through the bulk material it was evident that replacing the hole patterns with interleaved channels would provide a continuous series of paths. Three different channel designs were drafted and evaluated for increase in surface area: (1) concentric channels (2) linear checkerboard channels and (3) radial checkerboard channels. Considerations relative to the effects of shrinkage during sintering, distribution of mechanical stresses, gas dispersion and the simplicity of machining were weighed.

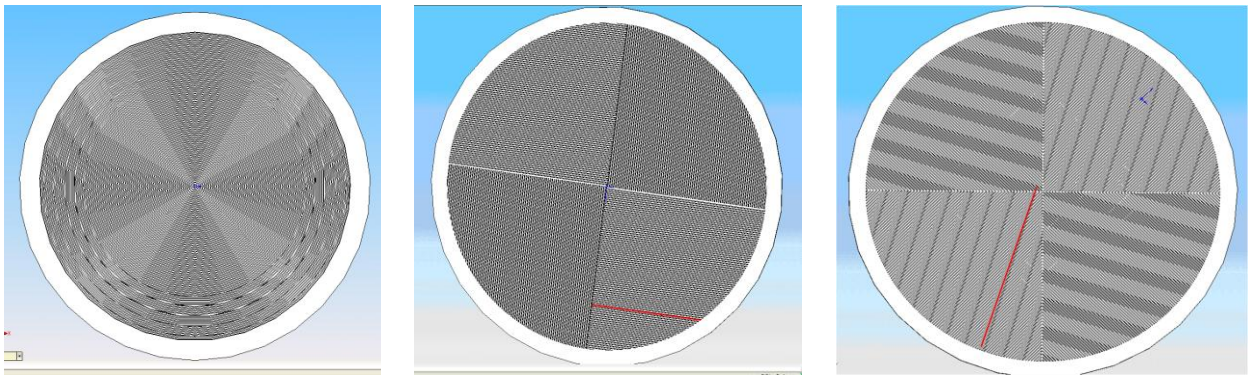


Figure 37 UniCell Channels Designs

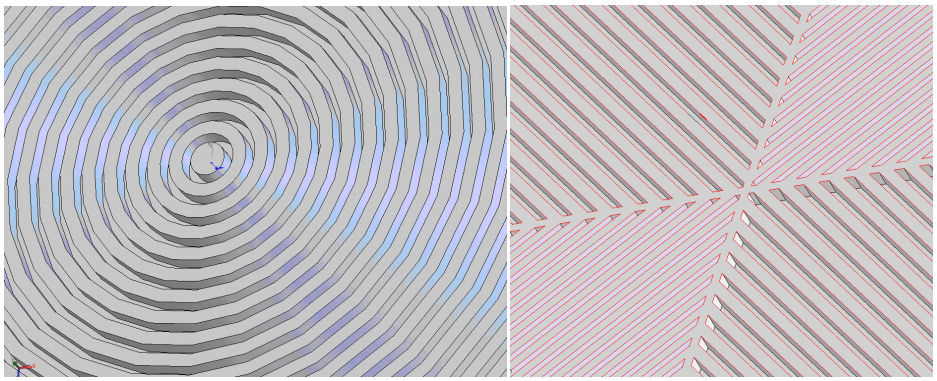


Figure 38 Channel Design Detail Views

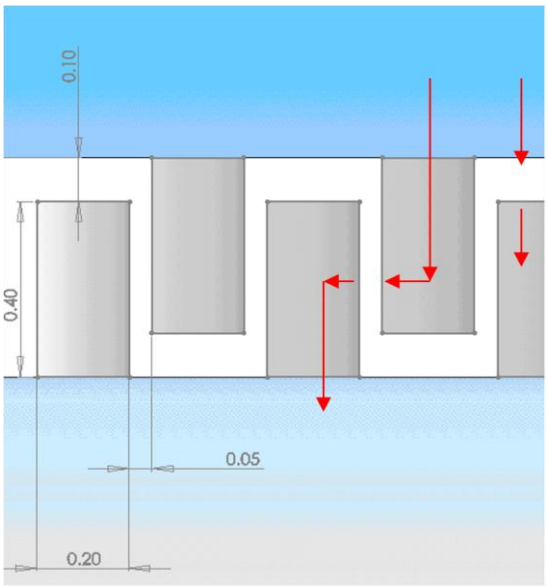


Figure 39 UniCell Channel Ionic Path Diagram

The concentric channel design offers an ionic diffusion path through the channels at all locations. Assuming the ionic path through the material is the shortest linear distance between two faces and channels occupy entire active area of cell, the interleaved channels reduce oxygen diffusion path length to approximately 0.070 mm through the electrolyte. To improve the overall strength of the material and accelerate the proof of concept study the interleaved channels were applied to a 0.400 mm thick electrolyte with the effort of scaling to follow in post studies.

$$t_{bot_channels} = 0.10 \text{ mm}$$

Equation 16 Ionic Path Distance through the Bottom of UniCell Channels

$$t_{wall} = 0.05 \text{ mm}$$

Equation 17 Ionic Path Distance through the Walls of UniCell Channels

$$A_{wall} = 0.30 \text{ mm}$$

Equation 18 Path Area of the UniCell Channel Wall per Unit Thickness

$$A_{floor} = 0.20 \text{ mm}$$

Equation 19 Path Area of UniCell Channel Floor per Unit Thickness

$$A_{total} = A_{wall} + A_{floor} = 0.50 \text{ mm}$$

Equation 20 Total UniCell Path Area per Unit Thickness

$$\text{Path} = t_{bot_channels} * A_{floor} / A_{total} + t_{wall} * A_{wall} / A_{total} = 0.70 \text{ mm}$$

Equation 21 Normalized Ionic Path Distance through UniCell Electrolyte

The interleaved channel designs reduce the difficulty of applying continuous and evenly distributed electrodes during air brushing by replacing holes, which are difficult to coat without filling, with larger channels. The interleaved channels may also act as an accordion to provide increased flexural strength.

Microscopic channel patterns increase the three phase boundary surface area from the interleaved holes, further decreasing the affect of activation polarization in lower temperatures

regimes. The surface area estimates assume it is appropriate to neglect the area on the perimeter of the cell where seals are applied because it is not chemically active. The surface area of the UniCell channel designs was calculated utilizing Solidworks software. The percent increase of surface area compares the UniCell electrolyte with an identical sized flat electrolyte without any surface contouring.

% Increase = 100% * (Electrolyte Area of Channel Design – Flat Electrolyte Area) / (Flat Electrolyte Area)

Equation 22 Percentage Surface Area Increase

The ratio of surface area, neglecting the seal area, is calculated utilizing Equation 23.

Surface Area Ratio = (Electrolyte Area of Channel Design) / (Flat Electrolyte Area)

Equation 23 Surface Area Ratio

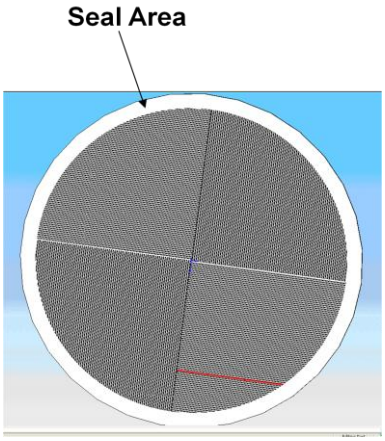


Figure 40 Seal Area Neglecting in Surface Area Calculations

Table 3 Channel Surface Area Comparison

Channel Design	Surface Area Increase	Surface Area Ratio
Concentric Channels	182%	2.82
Linear Checkerboard Channels	150 %	2.50
Radial Checkerboard Channels	148 %	2.48

The concentric channel design offers the highest increase in surface area, is simple and easiest to machine. The radial checkerboard channels may permit the gas flow from the center to the edges through the radial channels, where concerns could arise with the even gas dispersion in the concentric channel design.

EXPERIMENTAL PROCEDURE

Experimental Problem Definition

Design, fabrication, and testing of a novel electrolyte supported SOFC unit cell is essential to address the concerns defined in the needs statement. These objectives are defined as: Utilize standard ceramic processing techniques to fabricate a prototype; Optimize slurry mixture makeup and tape cast methodology to allow the consistent production of solid oxide fuel cell electrolytes; Study sintering behavior utilizing a dilatometer for linear shrinkage and CTE measurements and thermal gravitimetric analysis for burnout analysis and field emission microscope for imaging the microstructure; Investigate commercially available ceramic processing techniques for implementation of surface features; Conduct fuel cell performance testing on a tape cast, surface altered, electrode infiltrated and sintered unit cell utilizing a fuel cell test rig outputting voltage-current curves; and Determine if adequate mechanical integrity remains by calculating the brittle failure strength of the unit cell with Instron planar loading equipment.

Particle Dispersion Sedimentation Study

YSZ powder utilized for the particle dispersion was provided by Inframat Advanced Materials (Product # 40390R-8601). The fully stabilized 8 mol% cubic phase powder was manufactured by wet chemical co-precipitation method resulting in a 99.9+% purity (metal basis excluding Hf) with an average particle size of D_{50} ~0.5 mm and BET surface area approximately equal to 40 m^2/g. The powder has an approximate melting point of 2700 °C and a theoretical

density of 6.10 g/cm^3. [22] The solvent prepared was a 60/40 mixture of xylene/ethanol. Two different dispersants were tested: (1) blown menhaden fish oil (MFO) and (2) polyester/polyamide copolymer (KD-1).

The two dispersants were added in varying levels of 1-6 weight % of the YSZ powder to 12 separate xylene/ethanol solvent baths of 20 weight % solids loading. The dispersant and solvent mixtures were mixed utilizing an ultrasonic horn (Branson Sonifier 450 Horn Product Model # 102) for 60 seconds at a constant duty cycle of 4. The YSZ powder was added to each bath and mixed for another 60 seconds with the ultrasonic horn. The baths were then poured into 12 separate glass sedimentation vials and labeled. The vials were placed on a flat surface and left undisturbed for 72 hours other than monitoring optically with a digital camera.

Sintering Study

Effect of Maximum Sintering Temperature on Microstructure

Three separate sintering studies were conducted to study the effects of maximum sintering temperature on different ceramic powders and an electrolyte tape: (1) YSZ micro and nano particle sized powders (2) LSM Inframat and Nextech powders and (3) YSZ Tosoh powder electrolyte tapes. The fully stabilized 8 mol% cubic phase **micro** YSZ powder is identical to that utilized in the sedimentation study (Inframat Advanced Materials Product # 40390R-8601). The fully stabilized 8 mol% cubic phase **nano** YSZ powder (Inframat Advanced Materials Product # 40390N-8601) has a 99.9+% purity (metal basis excluding Hf) with an average particle size of 30-60 nm and BET multi-point specific surface area approximately equal to 15-40 m^2/g. The powders have the same approximate melting point and theoretical density. [23]

The LSM study utilized two powders from different manufacturers with varying microstructure morphology: (1) Inframat Advanced Materials (40 micron clusters) and (2) NexTech Materials (~0.5 micron particles in 100 micron clusters). The Inframat Advanced Materials LSM (Product # Infrox^{TM} S5725SR-1) is a perovskite with spherical granule morphology to permit flow during a spray feed. The average granule size is approximately 40 microns. The NexTech Materials LSM powder (Product # 41-01), $(La_{0.80}Sr_{0.20})0.98MnO_{3-\delta}$, is a single phase perovskite with an average particle size of approximately 0.5 microns, conglomerated in 100 micron clusters with a surface area 4-8 m^2/gram, CTE of 10-11 ppm/°C and an electrical conductivity greater than 200 S/cm at 800 °C. [24]

The YSZ Tosoh powder electrolyte tapes were cast at MSU. The 8 mol% YSZ Tosoh powder consists of 510 angstrom crystallite particles combined in spherical granules with a specific surface area of 6.5 m^2/g. The MFO dispersant (2.26 grams) was dissolved into a 60/40 Xylene/Ethanol solvent bath (66.67 grams). The Tosoh powder (100 grams) was added to the solvent/dispersant mixture in a 250 mL HDPE milling bottle with 250 grams of 10 mm diameter YSZ milling media pellets and ball milled for 24 hours at a speed setting of 4. The Polyvinyl Butyral B-98 Binder (7.75 grams), Butyl Benzyl Phthalate S-160 Type I Plasticizer (5.00 grams) and Polyalkylene Glycol Type II Plasticizer (4.00 grams) were added and ball milled for an additional 72 hours. The tapes were cast through a 8 inch wide doctor blade set at 425 microns and 900 microns on a Richard E. Mistler TTC-1200 table top casting machine set at a cast speed of 40.

The YSZ powders and LSM binder composites were pressed into ½ inch diameter pellets with an aspect ratio (height / diameter) less than 1 on a uniaxial press. The LSM powder

required the addition of a binder to increase the green strength of the pellet to permit handling. The binder (Polyvinyl alcohol celvol 21205) was combined with de-ionized water in 4:1 water to binder ratio. The binder solvent was then added to the LSM powder at 5% solids loading and hand mixed. To ensure laminate levels did not form the pressure was applied steadily up to 350 MPa for the YSZ powders and 175 MPa for the LSM. The pressure was held constant for 1 minute and then slowly released to avoid fracturing from the rapid discharge of the stored elastic energy. The YSZ tape was cut into 12.75 mm diameter disks with a die punch. The hand die punch cut a precise circle by pushing the punch completely through the green body and making a ¼ turn with the punch. The small size limited the shrinkage warping to avoid affecting the post sintered geometric density values.

The pressed pellets were placed in an aluminum oxide crucible without a constricting load on top. Ten of the punched tape discs were placed with the mylar contact side on the bottom between two 0.635 mm thick, 10 cm square sheets of aluminum refractory boards from Zircar ceramic (Type RS). The sintering cycles all utilized a 5 °C/min ramp rate to the maximum temperature where it dwelled for 2 hours prior to be cooled at 10 °C/min to ambient temperature. The YSZ micro powder pellets were sintered at maximum temperatures from 1100 – 1550 °C in increments of 50 °C. The YSZ nano powder pellets were sintered at maximum temperatures from 1100 – 1400 °C in increments of 50 °C. The LSM pellets were all sintered to maximum temperatures from 1100 – 1400 °C in increments of 50 °C. The YSZ electrolyte tape discs were sintered at maximum temperatures from 1400 – 1550 °C in increments of 50 °C. The electrolyte disc samples were sintered under an equal pressure distribution of 165 N/m^2 (in

accordance to the parameters described on page 87). A silicon carbide high temperature box furnace (Applied Test Systems, Inc. – Model Kanthal Super 33 PC-120/240-60) was utilized.

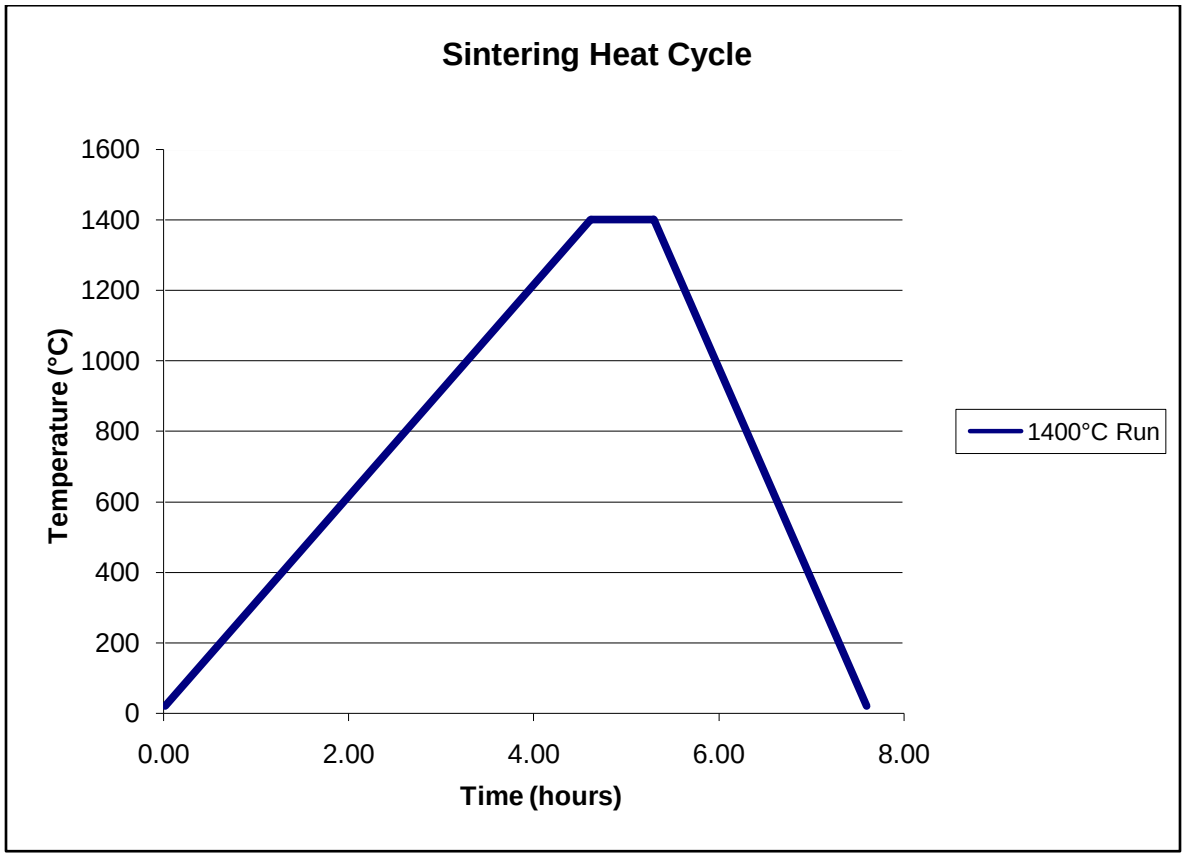


Figure 41 Sintering Cycle Temperature Profile (1400 °C)

The green density of the samples was calculated using two methods: (1) geometric measurements and the (2) Archimedes submersion technique. For the geometric measurements the weight of the sample was measured on a balance, and the height and diameter of the samples were measured with a digital caliper.

$$\text{Density} = \text{mass} / (\pi * r^2 * h)$$

Equation 24 Geometric Density

The relative sintered density equation compares the theoretical packing density of the materials to the measured density.

Relative Density = Measured density / theoretical packing density

Equation 25 Relative Density

The Archimedes density measurements were calculated and used as a comparison of the geometric densities measured. Archimedes' principle states that a body immersed in a fluid is buoyed up by a force equal to the weight of the displaced fluid. Since 1 mL of water has a mass almost exactly equal to 1g, if the object is immersed in water, the difference between the two masses will equal almost exactly the volume of the object weighed. The assumed density of water utilized for calculations was 0.998203 g/cm^3. A C shaped metal sample holder was set on the scale and hung the sample into a cup of water. The wet weight of the sample suspended in water was measured. The volume of water that was displaced by the sample was calculated using Equation 26.

Volume displaced = (wet weight - dry weight)/(density of water)

Equation 26 Achimedes Volume

The Archimedes density was then calculated using Equation 27.

Archimedes density = (Dry weight)/(volume displaced)

Equation 27 Achimedes Density

Field emission microscopy (FEM) was utilized to collect images of the microstructures at magnifications of 5,000 and 10,000. The YSZ uniaxially pressed and tape cast samples were sputter coated with Iridium at 20 mA for 30 seconds to enable electron mapping of the surface since YSZ is not electrically conductive. The Linear Intercept Method used to estimate grain size required drawing a line diagonally across a FEM image of the grains. (See Figure 42) The average grain size was calculated as the number of grains intercepted by the line divided by the line length.

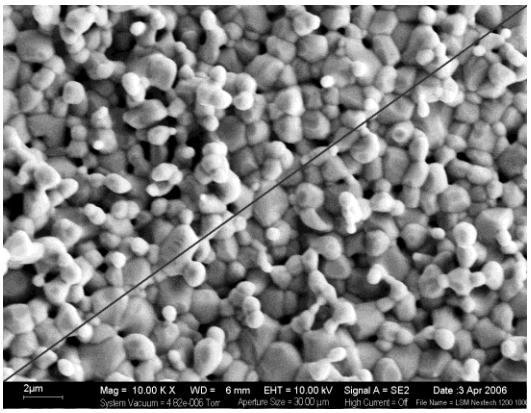


Figure 42 Linear Intercept Method

Sintering Pressure

A constant pressure must be applied to the YSZ electrolyte tape during sintering to ensure minimal cell curvature. However excessive pressure can constrict the sample, prohibiting even shrinkage during sintering and resulting in high stress concentrations that cause internal flaws to form in the YSZ microstructure. These flaws in the electrolyte discs act as regions from which cracks could form and propagate prior to reaching the maximum flexural strength.

The electrolyte tapes were sintered between two aluminum oxide refractory boards with varying amounts of additional weight on top. It was determined empirically that an acceptable pressure to be applied by the top sheet was 165 N/m^2. The following sintering pressure regime was applied during sintering of the concentric ring and fuel cell samples. Five 77 mm diameter electrolyte discs were placed on top of a 0.635 cm thick, 25.5 by 27 cm rectangular aluminum oxide board (Zircar Zirconia © TYPE Buster) with the mylar contact side facing down. A 0.20 cm thick sheet (360 grams) was placed on top with a 15 mm diameter zirconia milling media pellet (15.5 grams) on the top directly above each disc for additional weight. The top and bottom

aluminum oxide boards required careful inspection for imperfections to avoid having the sample snagged slightly.

Tape Cast Optimization Studies

Starting Materials

YSZ raw powders produced by two different manufacturers were utilized for tape casting: (1) Inframat Advanced Materials and (2) Tosoh Corporation. The Inframat fully stabilized 8 mol% cubic phase micro YSZ powder is identical to that utilized in the sedimentation and sintering studies (Inframat Advanced Materials Product # 40390R-8601). The Tosoh YSZ powder is the same powder utilized for the YSZ tape in the sintering study.

Table 4 Electrolyte Tape Concentrations

Constituents	Solids Loading %
YSZ	
Inframat Powder	58.6 %
Tosoh Powder	58.6 – 60.0 %
Xylene/Ethanol Solvent 60/40	Not Applicable
Constituents	**Weight % of YSZ**
Dispersant	
Blown Menhaden Fish Oil (MFO)	2.26
Polyester/Polyamide Copolymer (KD-1)	2.26
Butyl Benzyl Phthalate S-160 Type I Plasticizer	5.0 – 6.0
Polyalkylene Glycol Type II Plasticizer	4.0 – 5.0
Polyvinyl Butyral B-98 Binder	7.75 – 8.0

The two different dispersant agents studied in the sedimentation study were also investigated for tape casting at 2.26 % solids loading: (1) blown menhaden fish oil (MFO) and (2) polyester/polyamide copolymer (KD-1). The types of solvent (60/40 Xylene/Ethanol), plasticizers (Butyl Benzyl Phthalate S-160 Type I Plasticizer and Polyalkylene Glycol Type II

Plasticizer) and binder (Polyvinyl Butyral B-98 Binder) remained consistent throughout all tape cast experiments; however the concentrations were altered to optimize the tape.

Slurry Preparation

The solvent was poured into a 250 mL HDPE bottle and then the dispersant was added. The bottle was closed tightly and rigorously shaken by hand for 15 seconds. The YSZ powder and ball milling media was added and again hand shaken. The container was then placed on a ball rolling mill for 12-72 hours. At the end of the first milling period the bottle was removed from the milling rollers, the binders and plasticizers were added, hand shaken and returned to the rollers. The second milling period ranged from 6-72 hours. At the end of the second milling period the slurry was filtered and then de-aired in a vacuum for one minute.

Tape Casting

The tapes were cast through two different doctor blades: (1) 8 inch wide single doctor blade (2) 8 inch double doctor blade. The doctor blade height ranged from 0.400 to 1.000 mm on a Richard E. Mistler TTC-1200 table top casting machine set at a constant cast speed setting of 40%. When pouring the slurry into the doctor blade the height of the fluid in the doctor blade was attempted to be held consistent by the eye, it was not automatically controlled or monitored. The hydrostatic pressure was held more consistent with the double doctor blades, applying a more constant shearing stress to the slurry as the moving Mylar sheet pulled it into a thin tape. The tapes were all air dried on the tape cast bed at ambient temperature without air circulation. A sheet of plexiglass acted as a lid covering the tape casting bed; however the seal was not air tight

and large openings at the front and rear of the tape cast bed permitted air flow necessary for drying.

Thermal Gravimetric Burnout Study

Thermal gravimetric analysis was conducted on a Linseis L81 vertical bench top research balance. The Balance was controlled through the Linseis design PCI controller / data acquisition card. The software used was a Linseis 32 Bit Windows package with data acquisition and evaluation tools. A 3 mL aluminum oxide crucible was used as the sample holder. A baseline reference curve was first obtained for each temperature profile tested by placing an equal amount of aluminum oxide powder in the reference and sample crucibles. The sample crucible was then loosely filled halfway with a green tape (See Table 5) sliced into ½ cm squares, weighed on a balance and placed in the TGA.

The TGA study varied the temperature profiles' ramp rates, dwell temperatures and dwell periods. The tests were all conducted in an air oxidizing atmosphere chamber vented to atmosphere pressure and brought up to a maximum temperature of 1500 °C. The data collection software recorded the precise weight of the sample every 10 seconds as a function of furnace temperature. The Linseis data analysis software was utilized to subtract out the effect of the reference material on the balance as measured in the baseline curve.

Table 5 Tape Recipe Used for TGA Study

Constituents	Solids Loading %
8 mol% YSZ Tosoh Powder	60.0%
Xylene/Ethanol Solvent 60/40	Not Applicable
Constituents	**Weight % of YSZ**
Blown Menhaden Fish Oil (MFO)Dispersant	2.26
Butyl Benzyl Phthalate S-160 Type I Plasticizer	5.0
Polyalkylene Glycol Type II Plasticizer	4.0
Polyvinyl Butyral B-98 Binder	7.75

Dilatometer Studies

A dilatometer study was conducted to investigate linear shrinkage of uniaxially pressed YSZ pellets with varying powder morphologies as a function of sintering cycles. A second dilatometer study investigated the CTE of a sintered YSZ electrolyte sheet at 800 °C. The 8 mol% YSZ micro and nano particle sized powders (Inframat Advanced Materials Product #s 40390R-8601 & 40390N-8601 respectively) were pressed into 1.27 cm diameter pellets at 350 MPa with an aspect ratio less than 1. A vertical bench top Linseis L75 dilatometer was utilized. The dilatometer's linear actuator measured the change in sample thickness. An aluminum oxide sample key, sample holder and pushrod was used for all tests. A baseline reference curve was first obtained for each temperature profile tested by running the system without a sample to measure the thermal expansion of system components. The sample's thickness was measured with a digital caliper and recorded. The sample was then placed freely on top of the sample holder in the dilatometer. The preload was set at 300 mN and the sample was run in air without additional gas flows.

Surface Contouring Investigation

The following table summarizes the various methods explored to obtained different surface contouring designs.

Table 6 Surface Contour Methods Explored

Machining Method	Sample State	Sample Thickness
Interleaved Linear Hole Pattern		
CO_2 Laser	Green & Sintered	150 microns
Interleaved Checkerboard Hole Pattern		
Photoresist Machining	Green & Sintered	150 microns
CO_2 Laser	Green	150 microns
Interleaved Concentric Channels		
Excimer Laser	Green	400 microns
Photoresist Machining	Green	400 microns
One Side Linear Channels		
CO_2 Laser	Green	400 microns

An application test was conducted to determine whether CO_2 laser drilling could be used to obtain the linear interleaved pattern of microvia holes with the desired hole diameter, blind depth and profile in green and sintered YSZ thin films. For original testing the total hole count, disc's shape and location of the holes relative to the disc's edge were not of concern. The 100 micron diameter blind holes were attempted to be drilled to a depth of 100 microns in a 150 micron thick green tape and a sintered disc. The green laser drilled sample was sintered under atmospheric pressure (5 °C/min to 1500 °C, dwell for 2 hours and cool to ambient at 10 °C/min). The samples were then sliced through the center of the holes, mounted in epoxy and polished flat for optical viewing.

The checkerboard interleaved hole pattern was attempted to be manufactured via two methods: (1) CO_2 laser drilling on a 150 micron thick green sample and (2) photoresist

machining on 150 micron thick sintered and green samples. Photoresist machining was also investigated for manufacturing concentric channels in a green YSZ tape.

Excimer laser drilling was investigated to produce the concentric channel design in a 400 micron thick electrolyte green tape. To reduce processing time a wide aperture CO_2 laser was tested for machining linear channels into one side of a 400 micron green tape. These samples were sintered for 24 hours under an equal pressure distribution of 165 N/m^2 (in accordance to the parameters described on page 87).

An optical microscope was utilized to obtain images of the concentric channel UniCell in three states: (1) green (2) sintered prior to application of the electrodes and (3) as a complete unit cell including the electrodes. FEM was used to obtain high definition images of three sample sets: (1) green and sintered CO_2 laser drilled linear hole pattern samples (2) sintered concentric channel UniCell and (3) sintered CO_2 laser drilled linear channel specimen. All samples were sputter coated with Iridium for 30 seconds at 20 mA prior to enable imaging in the FEM.

Mechanical Strength Study

Equibiaxial flexural strength tests of a commercial 3 mol % YSZ electrolyte tape (Electro-Science Laboratories Product # 42000) and several different 8 mol % MSU fabricated electrolyte tapes were conducted at ambient temperature in accordance with the ASTM standard test method C 1499-05[25]. To comply with the test requirements, the samples tested must be a monolithic ceramic that is macroscopically isotropic.

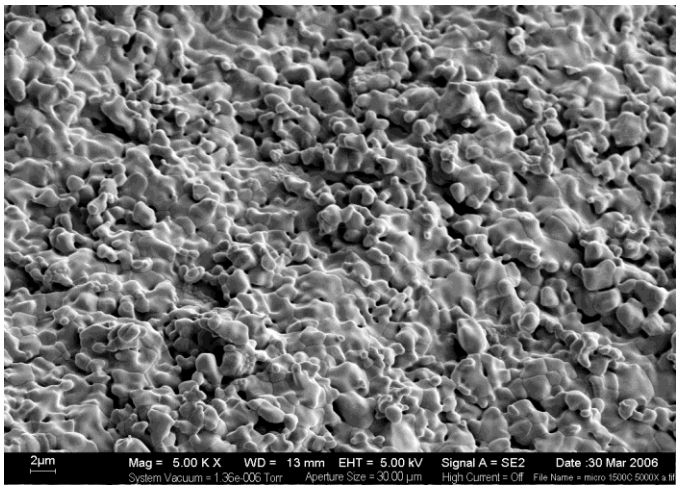


Figure 43 FEM Image of Electrolyte Displays a Macroscopically Isotropic Material after Sintering

ESL 3 mol % YSZ Samples

The Electro-Science Laboratories (ESL) partially stabilized 3 mol % YSZ tape was purchased from H-Tech Inc. Samples were stamped out of the tape utilizing a 10.16 cm diameter aluminum punch. The ESL recommended 5 stage sintering process used to fire the green tape to the approximately 98% of theoretical density was: (1) 3°C per minute to 600°C (2) 10°C per minute to 1000°C (3) 5°C per minute to 1450°C (4) 30 minute dwell at 1450°C (5) 10°C per minute to ambient. Sets of five samples were batch sintered between two sheets of aluminum oxide weighted with YSZ milling media pellets to apply a set pressure as described on page 87.

MSU YSZ Samples

The different MSU tape batches utilized for the concentric ring strengths tests included tape numbers 17, 21, 22, 24DB and 25. The recipe and processing parameters for all of these tapes remains consistent with the tape recipe used for the TGA study shown in Table 5 on page

91. However the slurries were ball milled for different periods and the tapes were cast at different doctor blade settings. Table 7 shows the different tape manufacturing parameters.

Table 7 MSU Concentric Ring Samples

MSU Tape #	Second Stage Milling Period Duration (hours)	Doctor Blade Height (mm)	Sample Batch Size Tested
17	72	425	1
21	24	470	4
22	72	1065	2
24DB	72	1250	5
25	72	400	10

The electrolyte discs were removed from the green tape via a new, sharp and clean razor blade hand guided by the edge of a template placed on top of the green body. The samples were all sintered in the following 6 stage 24 hour cycle: (1) 2°C per minute to 150°C (2) 2 hour dwell at 150°C (3) 0.5°C per minute to 400°C (4) 2.5°C per minute to 1500°C (5) 2 hour dwell at 1500°C (6) 10°C per minute to ambient. The samples were sintered in between the aluminum oxide sheets identical to the ESL samples. The MSU discs tested covered a broad range of thicknesses (0.11 – 0.52 mm). The diameters of the samples only varied slightly (76.19 – 77.9 mm) after sintering.

Concentric Ring Sample Holder

A concentric ring on ring apparatus, in accordance with ASTM C1499-05 test standards was designed, manufactured and mounted onto a table Instron accurate within ±1% of the selected load range. Refer to Appendix A on page 156 for detailed shop drawings of the fixture.

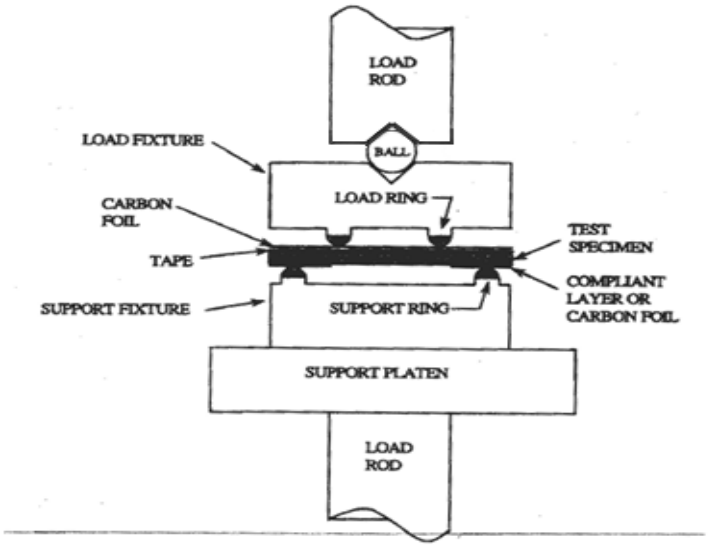


Figure 44 Section View of Basic Fixturing and Test Specimen for Equibiaxial Testing [25]

An aluminum 6061 T-6 load rod, with a 0.3175 cm diameter conical indentation 0.3175 cm deep, was mounted inside the top Instron support and held in place with a cotter pin. The aluminum 6061-T6 bottom load rod and bottom platen was mounted inside the lower Instron support and held in place with a cotter pin. A 316 stainless steel support fixture with a support ring, pressure relief center hole and channel (see Appendix A on page 156) was placed on top of the bottom platen. A circular recess at the center of the bottom platen fit into the support fixture's center hole to ensure the fixture was consistently aligned in the same keyed location. The thin electrolyte disc was concentrically placed freely on top of the bottom ring. The top ring plate was set on top of the electrolyte disc parallel to the bottom plate by visual inspection. On the upper side of the top load fixture was a conical indentation in which a 0.3175 cm steel ball bearing was placed in order to ensure an even distribution of the load.

Test Procedure

The pretest sample thickness was measured with a digital caliper with a resolution of 0.01 mm at the center and four equally spaced positions and then averaged. The diameters of the samples were measured with a digital caliper at two radial positions nominally separated by 90° and averaged. The samples were visually inspected for any flaws or cracks to eliminate faulty specimens. The top and bottom rings were aligned concentrically by positioning the load fixtures in their keyed locations. Prior to placing the sample on top of the bottom fixture both load rings were inspected for nicks. The sample was then placed on the bottom load ring. The top load ring was placed on top of the electrolyte sample and aligned with the top load rod.

The concentric ring-on-ring apparatus equally distributed the force across the ring to accurately measure the maximum brittle failure strength of ceramic SOFC components under monotonic loading. The sample was first preloaded to ~10% of the failure load. The data acquisition software was started and a constant linearly increasing dynamic compression load with a ramp rate of 2 mm/min was applied in uniaxial fashion to the sample. The Instron data acquisition system software (BlueHill) recorded displacements over time as a function of load. Upon failure, the top load rod was retracted and the sample was carefully removed, placed on a piece of paper and reconstructed. The type of failure was recorded for each in accordance with ASTM test method C 1499-05. (See Figure 45) The samples with edge initiated failure were regarded as invalid and not included in the reported results.

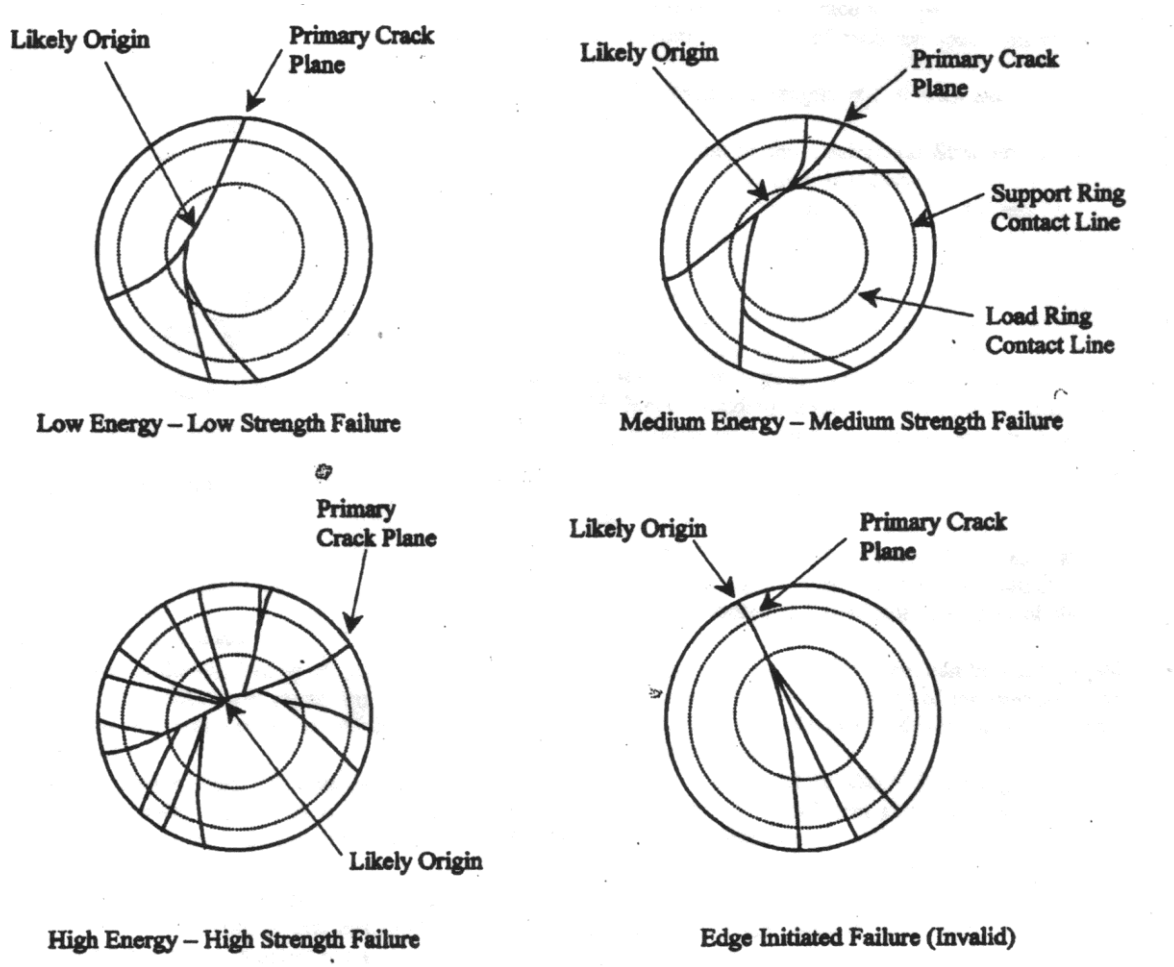


Figure 45 Illustrations of Failure Patterns in Concentric Ring Test Specimens [25]

Calculation of Results

The equibiaxial strength (σ_f) is a function of the linear force applied (F), sample height (h), sample diameter (D), Poisson's ratio (υ), support ring diameter (D_s), and load ring diameter (D_L). The equibiaxial strength is measured in MPa, force is measured in newtons, Poisson's ratio is dimensionless and the remaining dimensions are measured in mm. The formula for equibiaxial strength at point of failure for the circular disc tested in the concentric ring apparatus is:

$$\sigma_f = \frac{3F}{2\pi h^2} * [(1-\upsilon) * \frac{{D_s}^2 - {D_L}^2}{2D^2} + (1+\upsilon)\ln\left(\frac{Ds}{D_L}\right)]$$

Equation 28 Equibiaxial Strength of a Circular Plate in a Concentric Ring Load Test [25]

Fuel Cell Performance Study

Sample Punching

The electrolyte discs were removed from the green tape via two different tools: (1) razor blade and (2) laser. The UniCell laser drilled sample was removed from the green tape during surface contouring.

Sintering

The samples were placed on an aluminum oxide refractory sheet with a second sheet and YSZ milling media weights set on top as necessary to obtain approximately an equal pressure distribution of 165 N/m^2, in accordance with the parameters set on page 87. They were then heat treated in the furnace at the optimized 24 sintering cycle described on page 87.

Electrode Application

Ni-YSZ anode and LSM cathode inks were prepared and applied to the electrolyte samples via air brushing to permit the fuel cell electrochemical testing. The inks were ball milled in 250 mL HDPE bottles on a standard two roll mill in two stages for 24 hours each. To prepare the cathode ink the first step was to combine 45g LSMO (Inframat Advanced Materials Product #: Infrox TM 5725-1 lot# IAM5045LSM1) with 20 grams of de-ionized water and 0.25 grams of a Darvan C dispersant solution (ammonium polymethacrylate 30875-88-8 and water 7732-18-5). The anode ink prepared for the first milling stage combined 29.25 g NiO powder purchased from NexTech Materials, 15.75 grams of Tosoh YSZ powder, 20 grams of de-ionized

water and 8 drops of the Darvan C dispersant. The containers were filled 1/3 with equal parts of 5 and 10 mm milling media and mixed, at a speed setting of 4, for 24 hours. The containers were removed from the rolling pins to add 5 grams of polyvinyl alcohol solution (celvol 21205 binder) and 3 drops of surfynol 485 surfactant. The containers were then returned to the rolling pins and milled for the second 24 hour period.

A template was machined out of aluminum to permit airbrushing electrodes with a consistent shape and clean edges. The cells were placed within the template holder while the electrodes were airbrushed one by one onto the electrolyte via an internal mix airbrush apparatus. The airbrush gun reservoir was filled with an equal amount of ink each time, held 18 inches from the sample and moved side to side to evenly distribute the ink onto the electrolyte. The samples were removed from the template holders and placed in a dish, with the cathode facing down, where only the uncoated edges were in contact with the dish. The samples were air dried for 30 minutes and then placed on top of an aluminum oxide sheet with the cathode facing down. The cells were co-sintered from ambient to 1300 °C at 5 °C/min, held for two hours and cooled to ambient at 10 °C/min to produce a porous structure chemically bonded to the electrolyte substrate.

Fuel Cell Test Stand

The MSU fuel cell test system consists of a vertical tube furnace (Applied Test Systems Inc Product # 3210, 1500 W, 115 VAC, 13 A), compressed hydrogen (UN1049), nitrogen (UN1066) and air (UN1002) gas cylinders, pressure regulators (Product #s N_2: HP722-125-580-BE, H2: HP722-125-350-BE and Air: GPS270-40-346-4M), 1,000 SCCM mass flow controllers (MKS Product #s N_2: 1179A01313CS1BV, H2: 117900713CS1BV and Air:

1179A00813CS1BV), multi gas controller (MKS Product # 647C), system DC power supply (Agilent 0-10V, 0-50A, Product # 6651A JO1), system DC electronic load (Agilent Product # N3301A), tygon tubing and a dell desktop with LabView Software (Version 8.0). The system permits independent control of N_2, H_2 and air flows, temperature and voltage or current.

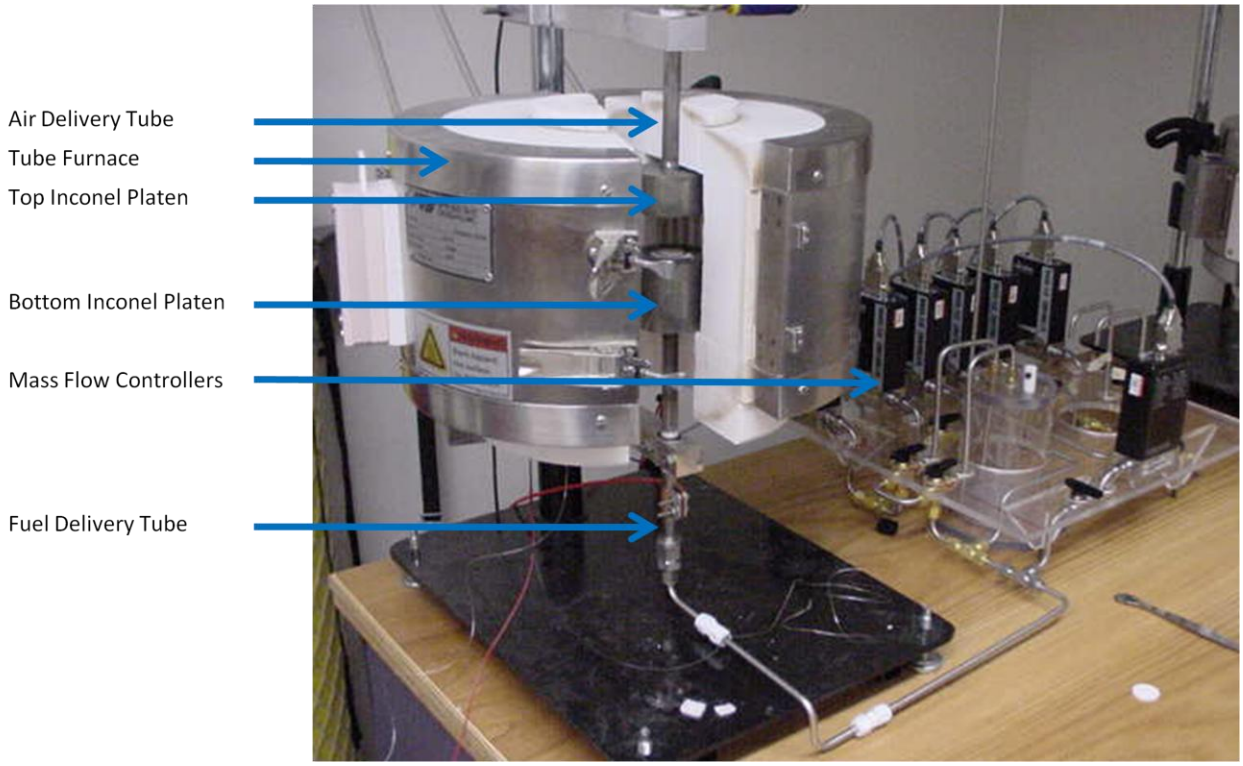


Figure 46 Fuel Cell Test Rig Furnace and Mass Flow Controllers

Solid Oxide Unit Cell Mounting

The fuel cells were mounted between two Inconel platens within the fuel cell test rig (See Figure 47). Silver mesh and nickel foam were cut into circles with the same size diameter as the electrodes. The silver mesh was pressed between two flat steel plates with a uniaxial press to 7,000 psi to flatten the material and ensure good contact is made with the cathode. The nickel mess was reduced to 2/3 of its original thickness in the uniaxial press at very low pressure to

ensure gas diffusion through the foam was not limited. A thin layer of silver paste was applied with a razor blade to the Inconel platens, silver mesh and nickel foam. Careful attention was paid to ensure the silver did not protrude past the electrodes and short out the cell. The nickel foam was placed on the bottom where the anode is exposed to flowing hydrogen and nitrogen. The solid oxide unit cell was placed on top of the nickel foam with the anode side facing down. The silver mesh was placed on the top of the electrolyte and the top Inconel platen was lowered on top of the entire sandwich, contacting the silver mesh.



Figure 47 Fuel Cell Test Rig Inconel Platens

Operating Conditions

All fuel cell tests were conducted under identical operating parameters. The furnace temperature profiles, gas flow rates and operating voltage conditions are shown in Table 8 & Table 9. The cells were brought up to temperature under constant nitrogen and air flows of 20 mL/min. Once the furnace temperature neared 750 °C the nitrogen and compressed air flows were raised to 170 and 250 mL/min respectively, and the hydrogen flow was stepped up continuously over 30 minutes to 130 mL/min. Voltage-current (V-I) and constant 0.5 V curves were obtained at 750, 800 and 850 °C.

Table 8 Fuel Cell Testing Temperature Profile

Sintering Cycle							
Temp	Ramp Rate (°C/min)	Duration (min)	Duration (s)	Starting Time	Starting Time (s)	Ending Time (min)	Ending Time (s)
0-750	2.5	290	17400	0	0	290	17400
750	Dwell	310	18600	290	17400	600	36000
750-800	2.5	20	1200	600	36000	620	37200
800	Dwell	300	18000	620	37200	920	55200
800-850	2.5	20	1200	920	55200	940	56400
850	Dwell	300	18000	940	56400	1240	74400
850-ambient	10	85	5100	1240	74400	1325	79500

Table 9 Fuel Cell Testing Operating Conditions

Fuel Cell Testing Regime							
Stage #	Duration (s)	Ending Time (s)	Temp	Nitrogen Flow (mL/min)	H2 Flow (mL/min)	Air Flow (mL/min)	Voltage ***
1	16200	16200	0-750	20	0	20	0.5
2	1800	18000	750	170	0+130/1800*(t-16200)	250	0.5
3	3600	21600	750	170	130	250	0.5
4	3600	25200	750	170	130	250	1.2-1.0/3600*(t-21600)
5	3600	28800	750	170	130	250	0.5
6	3600	32400	750	170	130	250	1.2-1.0/3600*(t-28800)
7	3600	36000	750	170	130	250	0.5
8	1200	37200	750-800	170	130	250	0.5
9	3600	40800	800	170	130	250	0.5
10	3600	44400	800	170	130	250	1.2-1.0/3600*(t-40800)
11	3600	48000	800	170	130	250	0.5
12	3600	51600	800	170	130	250	1.2-1.0/3600*(t-48000)
13	3600	55200	800	170	130	250	0.5
14	1200	56400	800-850	170	130	250	0.5
15	3600	60000	850	170	130	250	0.5
16	3600	63600	850	170	130	250	1.2-1.0/3600*(t-60000)
17	3600	67200	850	170	130	250	0.5
18	3600	70800	850	170	130	250	1.2-1.0/3600*(t-67200)
19	3600	74400	850	170	130	250	0.5
20	4950	79350	850-25	20	0	20	0.5
21	END	END	25	0	0	0	0

A set of four different fuel cells were tested: (1) 100 micron thick MSU fabricated ESC (2) 400 micron thick MSU fabricated ESC (3) 125 micron thick Indec commercial ESC and (4) 400 micron thick UniCell.

RESULTS & DISCUSSION

Particle Dispersion Sedimentation Study

Subsequent to ultrasonic mixing a homogeneous solution of YSZ, xylene/ethanol and MFO dispersant was visually apparent. However after 18 hours the solution had already undergone significant settling. The 1% YSZ was fully settled, the 2% sample had half the volume of sedimentation at the bottom compared to the 1 %, and the 3-6% samples all had the same amount of sedimentation. The cloudy supernatant in the 2-6% samples indicates the dispersant is effective when fully coated with dispersant in which very fine YSZ particles remained separated and suspended from Brownian motion. Since these samples were ultrasonically mixed utilizing identical procedures it can be concluded that the mixing time was not adequate to fully break the VDW bonds between the ceramic particles and permit the long chain fatty acids in the MFO dispersant to coat the surface of all the YSZ. The YSZ agglomerates that remained in tack without dispersant chains extended into the solution were free to move, collide with other agglomerates and grow in size due to the VDW forces until the buoyancy force was exceeded by gravity causing the agglomerates to fall to the bottom. The 3-6% samples contained a solution where all the free YSZ particles were covered by dispersant chains and an equal amount of agglomerates settled at the bottom. Based on the final sedimentation heights it can be concluded that the optimum MFO dispersant weight percent of YSZ lies between 2-3%.

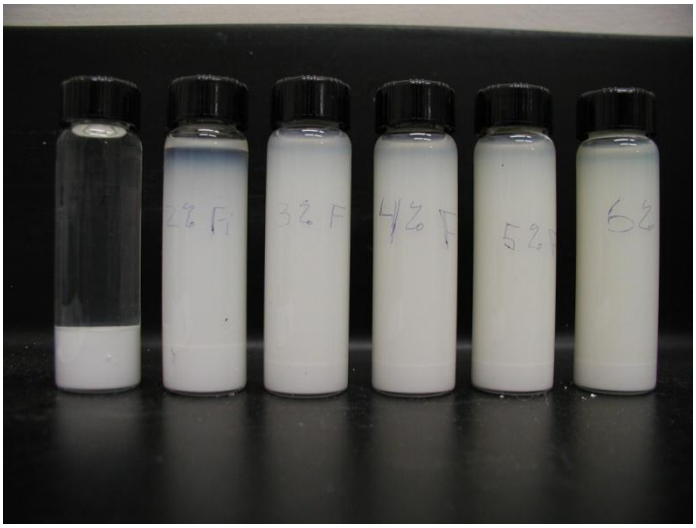


Figure 48 MFO Particle Dispersion Specimens After 66 hours

After 18 hours the 2-6% samples were only slightly transparent (see Figure 49). The 21 hour sample was more translucent than the 18 hour sample, but the 21, 42, 48 and 66 hour samples showed no difference in transparency or sedimentation levels. Therefore the sedimentation cycle is complete after approximately 21 hours.



Figure 49 MFO Particle Dispersion Specimens After 18 (left) & 24 (right) Hours

The KD-1 dispersed the YSZ in the solvent through ionic charging of the ceramic particle surfaces. Desorption of the KD-1 ions resulted in an ionic repulsion force that is stronger than

the VDW forces, stimulating dispersion. The 1% KD-1 vial had slightly more sedimentation at the bottom than the 2-6% vials, all of which had an identical sediment height; therefore approximately 1-2% KD-1 dispersant level is adequate.

The sediment heights in the 2-6% KD-1 vials were identical to that experienced in the 3-6% MFO vials. The sedimentation of the YSZ was slightly evident after 21 hours, however after 24 hours the YSZ particles began to settle. The 42, 48 and 66 hour samples have equal amounts of sediment at the bottom and the solution was approximately equally transparent. The ionic repulsion forces of the KD-1 were adequate to suspend the agglomerates within all the 1-6% vials for about 21 hours. By 24 hours the force of gravity of the growing agglomerates had exceeded the ionic repulsion forces and sedimentation was rapid. After 42 hours the agglomerates free to move had essentially all grown beyond the tolerance of the dispersant and sedimentation was complete.

Sintering Study

LSM Sintering Study

FEM images of the LSM powders utilized for the sintering studies characterized the morphology of the ceramic particles. The Inframat LSM powder consisted of spherical granules approximately 40 microns in diameter. (See Figure 50) The NexTech LSM powder consisted of approximately 0.5 micron particles conglomerated into 100 micron granules. (See Figure 51)

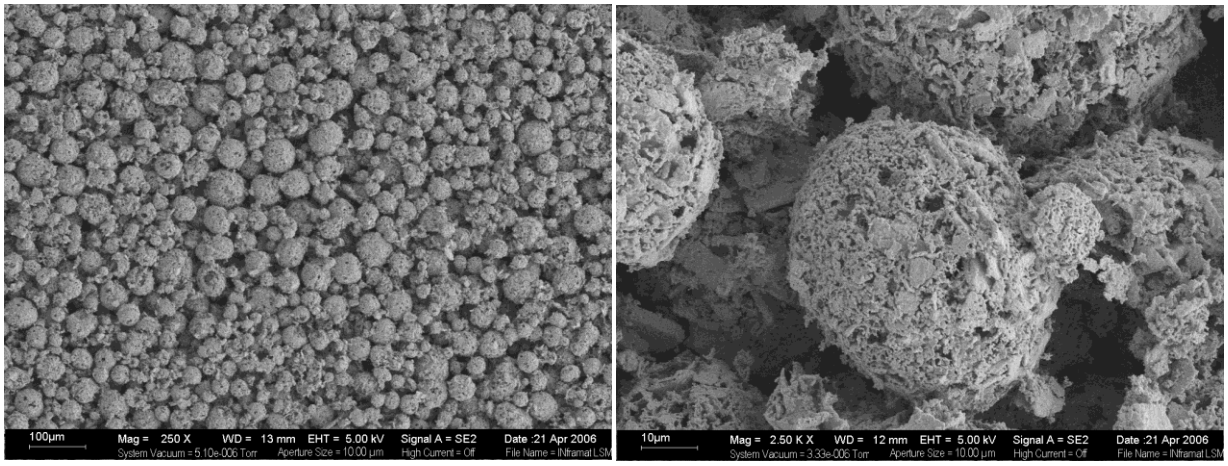


Figure 50 FEM Images of Inframat LSM 40 Micron Spherical Granules
(Left 250 X & Right 2,500 X Magnifications)

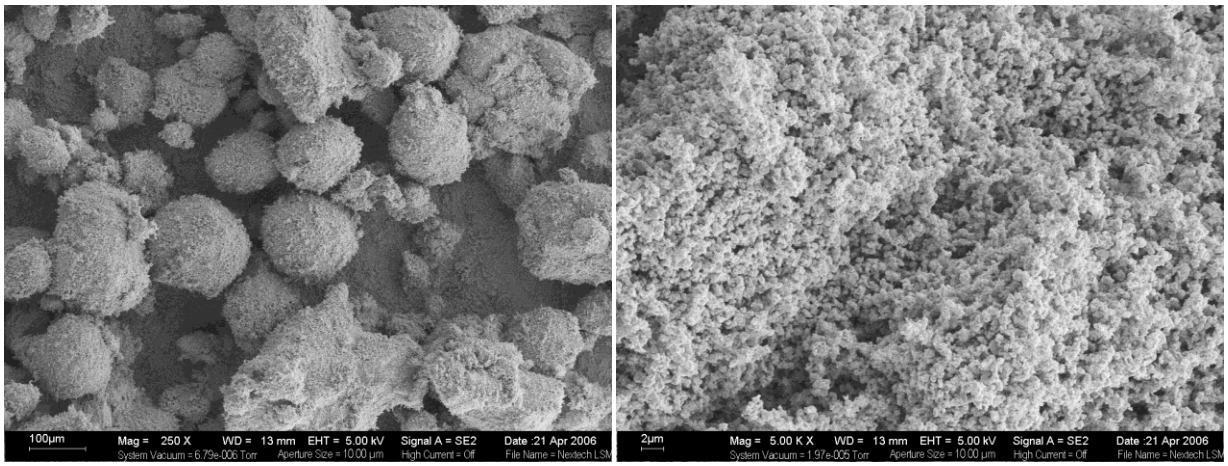


Figure 51 FEM Images of NexTech LSM 100 Micron Spherical Granules
(Left 250 X & Right 5,000 X Magnifications)

The LSM pellets uniaxially pressed at 175 MPa resulted in 59% and 56% relative green densities for the Inframat Advanced Materials and NexTech Materials powders, respectively. This is as expected since a conglomeration of small particles allows a denser packing configuration through the reduction of empty space between the spheres.

The Archimedes relative density measurements display a significantly lower overall value. (See Figure 52) The LSM is a porous structure and originally displaces the water equal to

the entire volume of the specimen including the pores. As the water penetrates into the sample the quantity of water displaced goes down. The duration which the specimens were left in the water bath was not adequate to permit all of the open pores within the structure to be filled. Therefore the geometric density measurements will be referenced for the remaining discussions.

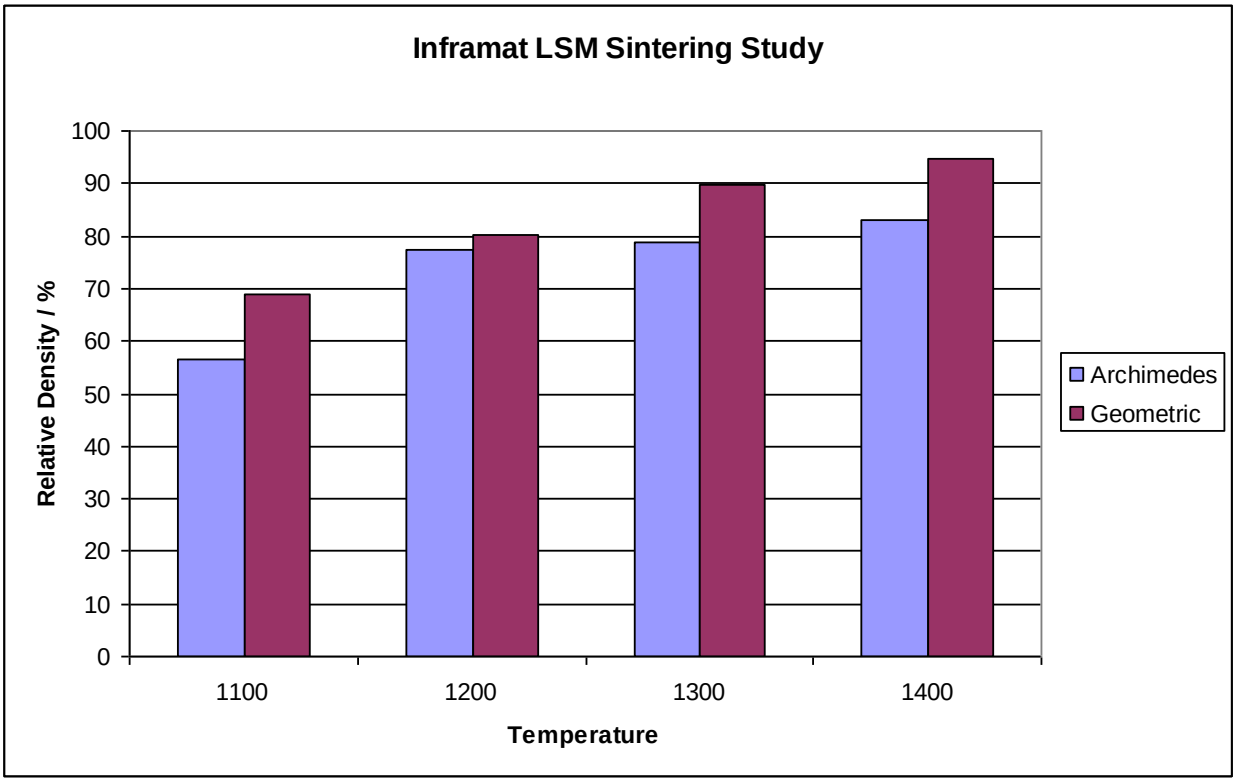


Figure 52 LSM Geometric vs. Archimedes Density Measurements Comparison

The pellets made of smaller granules sintered to a higher relative density (see Figure 53) and larger grains were grown (see Figure 53) at equal temperatures. This is attributed to the nature of the sintering behavior of the powder. Small granules have a larger surface area, in turn a higher surface energy, since more area is exposed to the solid-vapor interface. Sintering reduces the total free energy in the system with the introduction of heat energy that causes the

system mass to transfer between particles in contact with one another, reducing the particles' surface area.

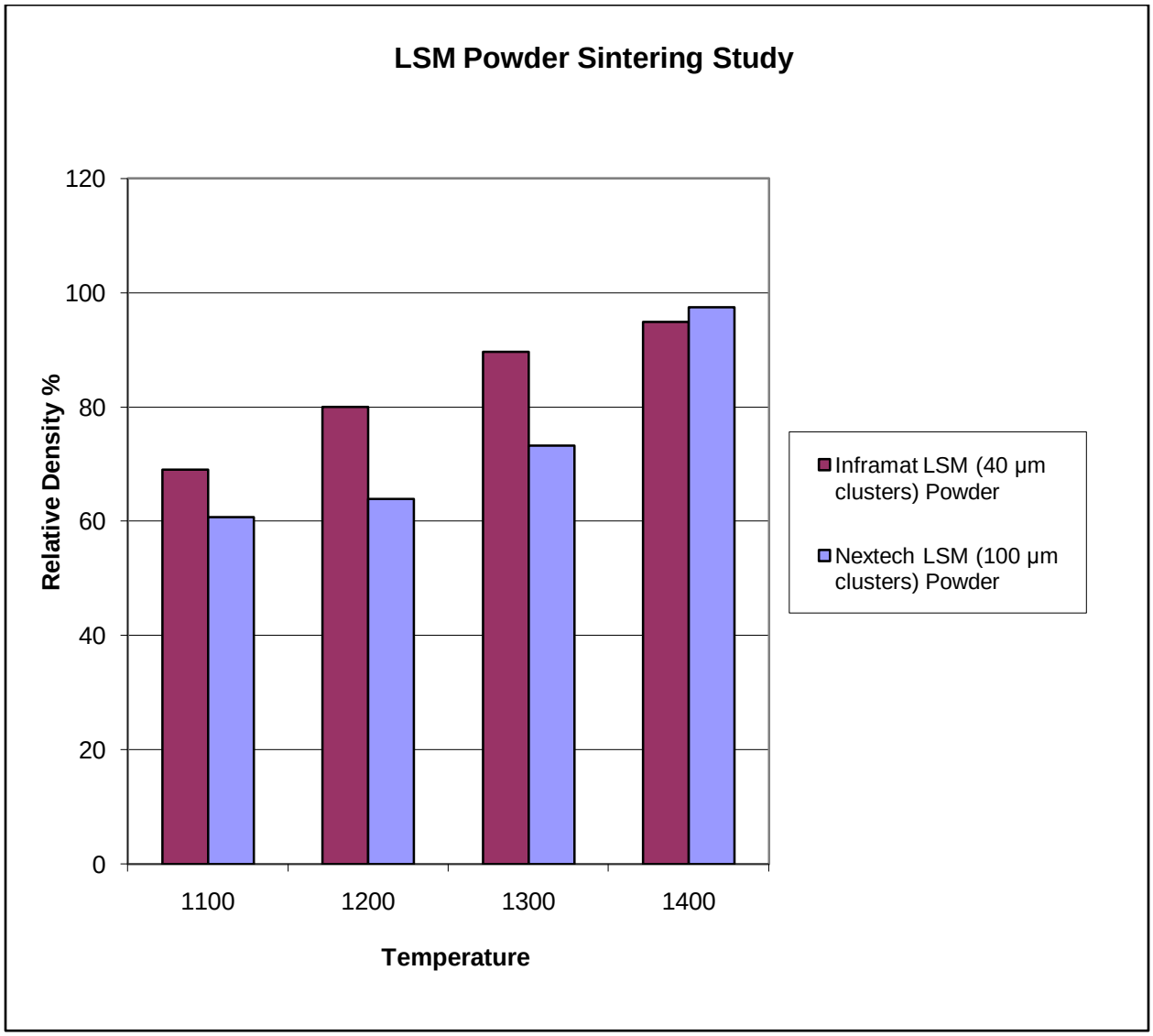


Figure 53 Relative Densities of LSM Pellets Sintered from 1100 – 1400 °C as a Function of Granule Size

The LSM from NexTech Materials sintered at 1300 °C exhibited a pore microstructure that demonstrated adequate mechanical strength and gas diffusion characteristics for electrochemical fuel cell testing. (See Figure 55)

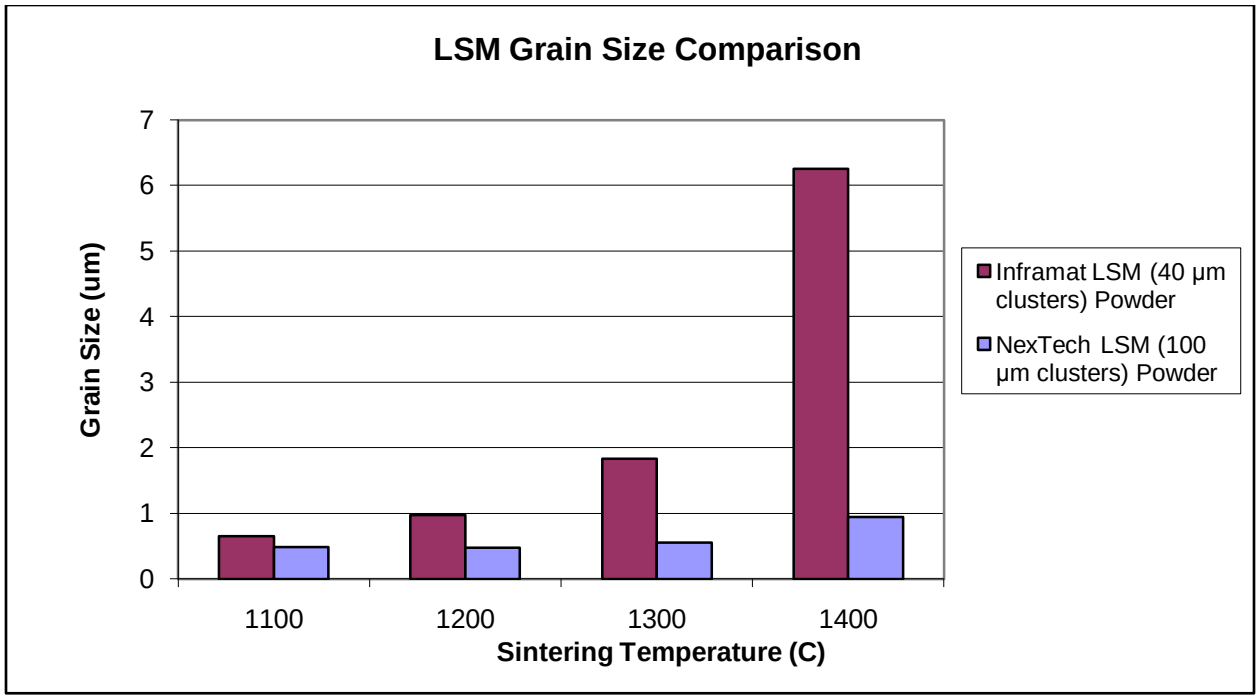


Figure 54 Grain Size in LSM Pellets Sintered from 1100 – 1400 °C as a Function of Granule Size

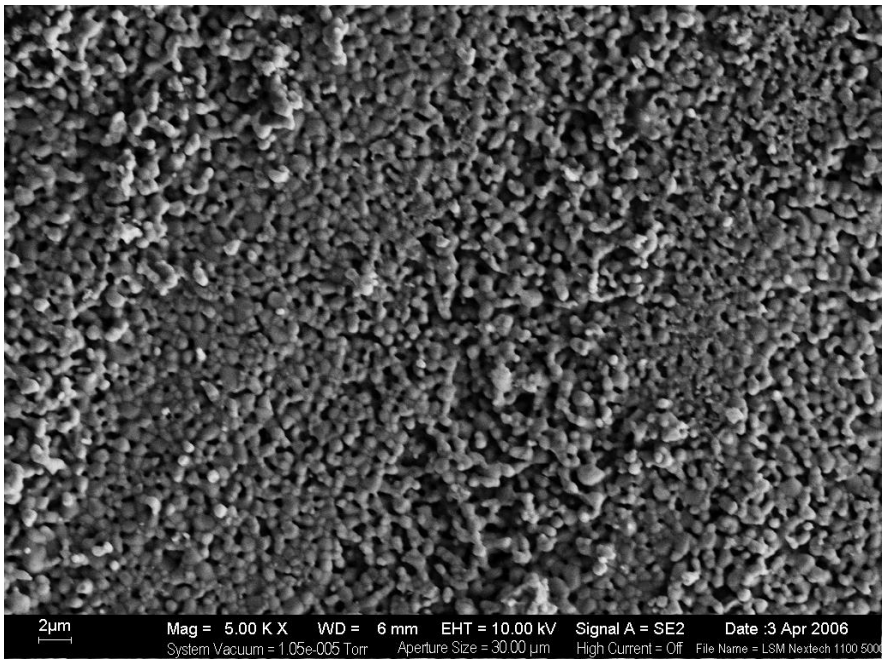


Figure 55 FEM Image of the Microstructure of NexTech LSM Sintered at 1300 °C

YSZ Sintering Study

FEM images of the YSZ powders utilized for the sintering studies characterized the morphology of the ceramic particles. The YSZ micro and nano powders consisted of particles no larger than approximately 500 and 30-60 nanometers in diameter, respectively. (See Figure 56)

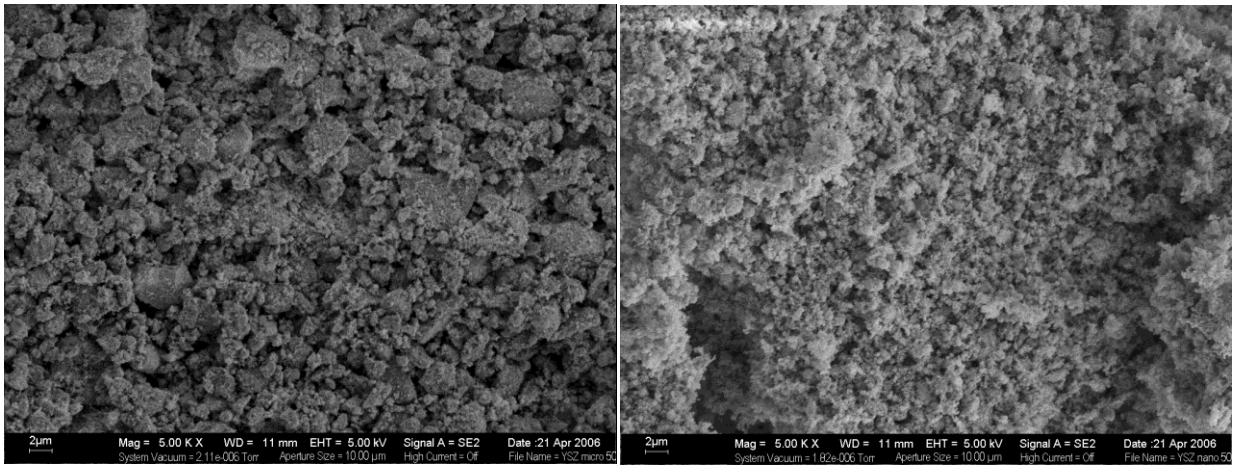


Figure 56 FEM Image of YSZ Micron (Left) and Nano (Right) Particles at 5,000 X

The YSZ pellets uniaxially pressed at 350 MPa resulted in 47.5% and 48.2% relative green densities for the micro and nano powders, respectively. The nano and micro pellets sintered to a maximum relative density of 89% at 1300 °C and 93% at 1400 °C, respectively. (See Figure 57)

FEM images of the YSZ powders demonstrate the three stages of sintering: (1) neck formation (2) densification and (3) grain growth. The nano powders sintering stages are encountered at 1100, 1300 and 1400 °C. (See Figure 58) The micro powders encountered the stages at the following higher temperatures due to the lower free surface energy: 1300, 1400 and 1500 °C.

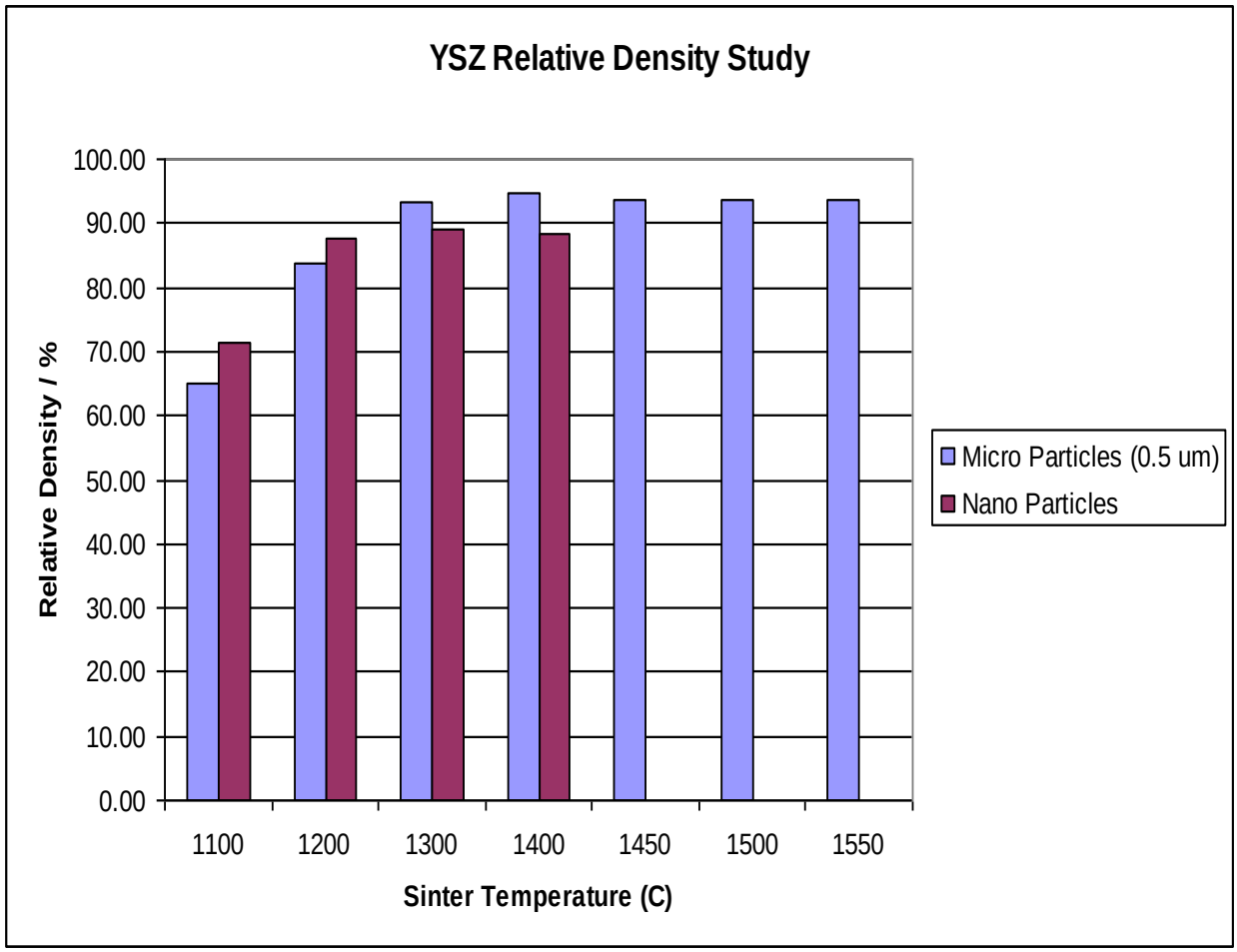


Figure 57 Relative Densities of YSZ Pellets Sintered from 1100 – 1550 °C as a Function of Particle Size

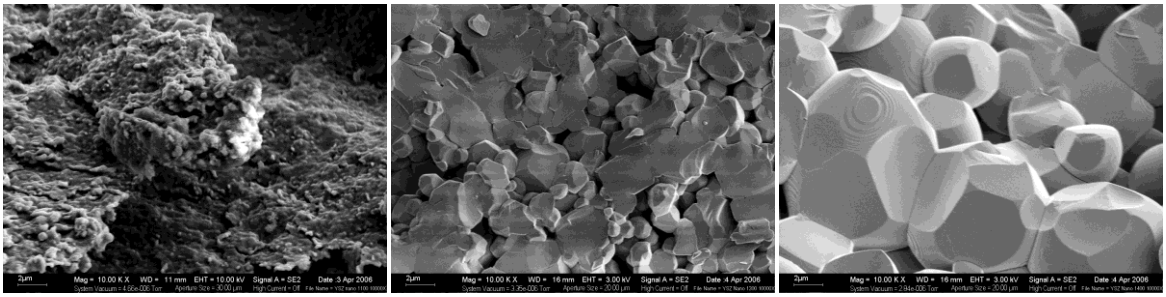


Figure 58 FEM Images of Nano YSZ Powders Sintered at 1100, 1300 and 1400 °C

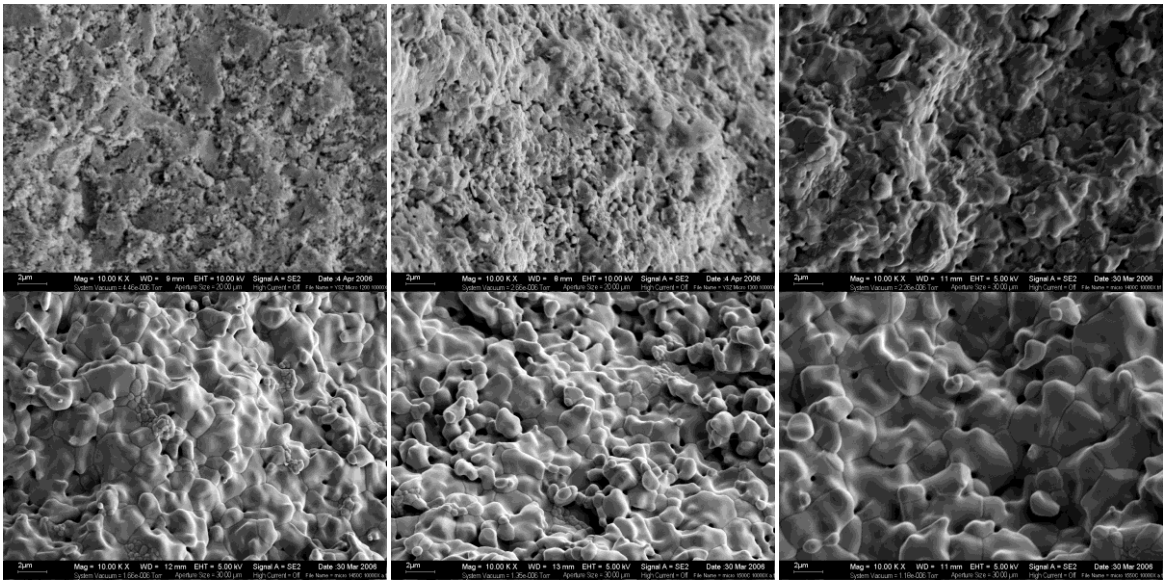


Figure 59 FEM Images of Micro YSZ Powders
Sintered at 1300, 1350, 1400, 1450, 1500 & 1550 °C

The grain growth stages were quantified and graphed. (See Figure 60) A dense electrolyte material which is nonporous to ensure fuel and oxidant do not mix was obtained at sintering temperatures above at 1300 and 1400 °C for the nano and micro powders, respectively. While grain boundary conductivity shows some future promise to improve ionic conductivity, grain boundary dominance requires grain sizes on the order of less than 100 nanometers, which is difficult to achieve through high temperature sintering processes. On the other hand from a macro perspective, ionic conductivity has been shown to be enhanced in a material with large grains. The overall ionic conductivity is decreased in -traditional micro-grain structures due to the dominant slow ionic transport between grain/boundary interfaces. [26] The mechanical strength of a ceramic is reduced with grain growth due to the decrease in concentration of grain boundaries. The impurities in grain boundaries permit ductile tearing at the tip of a crack, absorbing crack energy and increasing the overall structure's fracture strength. A grain size of 1

micron provides a balance between fast ionic transport through the large grains and mechanical strength. The nano and micro powders sintered for two hours at 1300 °C and 1500 °C result in grains of 1.5 and 1 microns respectively.

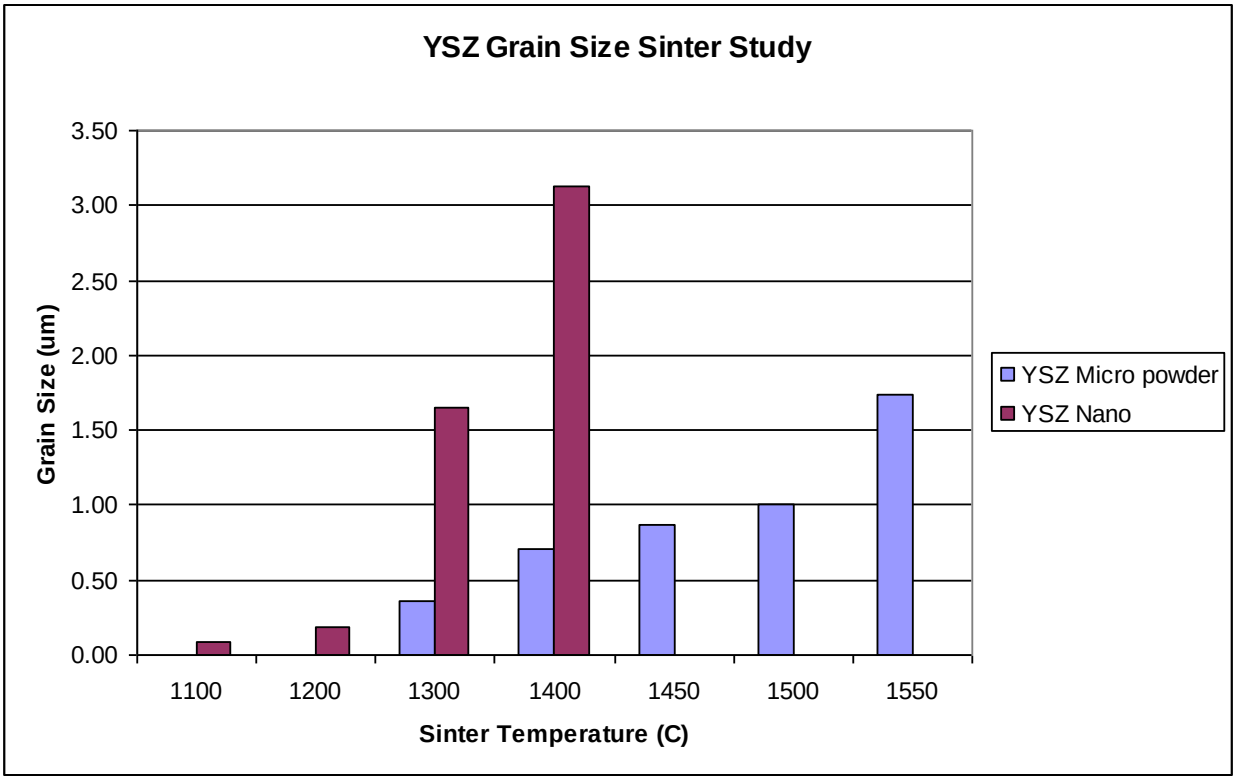


Figure 60 Grain Size in YSZ Pellets Sintered from 1100 – 1550 °C as a Function of Particle Size

Tape Sintering Study

An MSU fabricated micro YSZ electrolyte tape was sintered at maximum temperatures ranging from 1400-1550 °C to determine if grain growth and density coincides with the YSZ micron powder density study previously conducted.

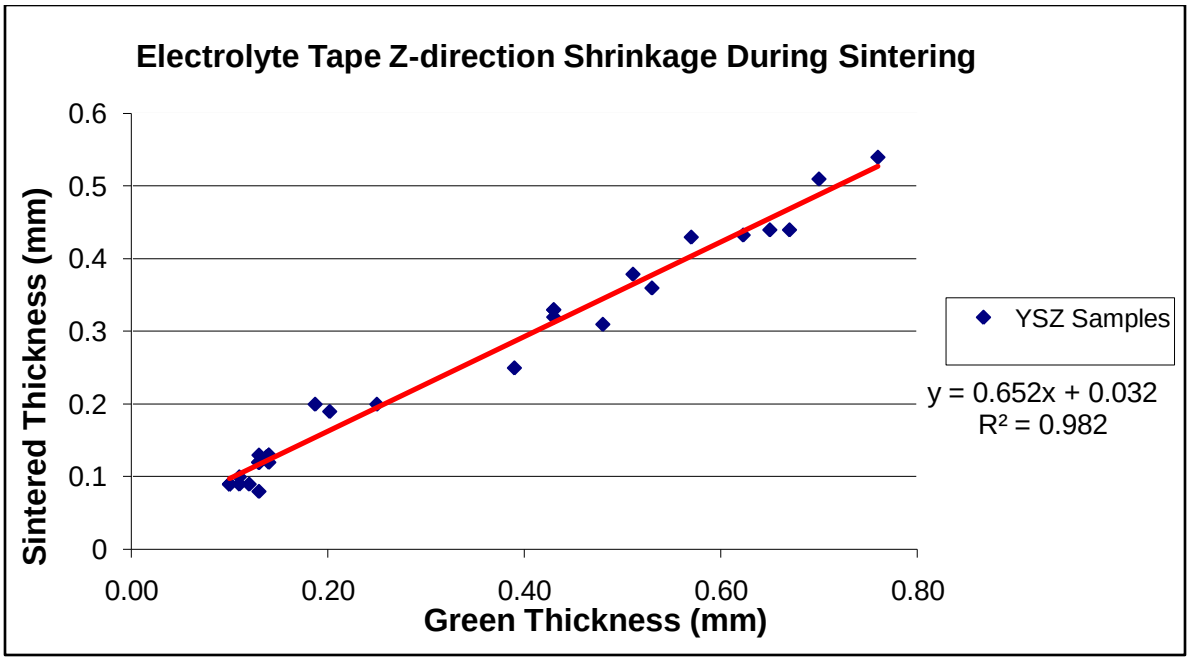


Figure 61 Sintering Shrinkage of YSZ Electrolyte Tape

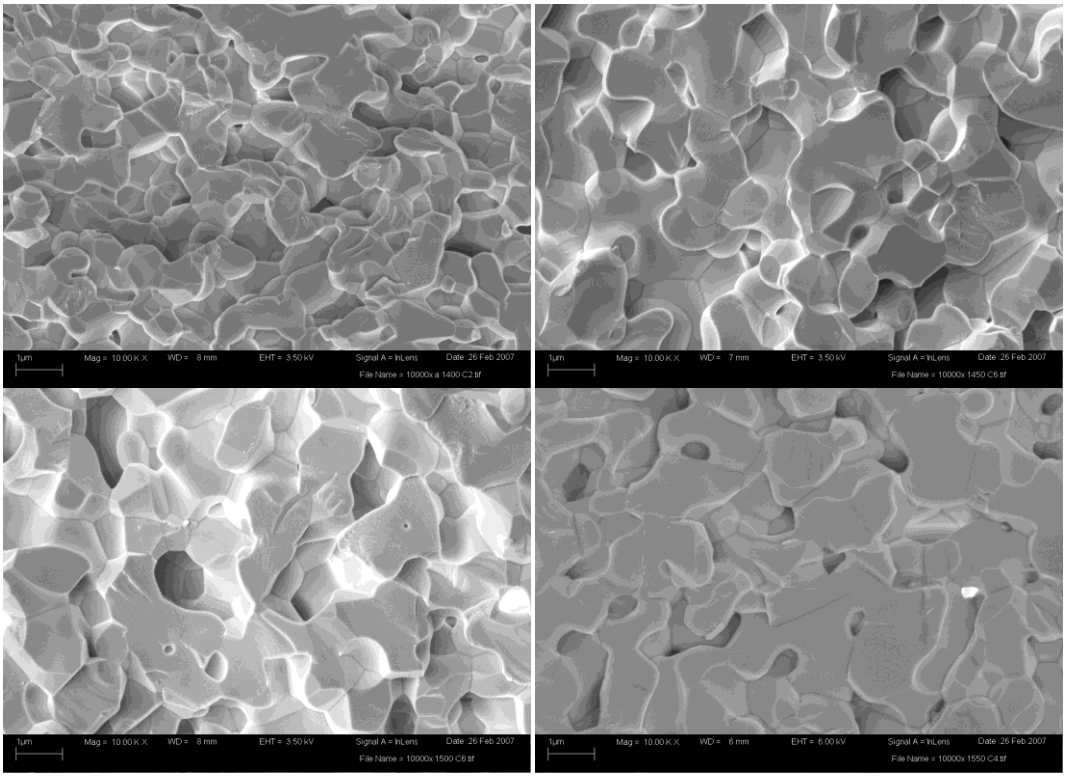


Figure 62 Micro YSZ Tape Cast Specimens Sintered at
1400 (top left), 1450 (top right), 1500 (bottom left) & 1550 (bottom right) °C

FEM microstructure images show results correspond and the optimum maximum temperature remains 1500 °C. During sintering of an YSZ tape with laser drilled linear channels on one side excess pressure restricted shrinkage, causing a crack to form and propagate from the high stress region at the bottom corner of a channel. (See Figure 63) This required additional care in the placing of weight and surface of the setter when sintering UniCell's.

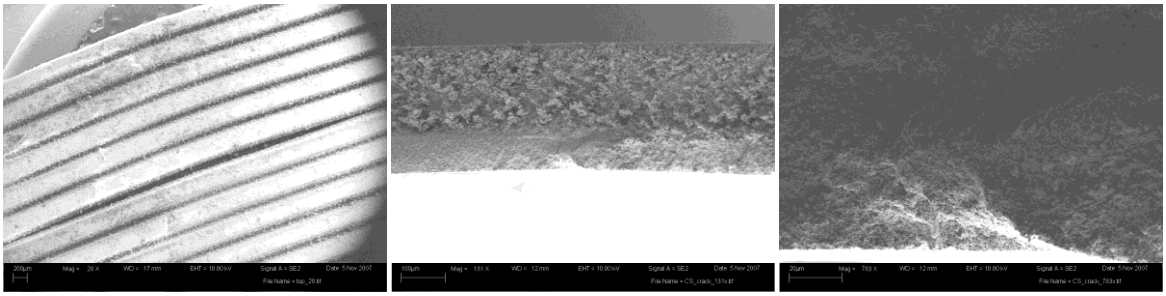


Figure 63 FEM Images of Linear Laser Drilled
Fracture Caused During Sintering Due to Excess Pressure

Tape Cast Optimization

To ensure consistent and homogonous slurry was obtained, originally 350 grams of milling media was used. The removal of some of the milling media for the second period was originally utilized to decrease the shearing effects during the second stage and reduce the breakdown of the binder matrix. However, this resulted in an unpredictable quantity of slurry being lost, adversely affecting the concentration levels of the constituents. The total quantity of milling media in the first stage was reduced to 250 grams where an audible sound of the media hitting the bottom of the container was still evident. The same amount of media was then used for the second milling period.

Initially the tape cracked throughout entire length. The type I plasticizer content was increased from 5.0 to 6.0 weight percent and the flexibility of the tape was increased between

cracks, but the cracks were not eliminated. The type II plasticizer was increased 4.0 to 5.0 weight percent and the tape demonstrated a higher ability to plasticity deform between the cracks, but a decrease in the quantity of cracks still was not observed. The KD-1 dispersant was believed to not work effectively with the binder since it has been reported that the B-98 binders have a tendency to replace some of the dispersant on the particle surfaces, absorbing the binder and dissolving the dispersant back into the solution [15]. The amount of binder available for forming the polymer matrix to absorb the ceramic solids was diluted and could not form a continuous matrix free of cracks. The replacement of the KD-1 with MFO allowed the type I and II plasticizer contents to be decreased back to the original 4.0 and 5.0 weight percent, respectively, without the presence of cracks in the tape.

The slurry particles that remained agglomerated after the ball milling cycles were removed by filtering. The slurry needed to be degassed in a vacuum to remove air bubbles which got trapped during casting. These air bubbles left a pore or void in the electrolyte layer, prohibiting complete densification and initiated flaws within the microstructure.

Thickness variations along tape direction length were minimized with the use of a double doctor blade. The double blade offered a reservoir that maintained a more consistent slurry height level during casting by stabilizing the hydrodynamic pressure. To obtain a more consistent profile from left to right the slurry casting granite block and aluminum casting bed were precisely leveled. Edge effects were decreased with the increase of tape cast speed from 20-40. The decreased tape cast speed of 20 unsuccessfully resulted in outward flow. Increasing the speed of the mylar sheet increased the shearing force on the slurry and eliminated welling. The suspected binder breakdown led to a 2 stage ball milling period study (24 & 72 hours). Tape

casts slurries that utilized a 72 hour ball milling second stage demonstrated significantly more outward flow on the edges. This resulted in less consistent green thicknesses for tapes cast at the same exact settings. The 24 hour ball milling period reduced the breakdown of the binder and in turn edge effects. The binder remained intact after 24 hours and resulted in tapes with straight edges and a more consistent green tape thickness. (See Figure 64)

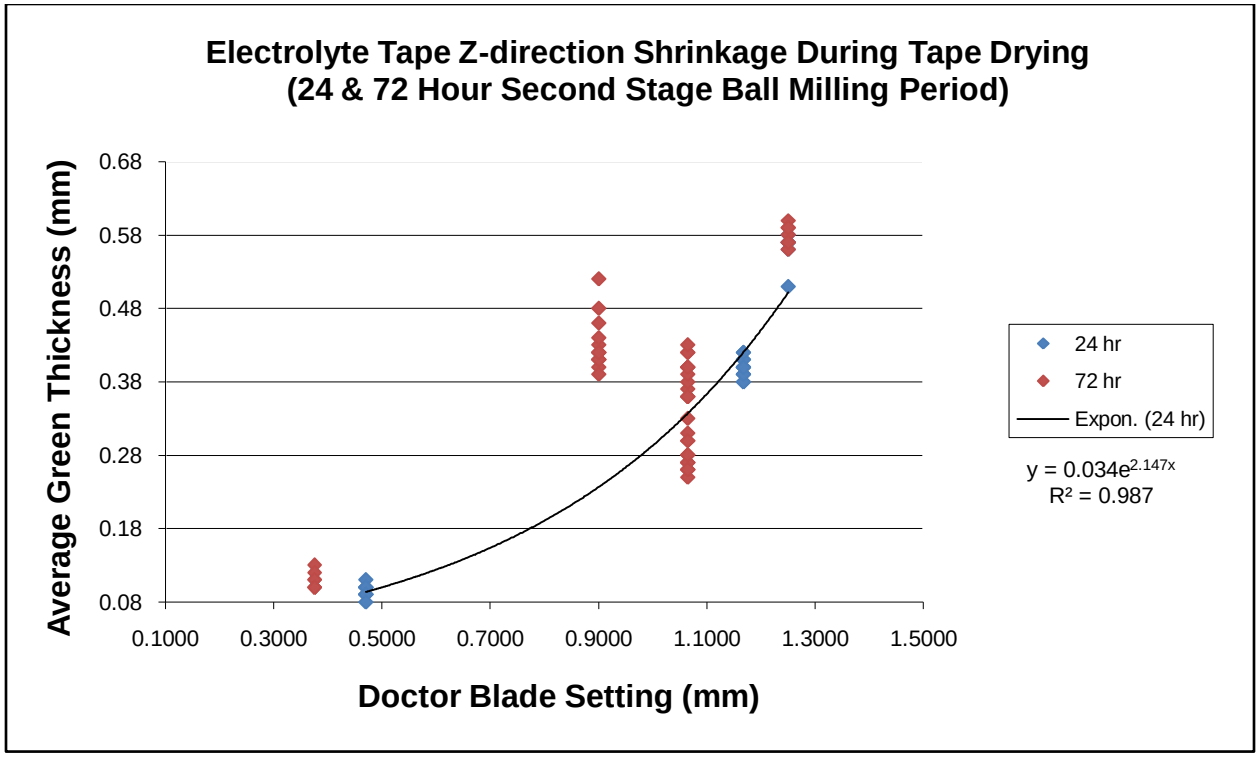


Figure 64 Shrinkage during Tape Drying

Sintering of the YSZ tapes with 58.6% solids loading caused ripples to form around the edge of the sample. This was a combination of the large diameter samples (3 inch) and the relatively large linear shrinkage during sintering. The tape shrank significantly more than a commercial tape because the ESL commercial tape had a denser green body. Therefore in order to increase the green density of the MSU electrolyte tape we increased the solids loading to 60%. Increasing the solids loading created a deficiency in binder to hold together the ceramic particles,

increasing the viscosity of the slurry and causing edge effects and cracking again. The binder concentration increase from 7.75 % to 8.00% minimized flow outward during casting and resulted in a crack free tape. The denser green tape in combination with the optimized 24 hour sintering cycle resulted in a cell with minimum curvature.

Dilatometer Studies

The micro and nano powder pellets reached their maximum linear shrinkage after a dwell at 1400 and 1300 °C respectively. This is evident in Figure 65 and Figure 66 where the linear shrinkage is no different in equal sized samples sintered at the two highest temperatures. From 1400 to 1500 °C in the micro powder and from 1300 to 1400 °C in the nano powder the density of the pellets was not changed and only pure grain growth was evident in the sintering and dilatometer studies. (See Figure 65 and Figure 66)

The linear shrinkage as a function of temperature, for the samples of the same powder, all followed the same path until the various dwell cycles were started. The linear section of these curves demonstrates that when held at a constant temperature the rate of shrinkage is constant. It can therefore be concluded that the sintering shrinkage rate is independent of the rate at which the sample is heated. A sample held at any temperature above which densification is present for long enough will eventually reach a fully dense substrate. The maximum temperature sintering cycle curves flatten out at high temperatures where sample shrinkage ceases as it reaches maximum density.

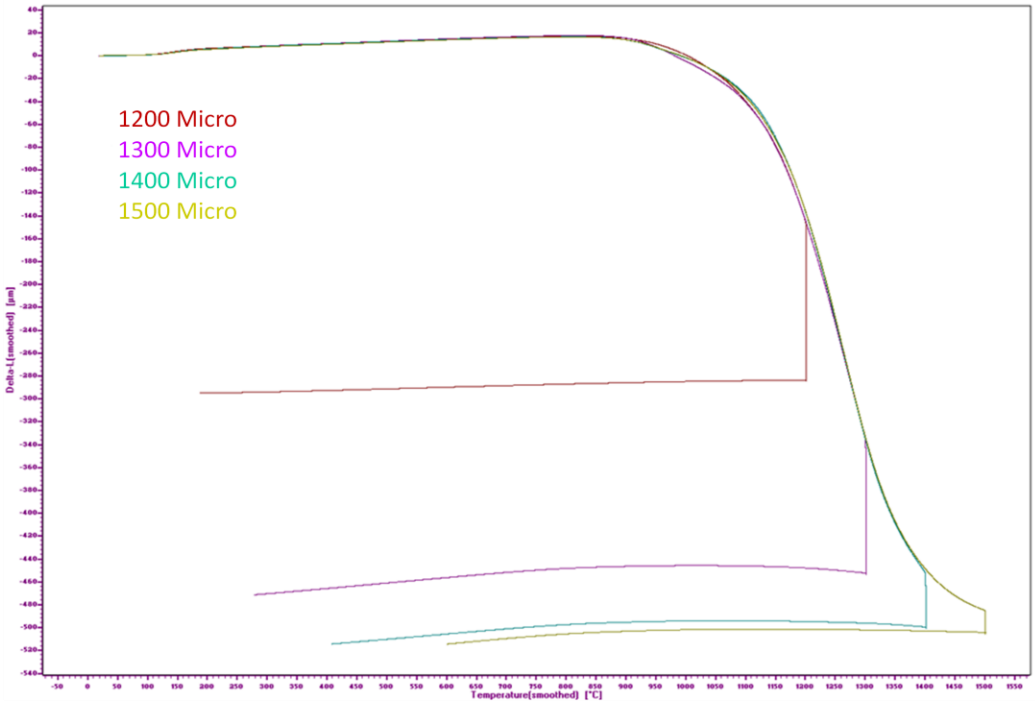


Figure 65 YSZ Micro Particle Pellets Dilatometer Sintering Study from 1200 to 1500 °C

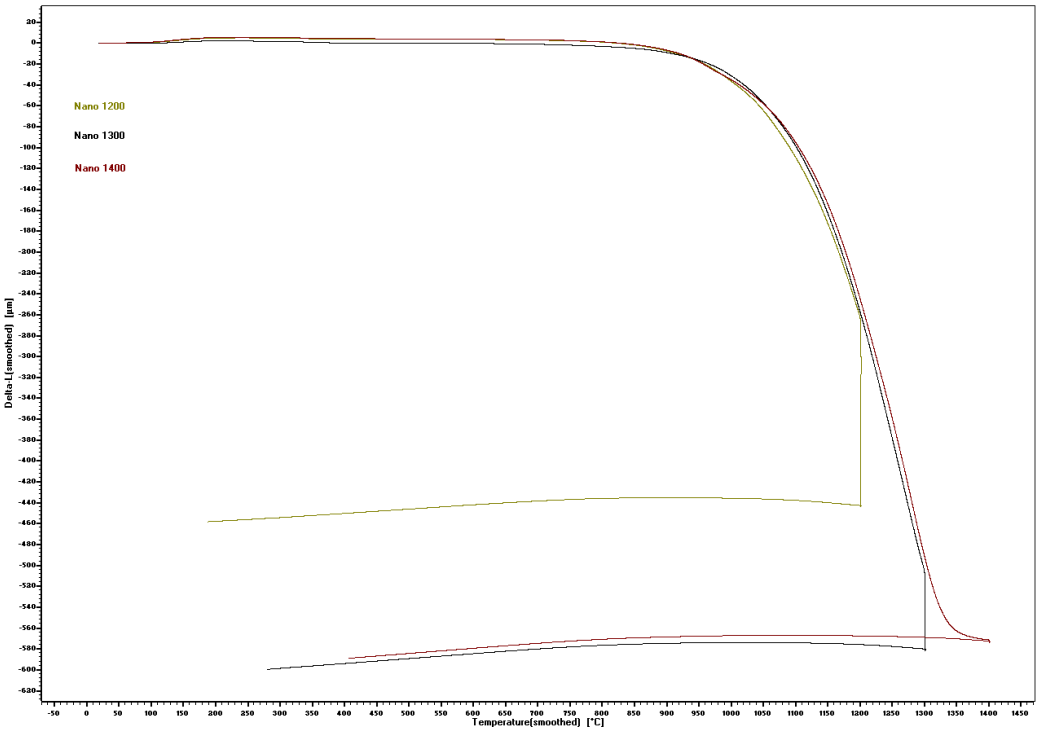


Figure 66 YSZ Nano Particle Pellets Dilatometer Sintering Study from 1200 to 1400 °C

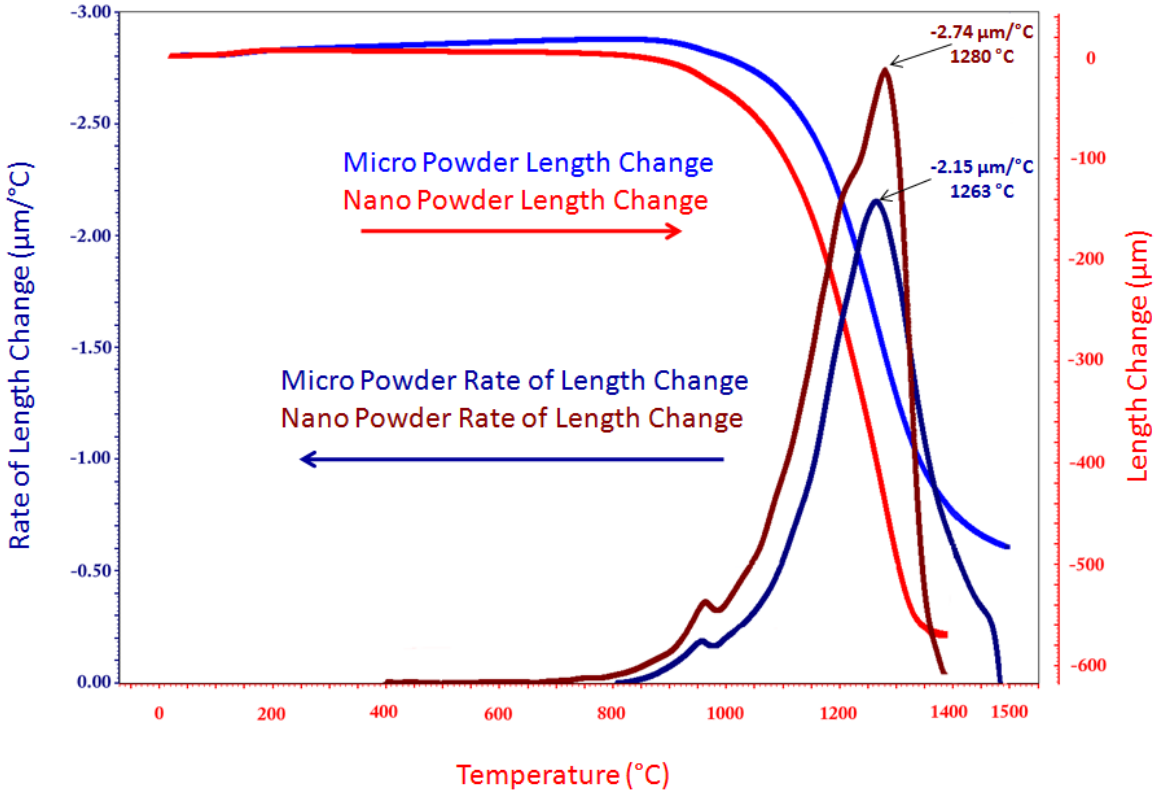


Figure 67 Sintering Shrinkage Rate as a Function of Temperature

The derivative of the highest temperature cycle curves provides the rate at which these samples are shrinking. (See Figure 67) The initial bump in the beginning of the rate curves is due to the transition of the tape from thermal expansion to the beginning of the densification stage. The nano powder sinters more rapidly and displayed a more rapid transition from densification to grain growth than the micro powder.

The CTE of a sintered YSZ tape substrate operated at 800 °C measured via a dilatometer is approximately $10.2*10^{-6}$/K at 800 °C. This coincides with value reported in the literature.[1]

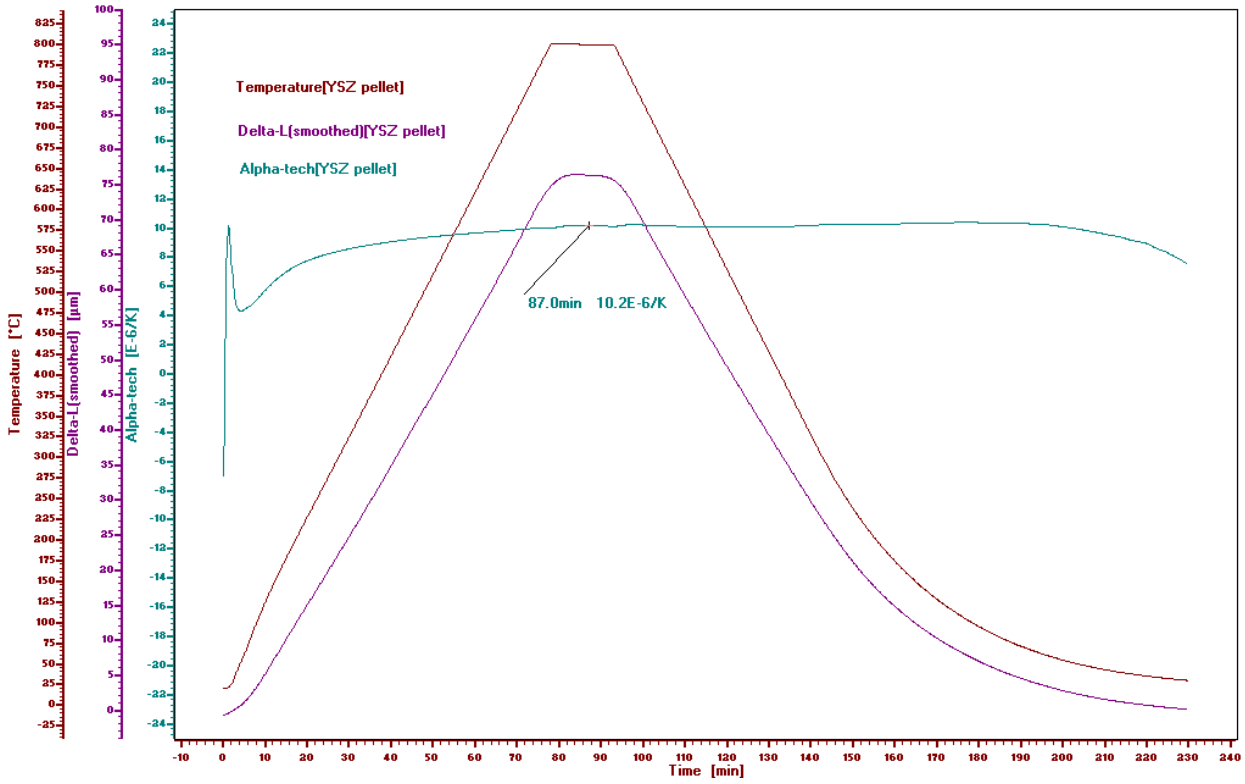


Figure 68 Dilatometer measurement of YSZ CTE up to 800 °C

Thermal Gravimetric Burnout Study

The organic burnout rates of the solvent, binder, dispersant and plasticizers in YSZ tapes were characterized via thermal gravimetric analysis. The different portions of the TGA curves can be attributed to the release of the different constituents based on their reported boiling points. (See Table 10) The rates of organic burnout were minimized through a series of TGA tests by varying the sintering temperature profiles and monitoring the change in slope of the TGA curves. (See Figure 69)

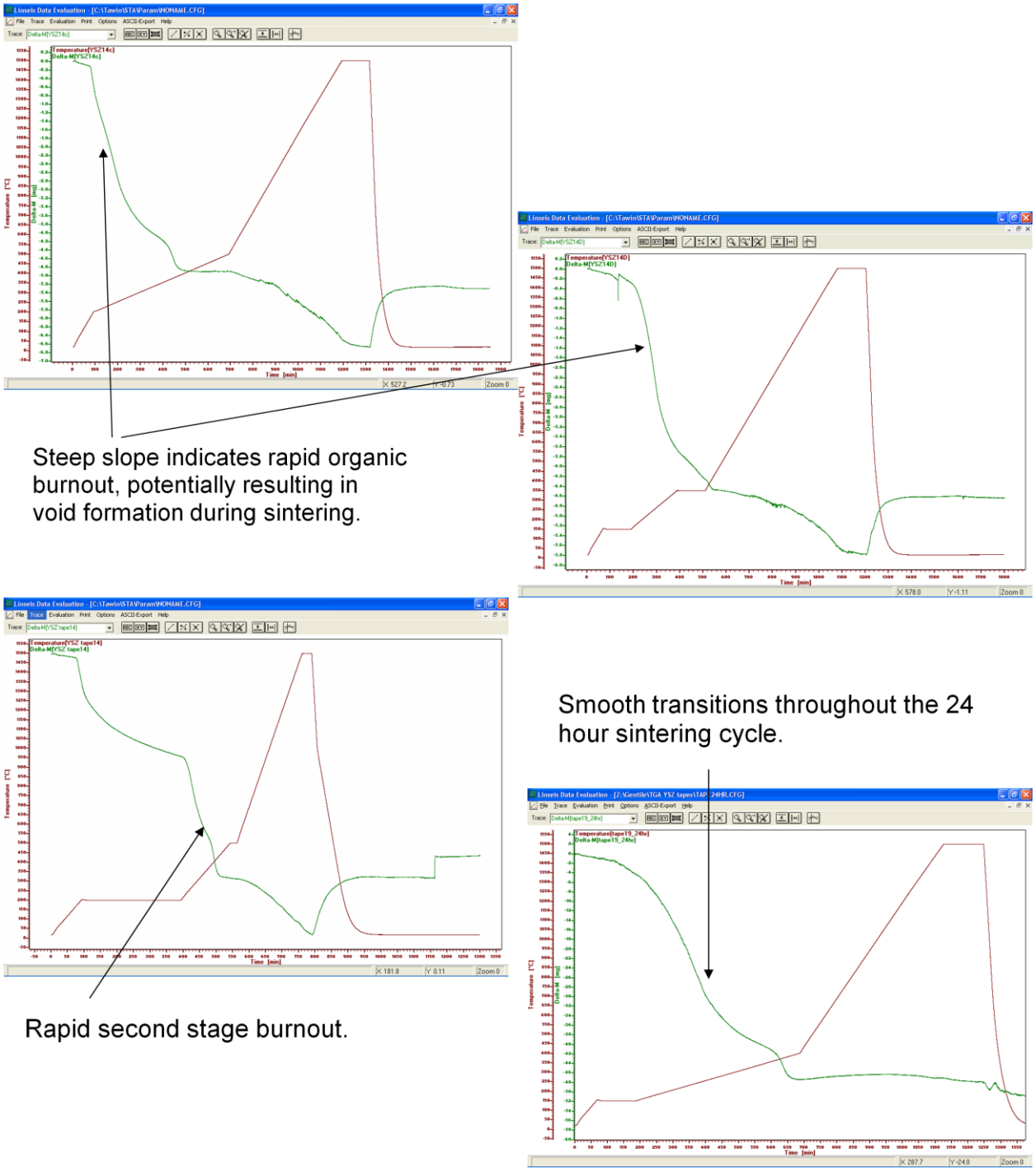


Figure 69 TGA Curves of YSZ Electrolyte Tapes at Varying Sintering Temperature Profiles

Table 10 Boiling Point of Organic Constituents in MSU YSZ Tape

Constituents (Reference Source)	Boiling Point
Ethyl Alcohol [27]	78 °C
Xylene [28]	135 – 145 °C
Polyvinyl Butyral B-98 Binder [18]	140 – 200 °C
Polyalkylene Glycol Type II Plasticizer [29]	249 °C
Blown Menhaden Fish Oil (MFO)Dispersant [30]	> 250 °C
Butyl Benzyl Phthalate S-160 Type I Plasticizer [31]	370 °C

The ethyl alcohol and xylene were burned out as the sample was heated from ambient to 150 °C at 2 °C/min. The tape was held at 150 °C to slowly decompose the binder matrix at the Polyvinyl Butyral B-98 lower boiling point. A slow decomposition of the binder resulted in a tape without significant warping and internal flaws. The MFO dispersant, Polyalkylene Glycol Type II Plasticizer and Butyl Benzyl Phthalate S-160 Type I Plasticizer were burned out of the sample very slowly through a ramp rate of 0.5 °C/min from 150 to 450 °C. The final 24 sintering temperature profile used (see Figure 70) could be further optimized by minimizing the Butyl Benzyl Phthalate S-160 Type I Plasticizer burnout rate at approximately 370 °C.

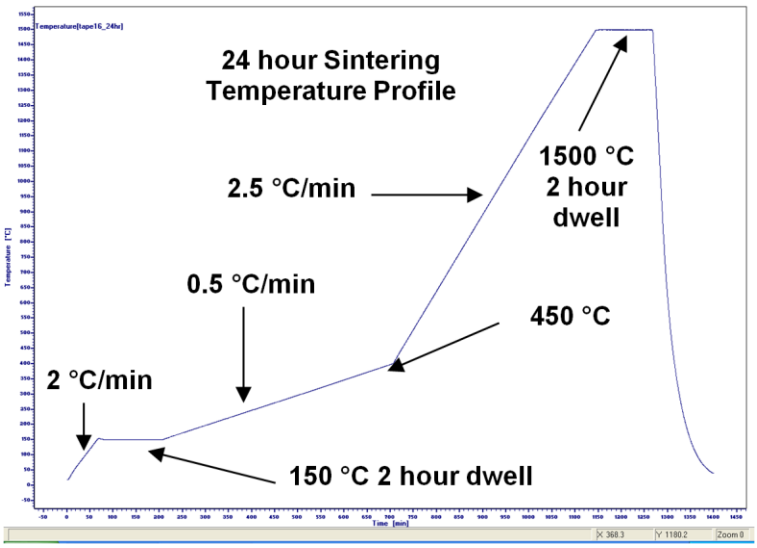


Figure 70 TGA Optimized 24 Hour Sintering Temperature Profile

The rapid organic burnout of the constituents in the electrode inks was observed. (See Figure 71) This may result in high processing stresses during the co-sintering of the electrodes on the sintered electrolyte considering the very small cross-sectional thicknesses introduced in the UniCell. Optimization of this process will significantly reduce interlayer stresses, in turn minimizing the potential for delaminating and catastrophic failure due to crack propagation.

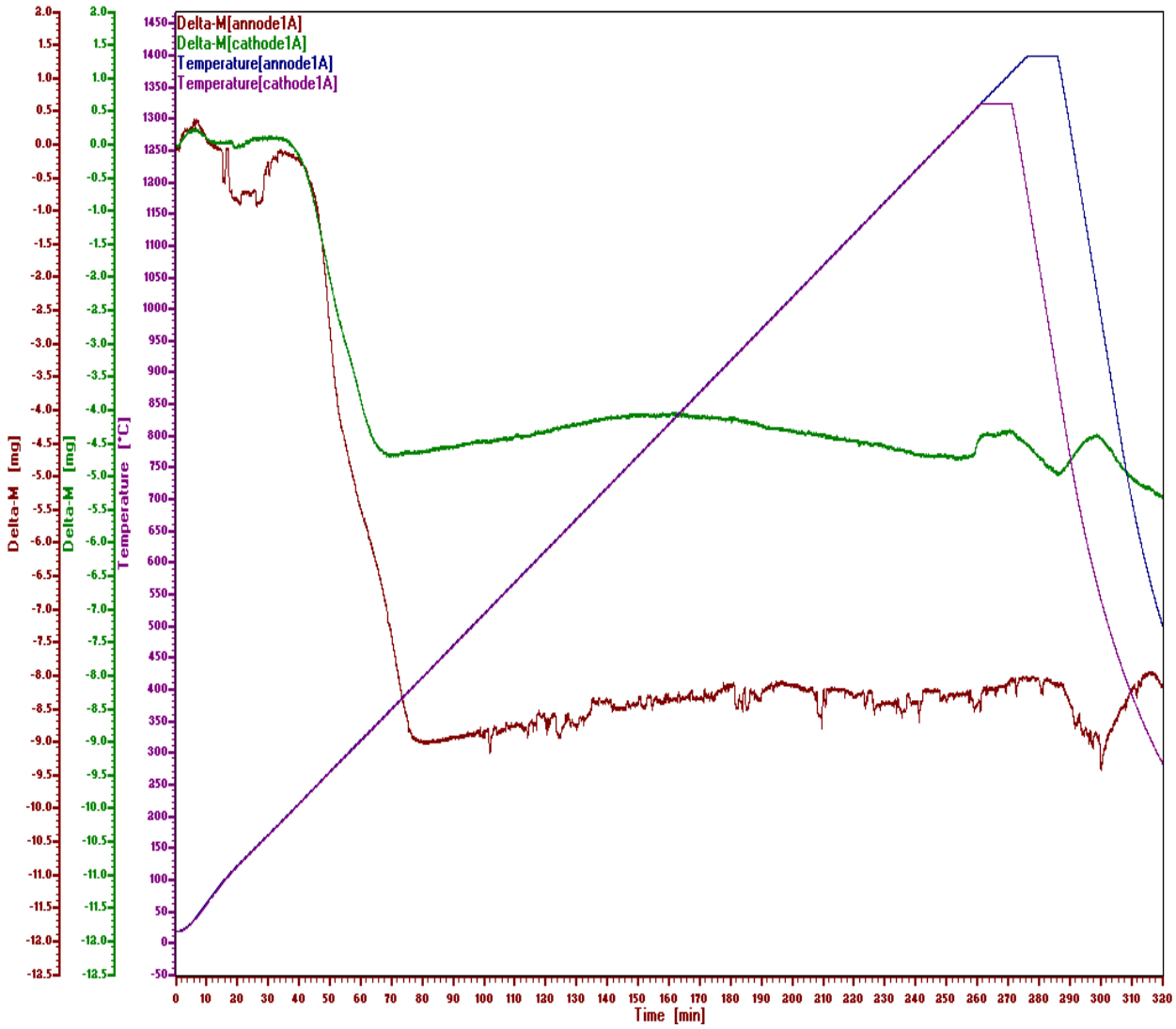


Figure 71 TGA Curves of Organic Burnout Rates in Electrode Inks at the Utilized Co-Sintering Rate

Surface Contouring

Interleaved Hole Patterns

The interleaved linear hole pattern machined into the green and sintered 8 mol% YSZ electrolyte tapes showed significant different profiles. The sintered ceramic was less conducive to machining of the interleaved features because of its brittle, highly dense nature. The amount of energy lost to heat during laser drilling was a function of the ceramic density, feature size, material thickness and laser pulse rate. The dense sintered ceramic particles were bonded together much stronger, requiring a higher intensity process to break the bonds and remove material. The increased intensity required to laser machine the sintered parts introduced high levels of heat energy into the ceramic and resulted in the formation of the heat affected zone (HAV) around the introduced features. (See Figure 72 Sample #1)

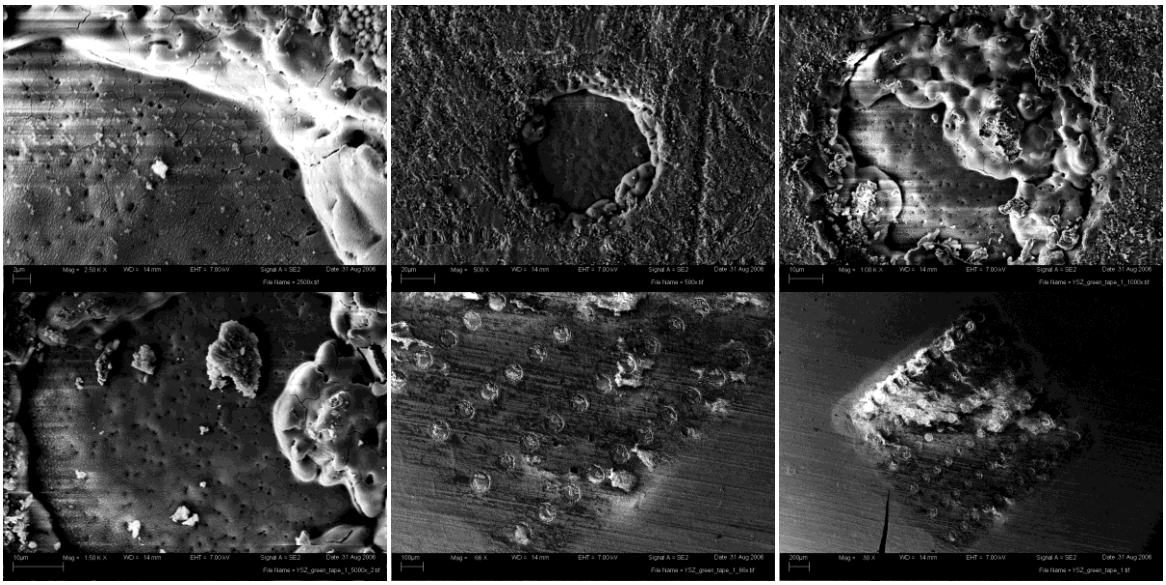


Figure 72 FEM Top Views of Blind Holes Laser Drilled in A Sintered Disc
Reference # (1) Top Left (2) Center (3) Right (4) Bottom Left (5) Center (6) Right

The thin recast layer formed in the HAV also contained high concentrations of mircostructural flaws which led to poor mechanical strength relative to standard ESC electrolytes. The material around the introduced features went into the liquid phase and re-solidified irregularly when the holes were attempted to be drilled at the desired blind depth in sintered samples. The shape and size of the molten region was not limited to the laser beam spot size, rather it varied throughout the individual samples resulting in inconsistent feature profiles. (See Figure 72 Sample #3) Surface debree was physically bonded to the surface. (See Figure 72 Sample #4) Shock waves caused surface ripples and damage to the adjacent structures. (See Figure 72 Samples #5 & 6)

The holes laser drilled into the green substrates slightly demonstrated the heat affects due to the small feature diameter versus blind depth that limited heat transfer away from the surface through the gas medium. The heat was forced to travel through the bulk material creating a small HAV. However the holes in the green sample were still capable of being drilled to the desired depth with a conical profile. The laser drilled prototype shown in Figure 74 decreased the ionic transport path length to 40 μm from one hole surface to another.

The sintering of the green ceramic after the laser micromachining allowed for the migration of material into voids around the machined features, self healing these flaws. The sintering of the green tapes after machining also slightly rounded the corners of the features, reducing the amount of high stress concentration regions. (See Figure 74)

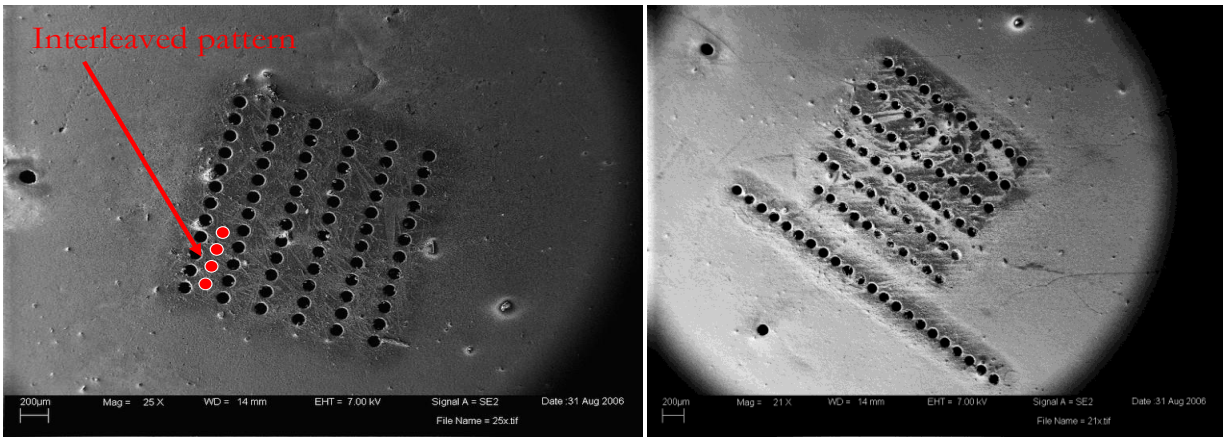


Figure 73 FEM Images of the Linear Interweaving Pattern of Blind Holes in a Green Electrolyte Tape via Laser Pulsing and CNC Controlled Translation

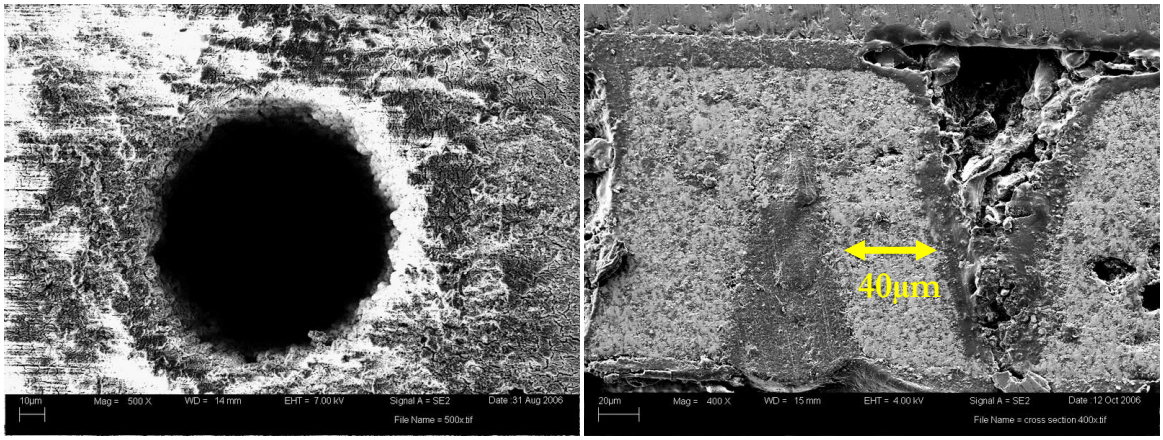


Figure 74 FEM Top & Cross Sectional Views of a Blind Hole Laser Drilled in Green Electrolyte Tape

Microscopic hole patterning via photo resist machining was investigated to attempt to achieve a more uniform profile of the holes, reduce process costs and improve manufacturing speeds. During the micro-via hole photo resist machining a thin film was applied to the top and bottom of the tapes. Upon completion of the photo resist machining these layers needed to be removed. Due to the minimum material left after the hole pattern the structure integrity was not preserved and the protective layers could not be removed without fracturing the part.

During initial prototype manufacturing of both interleaved hole patterns difficulty working with the originally desired 150 micron tape was encountered. The thin electrolyte demonstrated poor mechanical strength. The interleaved checkerboard design removed significantly more material due to the close proximity of hole features. The laser drilling of this prototype design in green electrolyte tapes resulted in a substrate that did not preserve the mechanical integrity and permit handling. It was decided in order to prove the concept a thick electrolyte with the surface contouring would be compared to the unaltered thick electrolyte of 400 microns thick.

Interleaved Concentric Channels

The interleaved concentric channels were successfully laser drilled utilizing an excimer laser. The soft green electrolyte, channel width to height ratio and continuous nature of the channels (compared to holes) permitted the near complete vaporization of material into a plasma plume, leaving behind only small amounts of heat that were dissipated through the gas between pulses. Minimal heat diffusion into the body resulted in a more efficient, accurate and cleaner process without introducing thermal stresses to the part.

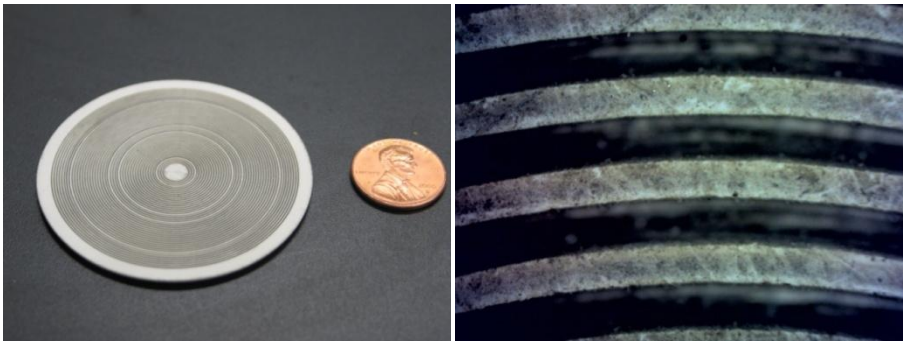


Figure 75 Digital (Left) and Optical 50X (Right) Images of Green UniCell Electrolyte with Concentric Channels Prior to Initial

The small aperture excimer laser (10 microns) limited the heat affect slightly but required ten passes per channel. This resulted in a square bottom channel with high stress points at the channel corners and unacceptable machining durations for one sample. A consistent depth profile was obtained (see Figure 76), however additional excimer laser testing to determine the optimum pulse rate for achieving the exact depth profile would be required.

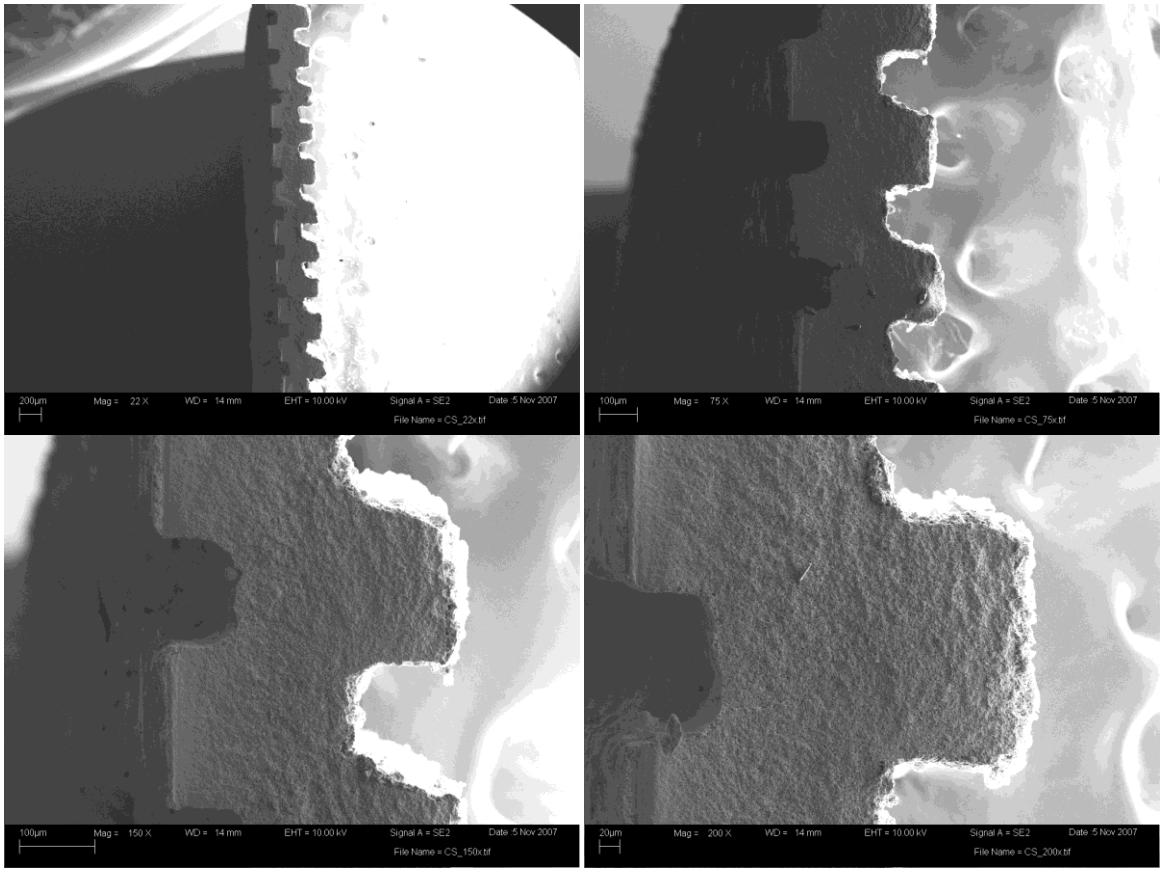


Figure 76 Cross Section of Concentric Channel Features in the Complete UniCell Including Electrodes (Anode on Left) After Co-Sintering and Electrochemical Testing (From top left to bottom right: Magnifications 22 and 75, 150 and 200)

The application of electrodes to the UniCell prototype with concentric channels completely coated the top surfaces, channel walls and channel bottoms; eliminating concerns of the ability to evenly disperse the inks via simple aerosol spraying. (See Figure 77)

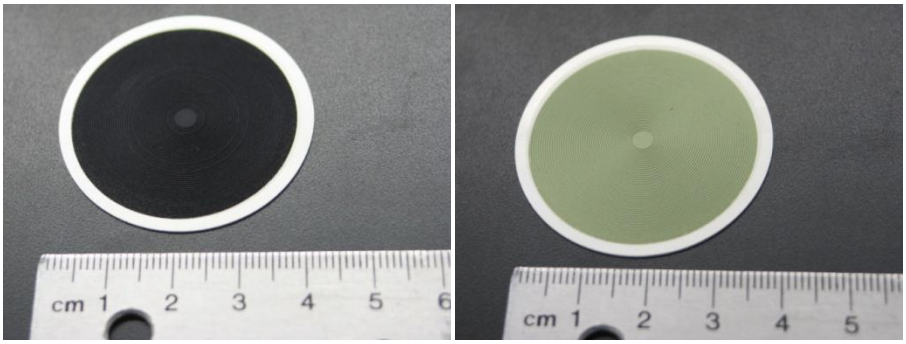


Figure 77 Digital Images of UniCell LSM Cathode (Left) and Ni-YSZ Anode (Right) Prior to Co-sintering

FEM images of the top and bottom of the anode and cathode channels show a consistent microstructure of the desired porosity in accordance with previously discussed sintering studies. (See above) The electrode thicknesses are consistently 15 microns across all channel surfaces.

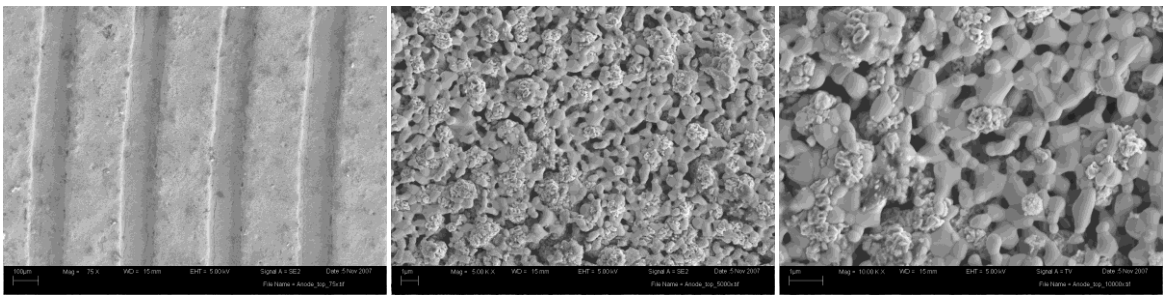


Figure 78 FEM Images of the Top of the Anode Side Channels Post Electrochemical Testing (75, 5,000 and 10,000 Magnifications)

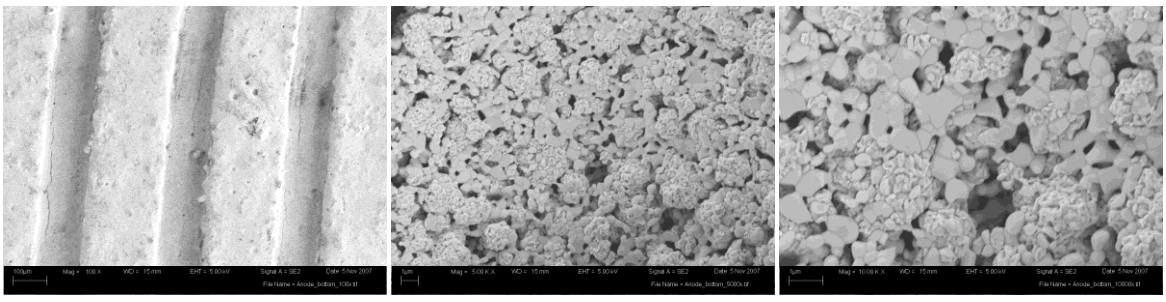


Figure 79 FEM Images of the Bottom of the Anode Side Channels Post Electrochemical Testing (100, 5,000 and 10,000 Magnifications)

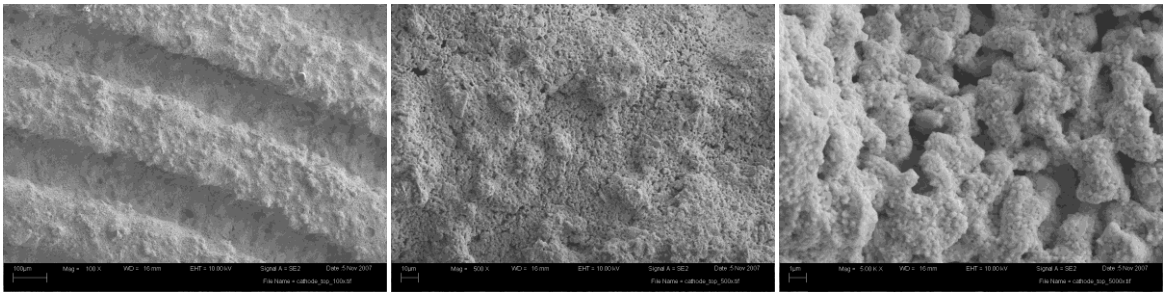


Figure 80 FEM Images of the Top of the Cathode Side Channels Post Electrochemical Testing (100, 500 and 5,000 Magnifications)

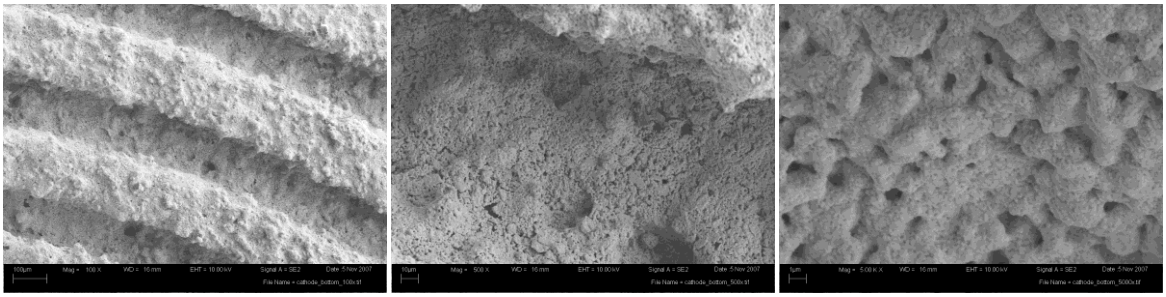


Figure 81FEM Images of the Top of the Cathode Side Channels Post Electrochemical Testing (100, 500 and 5,000 Magnifications)

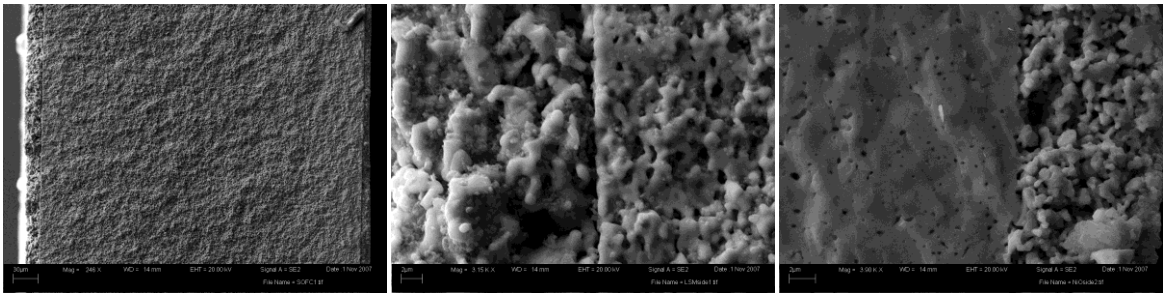


Figure 82 FEM Images of the UniCell Cross Section (Left), Cathode/Electrolyte (Center) and Electrolyte/Anode (Right) Interfaces after Electrochemical Testing

Single Sided Linear Channels

The use of a CO_2 laser was investigated to produce linear channels in a green tape. (See Figure 83) The wide aperture laser is capable of producing the channels in a single pass. The feature has rounded features that more adequately disperse the stresses throughout the sample in

comparison to the square bottom channels produced with an excimer laser. The linear nature of the channels permits laser machining of electrolyte tapes during a sheet fed operation such as tape casting, significantly reducing overall laser processing time and costs.

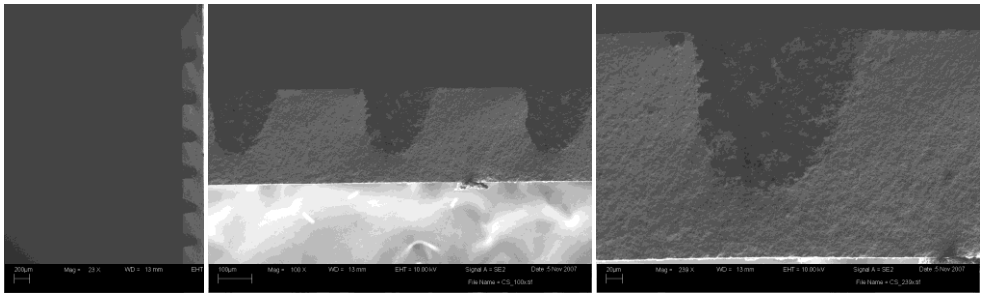


Figure 83 FEM Cross Section of Linear Channels Laser Drilled in a Green Electrolyte (23, 100 & 239 Magnifications)

Mechanical Strength Study

Preliminary Data

Preliminary data sets are not reported due to faulty testing procedure but are briefly noted. Fractures consistently initiated from the edge because the diameter of the discs was exactly or slightly less than that of the large bottom ring, resulting in high edge buckling effects due to slippage off the support during loading. Buckled edges are regions for high stress and cause premature failure, resulting in invalid tests. The sample diameters were adequately increased for the reported tests, eliminating edge buckling. The original test apparatus permitted a potential misalignment of the top and bottom rings that could have caused the load to be concentrated at select ring contact points. To reduce the error due to misalignment of the top and bottom rings a keyed mounting system was installed. The samples experienced high levels of creep during static loading of the top fixture due to its weight. A lathe was used to remove excess material and reduce overall weight without sacrificing the fixture's strength significantly.

Reported Data

The equibiaxial strength test conditions and experimental data for five 3 mol% YSZ and twenty-one 8 mol% YSZ electrolyte discs is shown in Table 11 on page 137. The force due to the weight of the top fixture was added to the applied load measured by the Instron as a static load. The failure stress for each sample was calculated utilizing Equation 28. The mean stress for the 3 mol% and 8 mol% YSZ were 968.74 MPa and 293.7 MPa, respectively. The maximum flexural strength of pure 8 mol% YSZ reported in the literature is 270 MPa.[27] ESL reports a fracture strength utilizing a three-point Modulus of Rupture to be greater than or equal to 1000 MPa.[28]

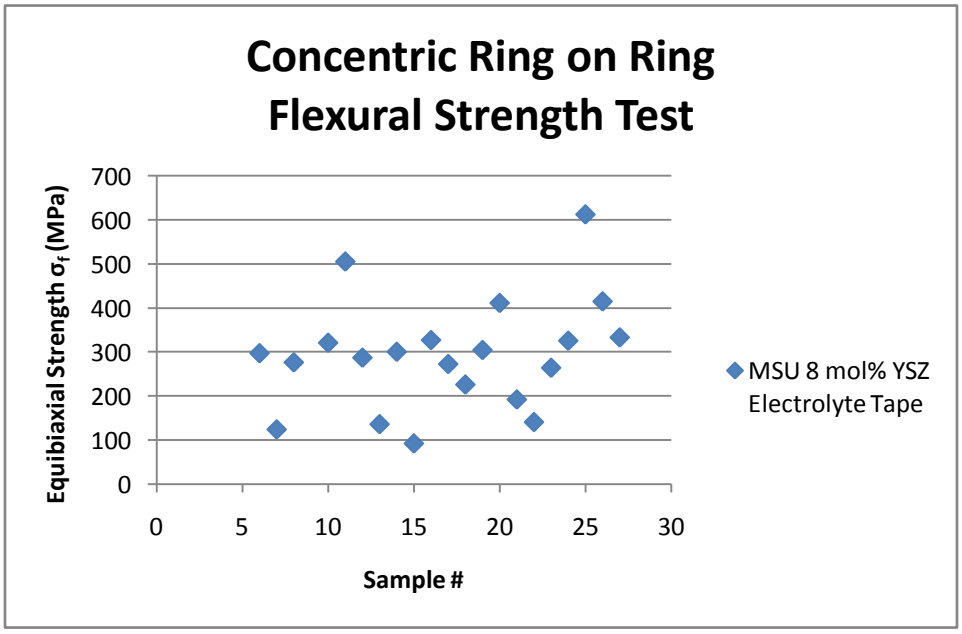


Figure 84 Monotonic Equibiaxial Flexural Strength of MSU 8 mol % YSZ Electrolyte Tape

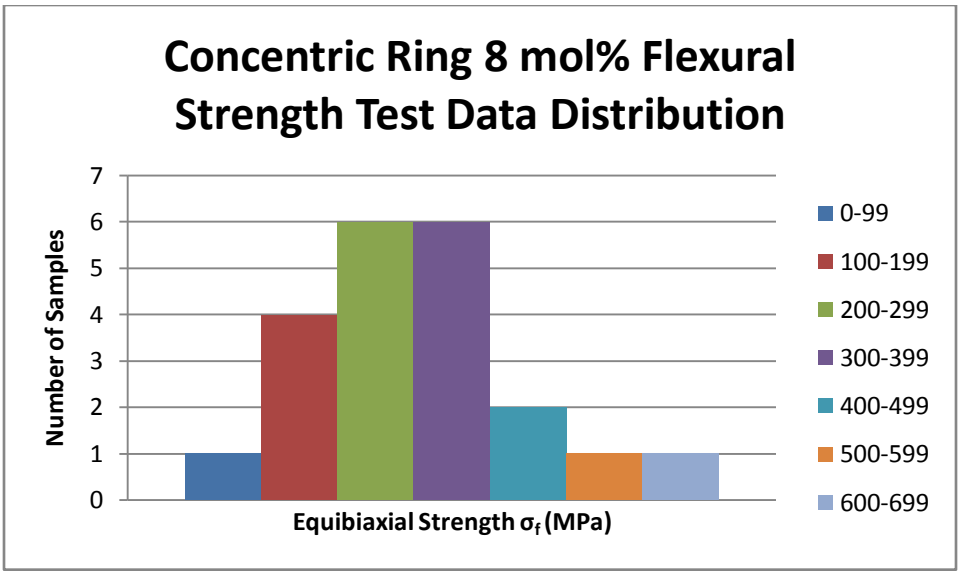


Figure 85 Concentric Ring 8 mol % Flexural Strength Test Data Distribution

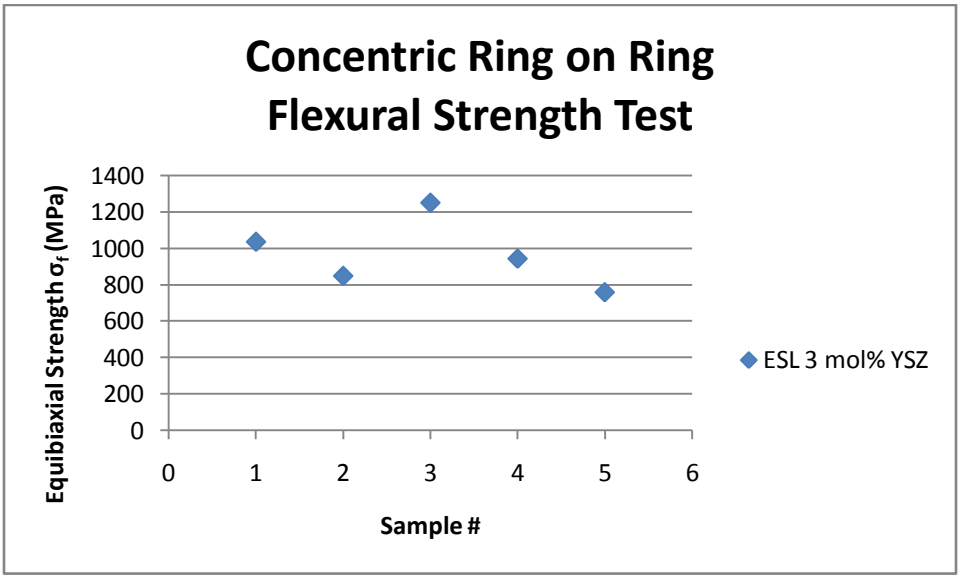


Figure 86 Monotonic Equibiaxial Flexural Strength of ESL 3 mol % YSZ Electrolyte Tape

The distribution of values for the MSU 8 mol% YSZ data set can be seen in Figure 85. The standard deviation for the 3 mol% and 8 mol% YSZ data sets is 189 MPa and 125 MPa, respectively. The large variations can be attributed to the flatness of test specimens, internal flaws and perturbations in the stress state due to non-homogeneous cross-sections. During the

punching of samples, the green tape was pulled and distorted along the edges slightly. This distortion caused a slight ripple effect along the edge during sintering, affecting the flatness profile and increasing the tangential stresses at the sample's edge. Internal flaws in the electrolyte discs tested may have caused regions from which cracks could form and propagate, causing brittle failure below the materials maximum flexural strength.

The stress strain curve for one 8 mol% YSZ specimen tested in shown in Figure 87. The initial concave slope can be correlated to creep due to the weight of the top fixture initially straining the material. Once the force applied to the specimen by the Instron dominates, the slope becomes linear as is expected with a ceramic material. The abrupt failure of the specimen during linear elastic stressing demonstrates zero plastic deformation at room temperature.

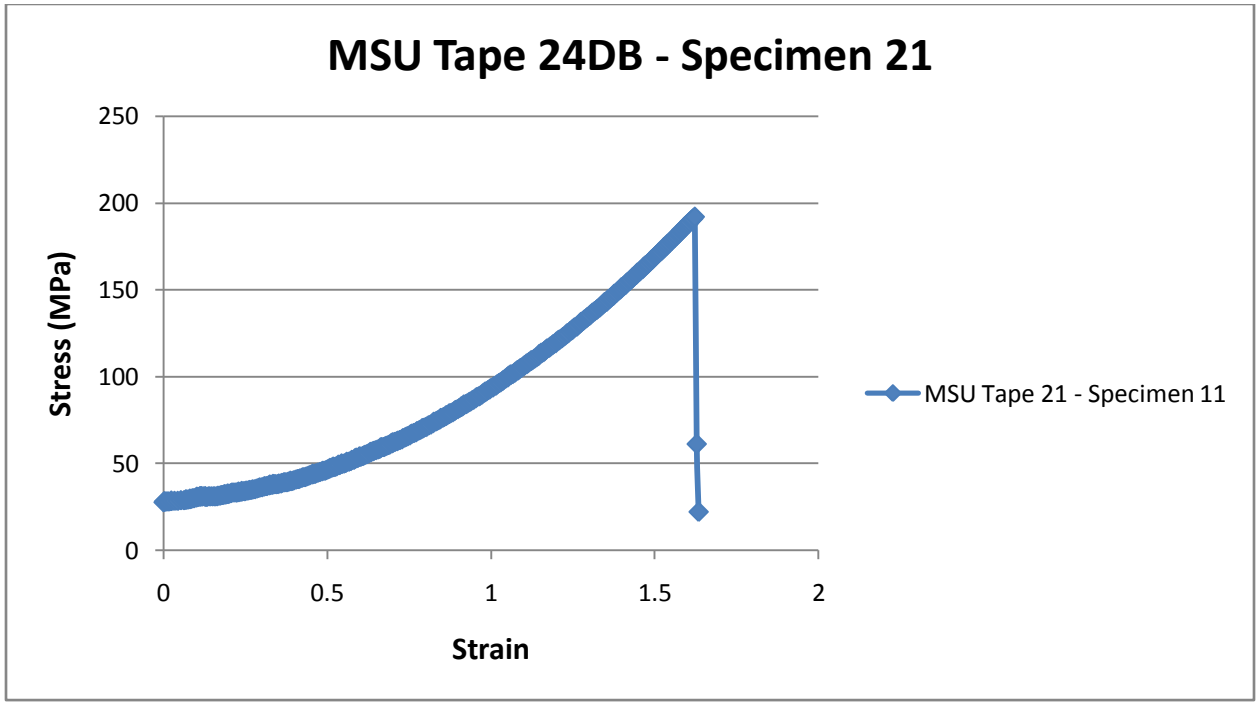


Figure 87 Stress - Strain Curve of MSU 8 mol% Electrolyte Tape
Obtained via Concentric Ring Equibiaxial Strength Test

Table 11 Equibiaxial Strength Test Conditions and Results

Concentric Ring on Ring Uniaxial Flexural Strength	
Top Fixture Mass (kg)	0.30778
Support Ring Diameter (mm)	74
Load Ring Diameter (mm)	30
Poisson's Ratio	0.22
Test Settings	
Constant Ramp Rate Through Load	2mm/min

#	Tape	Sintering Cycle	Specimen #	Diameter	Thickness	Applied Failure Force (N)	Total Failure Force (N)	Failure Stress (MPa)
1	ESL	ESL	spec 4	77.39	0.13	13.20472	16.22096	1037.33
2	ESL	ESL	spec 5	78.16	0.13	10.31744	13.33368	849.865
3	ESL	ESL	spec 6	77.54	0.14	19.69947	22.71571	1251.74
4	ESL	ESL	spec 7	78.64	0.13	11.83428	14.85053	944.633
5	ESL	ESL	spec 8	78.17	0.14	10.81597	13.83221	760.157
						Mean		1020.89
						Standard Deviation		171.877
						% Coeff of Variation		16.836
	MSU							
6	21	24 hour	spec 1	77.42	0.26	15.58455	18.60079	297.34
7	22	24 hour	spec 2	76.37	0.35	10.97237	13.98862	123.974
8	22	24 hour	spec 3	77.65	0.37	32.05962	35.07587	276.593
10	21	24 hour	spec 5	77.62	0.24	14.11631	17.13256	321.138
11	21	24 hour	spec 6	77.34	0.24	23.94052	26.95676	505.901
12	21	24 hour	spec 7	76.59	0.24	12.23814	15.25439	287.233
13	25	24 hour	spec 1	77.9	0.48	26.02635	29.04259	135.932
14	25	24 hour	spec 2	77.12	0.42	45.98395	49.0002	300.565
15	25	24 hour	spec 4	77.8	0.5	18.32228	21.33852	92.0829
16	25	24 hour	spec 6	77.01	0.47	63.7589	66.77514	327.242
17	25	24 hour	spec 7	77.61	0.52	65.28956	68.3058	272.748
18	24DB	24 hour	spec 8	76.5	0.36	23.99481	27.01105	226.138
19	24DB	24 hour	spec 9	76.74	0.32	25.76204	28.77829	304.604
20	24DB	24 hour	spec 10	76.61	0.3	31.1495	34.16574	411.691
21	24DB	24 hour	spec 11	76.26	0.34	17.42852	20.44476	192.102
22	24DB	24 hour	spec 12	76.99	0.34	12.01019	15.02644	140.73
23	24DB	24 hour	spec 13	76.61	0.42	39.96352	42.97976	264.234
24	24DB	24 hour	spec 14	76.77	0.43	52.57455	55.59079	325.821
25	24DB	24 hour	spec 15	77.2	0.39	83.20523	86.22148	613.159
26	24DB	24 hour	spec 16	76.19	0.39	55.10256	58.1188	415.178
27	24DB	24 hour	spec 17	76.78	0.33	30.48104	33.49728	333.331
						Mean		293.702
						Standard Deviation		125.439
						% Coeff of Variation		42.7095

Fuel Cell Performance Study

Fuel cell performance testing provided a comparison of the MSU UniCell and standard MSU ESCs (100 and 400 μm thick electrolytes) against a commercial Indec ESC. V-I and power density curves were obtained for all samples except the UniCell. An initial crack was created in the UniCell due to high internal stresses caused from the mismatch of layer's CTE during the co-sintering of the electrodes. A channel on the outside edge cracked and propagated through the entire channel separating from the rest of the cell. The outer portion of the cell was removed and the center of the cell that appeared to remain in tack and was electrochemically tested. During electrochemical testing of the UniCell the open current voltage of only 0.9 V showed that there initially was a slight gas leak in the cell that decreased the cell's Nernst potential. The cell idled for 75 minutes at 750 °C prior to starting a V-I curve without any significant power degradation apparent due to growth of the microscopic crack. However, after the first 8 minutes of a 60 minute V-I curve the internal crack within the UniCell catastrophically propagated in a brittle fashion, and the electrolyte no longer prevented the air and fuel from mixing. Upon the crack reaching a critical size where the gas was free to flow from one side of the cell to the other the crack stopped propagating, resulting only in a microscopic crack. After removal of the cell from the test stand the microscopic crack was not apparent to the naked eye. However a methanol drop test was performed and it was evident that there was indeed a crack within a channel that permitted the flow of gas from the anode to the cathode.

The highest power density recorded in the UniCell sample was 0.02 W/cm^2. (See Figure 88) An identical UniCell sample without the gas leakage would have demonstrated higher power

density. The lack of V-I curve results in the inability to calculate the UniCell's ASR and polarization contributions.

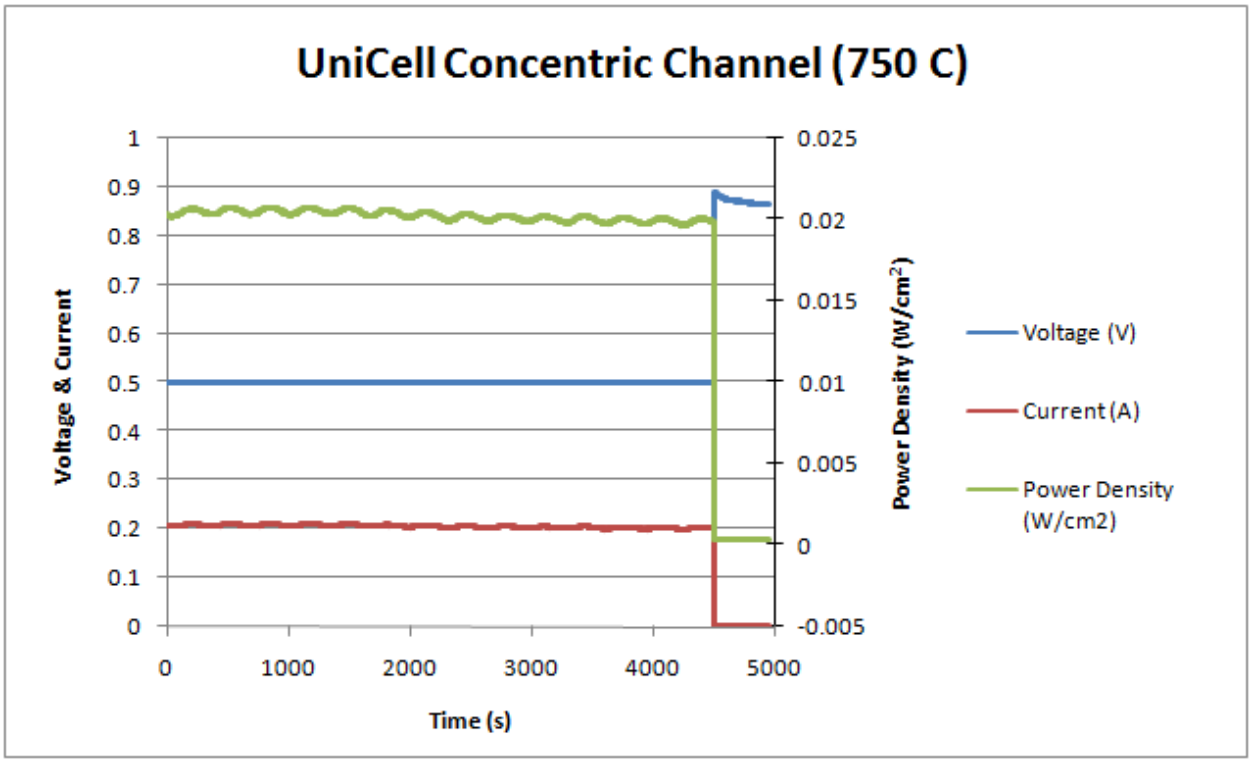


Figure 88 UniCell Power Density

The performance of all the tested cells is summarized in Table 12.

Table 12 Fuel Cell Performance Test Results

Cell	Mol% Yttria	Electrolyte Thickness (µm)	Maximum Power Density			ASR (Ω*cm²)
			(W/cm²)	Voltage (V)	Current (A)	
Tests Run at 750 °C						
Indec	3	100	0.133	0.47	4.97	2.0
MSU	8	100	0.029	0.46	0.70	7.5
MSU	8	400	0.015	0.57	0.29	30
UniCell	8	400 (250)*	0.02	0.5	0.2	NA
Tests Run at 800 °C						
Indec	3	100	0.190	0.52	6.50	1.5
MSU	8	100	0.056	0.45	1.40	4.0
MSU	8	400	0.011	0.50	0.25	30

* (250) Ionic transport distance across UniCell ~ 250 µm due to channels.

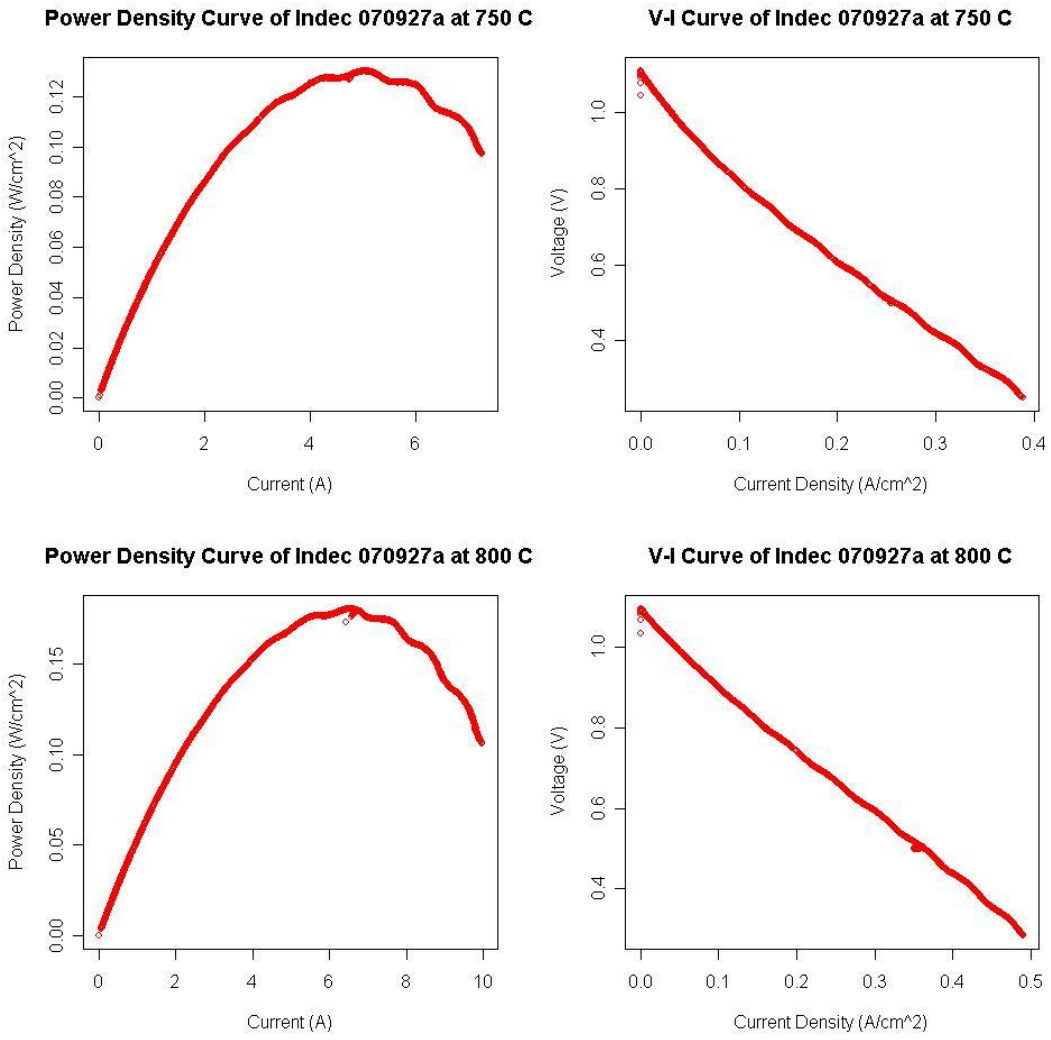


Figure 89 Commercial Indec ESC FC Performance Tests

The commercial Indec cell demonstrated a power density ranging from 0.133 to 0.190 W/cm^2 for 750 and 800 °C, respectively. The Indec V-I curves show a decrease of ASR from 2.0 to 1.5 Ω*cm^2 with an increase in temperature from 750 and 800 °C, as is expected due to the electrolyte ionic conductivity being a function of temperature. The linear shape throughout the entire V-I curve for the Indec cells show that the ohmic polarization due to the ESC design dominates the cell. (See Figure 89)

The MSU fabricated ESC tested that had a 100 micron thick electrolyte demonstrated a maximum power density of 0.056 and 0.029 W/cm^2 at 750 and 800 °C, respectively. The 750 °C V-I curve showed the cell was dominated by ohmic losses, however as the cell operating temperature was increased to 800 °C the ohmic polarization was reduced and activation polarization losses were evident. The MSU fabricated ESCs therefore require additional engineering of the cathode to minimize the activation losses demonstrated. The ASR of the cell was decreased from 7.5 to 4.0 Ω*cm^2 when increased from 750 and 800 °C, respectively.

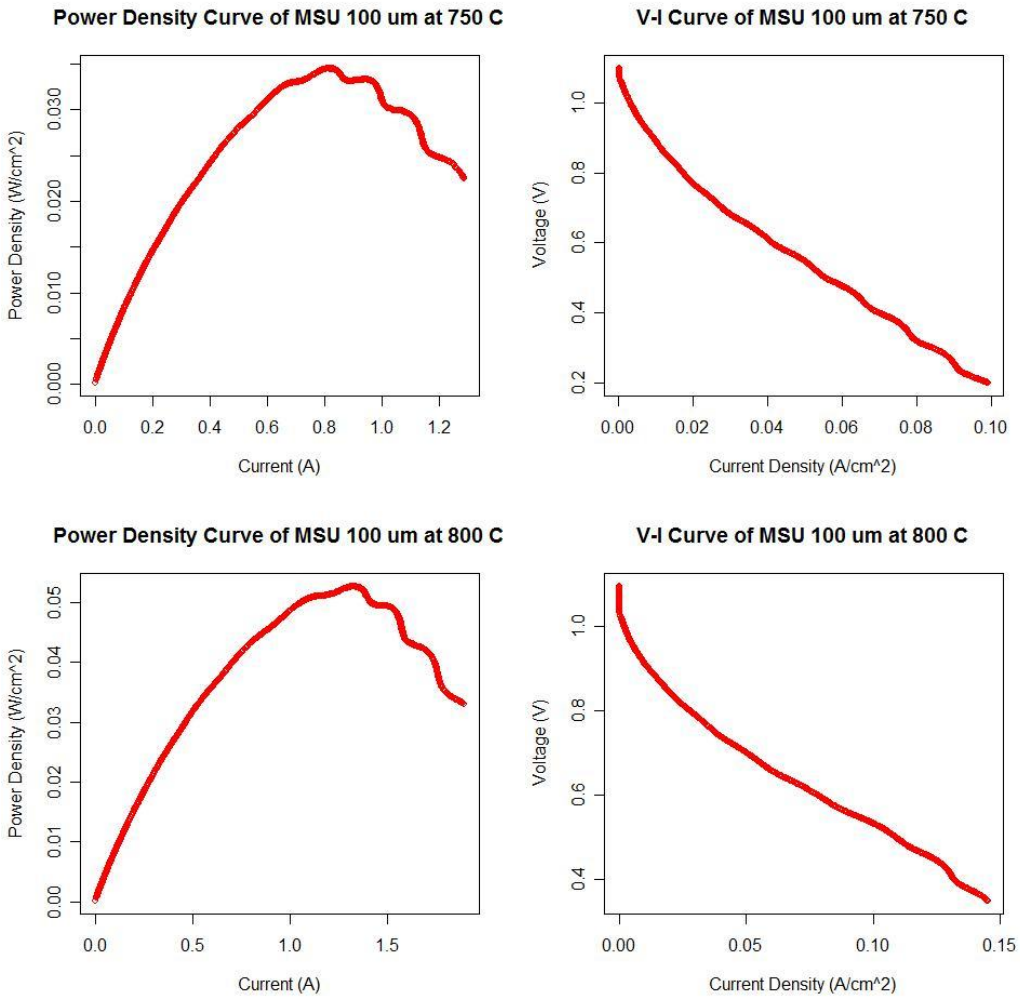


Figure 90 MSU 100 Micron Thick ESC FC Performance Tests

The MSU 400 micron thick ESC was completely dominated by ohmic polarizations due to the thick electrolyte. The ASR calculated was approximately 30 Ω*cm^2 at 750 and 800 °C. The run at 750 °C includes a bump in voltage due to test equipment malfunctioning. The 400 micron thick cell also showed significant degradation of the cell during testing, resulting in a lower power density at 800 °C compared to 750 °C.

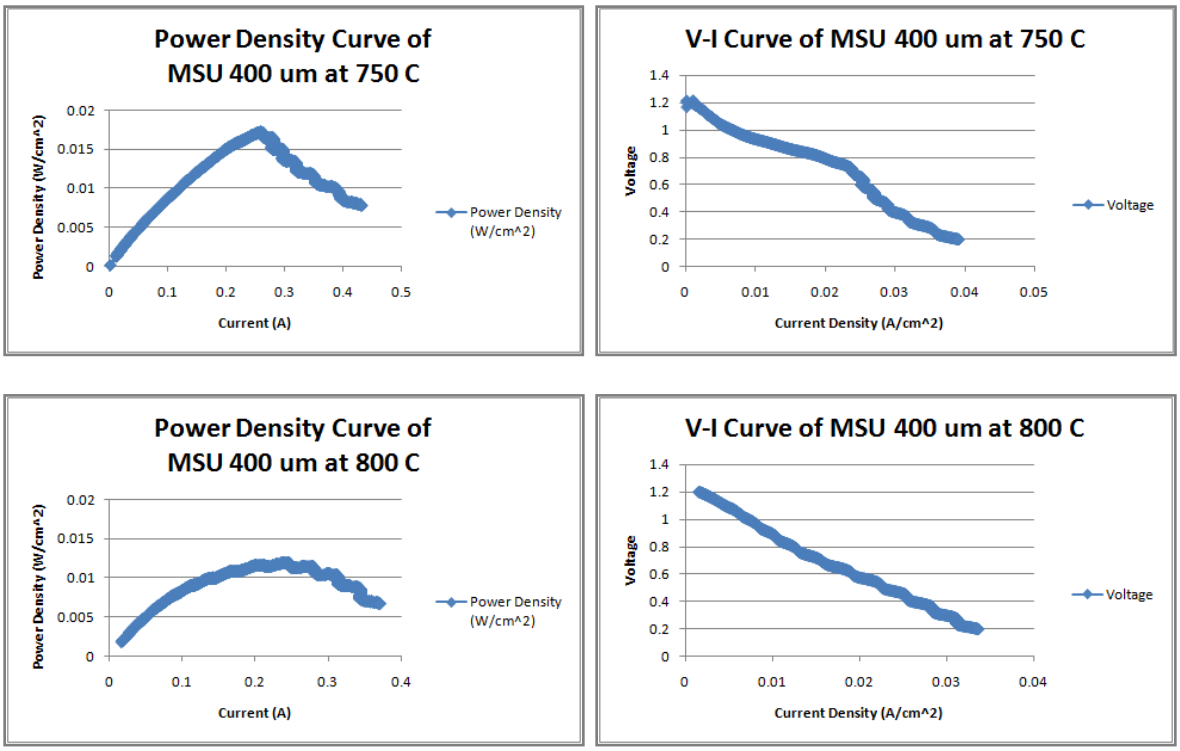


Figure 91 MSU 400 Micron Thick ESC FC Performance Tests

Linearly interpolating power density between the two different MSU fabricated cells operated at 750 °C estimated the power density output for a MSU cell with an electrolyte thickness of 250 microns to be approximately 0.0225 W/cm^2 at 750 °C. The UniCell with an ionic transport path length of 250 microns demonstrated a 0.02 W/cm^2. However, the ASR as a function of electrolyte thickness is not linear relationship, as demonstrated in Figure 9. The crack that prohibited the UniCell from reaching the true open circuit potential also reduced the

power output. Therefore initial testing shows that the UniCell performance is indeed improved (despite the decrease in open circuit potential) due to the inclusion of surface channels by comparing the performance of the maximum power density at 750 °C of the MSU 400 micron cell (0.15 W/cm^2) versus the UniCell fabricated from a 400 micron thick electrolyte (0.20 W/cm^2). A V-I curve of a new UniCell prototype is required to make conclusions on the effect of the increase in three phase boundary on the activation polarizations and ASR.

CONCLUSION

Results Summary

The particle dispersion study indicated the KD-1 dispersant effectively dispersed the YSZ in solvent at a lower concentration and for a longer duration than the MFO. However initial tape casts displayed a deficiency in binder matrix to prevent cracking due to reactions between the binder and dispersant. The replacement of the MFO eliminated cracking and resulted in a flexible tape capable of adequate amounts of plastic deformation. The use of all the milling media in the second stage resulted in the breakdown of the binder matrix after extensive milling. It was found that second stage milling periods less than or equal to 24 hours with the 250 grams of milling media did not sacrifice the binder matrix and reduced edge effects. The use of a double doctor blade and careful monitoring of the reservoir height reduced variations in the tape profile along the cast direction by eliminating welling. The green tape thickness as a function of doctor blade height can more accurately be predicted when a tape is cast without welling and edge effects present.

The smaller particle LSM and YSZ powders packed into a denser green body due to the higher ordering. The sintering of the smaller particle powders also resulted in more rapid, earlier densification and grain growth due to the higher amounts of free surface energy. The dilatometer results show the rate of linear shrinkage was solely driven by particle size and temperature, independent of ramp rate. The samples can therefore be sintered to the desired relative density by holding at a constant temperature adequate to permit interparticle diffusion. The linear shrinkage rate was calculated for the YSZ powders throughout the entire sintering range. During

sintering above 1300 and 1400 °C for the nano and micro YSZ powders, respectively, the rate of linear shrinkage was negligible and the samples only experienced grain growth. An optimum grain size of 1 micron was selected due to its balance of high ionic conductivity and mechanical strength, and was obtained via sintering the nano and micron powders to 1300 and 1500 °C. FEM images show a dense electrolyte at these temperatures that prohibits the mixing of the fuel and oxidant. The NexTech LSM displayed the desired pore microstructure that provided adequate mechanical strength without compromising gas diffusion when sintered at 1300 °C to approximately 60% relative density.

The tape sintered thickness can be accurately predicated as a function of the green tape thickness utilizing the linear relationship derived. The green tape thickness as a function of doctor blade thickness was more accurately predicted with a tape that demonstrated no welling, minimum edge effects and a consistent defect free body. A pressure on top of the tape samples during sintering of approximately 165 N/m^2 minimized cell curvature without introducing the formation of flaws due to internal stresses caused by the top surface restricting shrinkage.

Thermal gravitational analysis of the YSZ electrolyte tapes enabled the optimization of the sintering cycle to minimize the organic burnout rates. High binder burnout rates resulted in internal density gradients that shrink at different rates, causing high internal stresses. The rapid organic burnouts also introduced microstructure flaws that were sources for cracks to catastrophically propagate from in a brittle fashion common to ceramics. The burnout rates of the electrodes were measured and showed areas of concern.

Surface contouring of the YSZ electrolytes was successfully completed utilizing laser drilling in green substrates. The laser drilling of features into sintered YSZ substrates resulted in

large heat affected zones and inconsistent feature profiles. The poor thermal conductivity of the YSZ body did not permit the heat transfer from the site of laser through the bulk material without creating a HAV. The green substrate decreased the size of the HAV by decreasing the atomic bond strengths and permitting material removal at lower beam energy levels, but the high depth to hole diameter ratio restricted the plasma plume from evaporating due to the limited amount gas-surface interface area available for heat exchange. The replacement of holes with interleaved channels increased the gas-surface interface area and provided adequate heat removal to eliminate HAV. The original design goal to introduce the features in a thin electrolyte was relaxed from 150 to 400 micron thick layers to improve the substrate strength during prototyping. An excimer laser resulted in cleaner features due to the decreased pulse lengths that permitted additional heat exchange between pulses. However, the CO_2 laser demonstrated no HAV and reduced machining time by a magnitude of 10. The channel bottoms were slightly rounded with the CO_2 laser, eliminating high stress concentration regions. The linear channels machined by a CO_2 laser can be retrofitted into a tape cast sheet fed system, enabling inline surface contouring of the green tapes.

Concentric ring strength testing accurately predicted the maximum flexural strength at ambient temperatures for 3 and 8 mol% YSZ discs. All samples failed in a brittle fashion, exhibiting zero plastic deformation as expected for sintered ceramics. The 8 mol% YSZ samples provide a baseline for evaluating the effect of surface contouring electrolyte discs on the maximum flexural strength. Due to the destructive nature and limited prototype samples the UniCell maximum flexural strength was not calculated.

Fuel cell electrochemical performance testing compared the UniCell power density with that of an MSU fabricated ESC with an electrolyte the same thickness absent of surface contouring. The initial test results for the UniCell showed a crack was present, decreasing the Nernst Potential of the cell by permitting the mixing of small quantities of fuel and oxidant without electrochemical conversion. Prior to obtaining a V-I curve the UniCell crack propagated. Initial power densities suggest ohmic losses are decreased by the introduction of the interleaved channels but further testing is required to make any decisive conclusions. The MSU fabricated cells displayed activation losses in the thin electrolyte sample operated at high temperatures where ohmic polarization no longer dominated, suggesting engineering of the anode catalyst is required. The V-I curves for the cells confirmed ASR is a function of electrolyte thickness that can be minimized by decreasing the ionic path length.

Future Considerations & Recommendations

Due to the extensive nature of developing a method from scratch for fabricating the UniCell several process and testing improvements are recommended below. To take the fabrication to commercial production several procedures must be carefully controlled through the addition of new processing techniques. However prior to extensive investments can be made in the optimization of the processes the proof of concept fuel cell electrochemical test results must be expanded upon and the design must be optimized. It is recommended to produce a batch in excess of 5 samples of green tape sheets at a thickness of 400 microns that can be laser machined. Produce 7.5 cm square electrolytes with interleaved linear channels utilizing the CO_2 laser system, apply the electrodes via airbrushing and co-sinter the sample under pressure.

Compare the electrochemical performance versus identical tape samples without surface contouring. It is recommended to monitor the exit gas flow compositions to determine the fuel utilization of the cells.

The optimization of the cell channel design and electrolyte thickness to minimize the ionic path length should then be completed. It is recommended to consider utilizing state of the art modeling software commercially available from ANSYS, Fluent and through SECA to calculate thermo elastic stress, analyze the effects of geometry on fuel cell performance and calculate mechanical strength of various geometries prior to bringing the samples to production. The results of the highest performing designs should be verified experimentally.

The optimization of the fabrication processes to produce the electrolyte substrate should continue. Due to the detrimental environmental impacts associated with xylene and ethanol, the replacement of the electrolyte slurry which utilizes hazardous organic solvents with aqueous based slurry should be considered. Monitoring the viscosity of the tape slurries prior to tape casting would allow the fabrication of tapes with a more consistent thickness profile from batch to batch by reducing welling and edge effects. The use of a vibration table or mixing bar during de-airing of the slurry would permit the release of air more completely in a less volatile fashion.

When the tape casting process parameters have been solidified utilizing a doctor blade system with a fixed blade gap would minimize contributions to inconsistencies in tape thickness from human error in setting the blade height. Automatic control and monitoring of the slurry level in the doctor blade reservoir will ensure a consistent hydrostatic pressure. In turn a constant shearing stress will be applied to the slurry as the moving Mylar sheet pulls the slurry into a thin tape. The doctor blade could be replaced with a moving leveling blade; where low

viscosity slurry is poured onto the static mylar and then the leveling blade is moved over top to remove the excess material and flatten the slurry left behind into the desired thin film shape. This would require the development of a new slurry recipe but would permit the manufacturing of short sections of thin films with a more consistent profile.

The distortion due to edge tearing during cutting the electrolyte discs from the green tape caused a slight ripple effect along the edge during sintering, affecting the flatness profile and increasing the tangential stresses at the sample's edge. Future studies should address this issue by utilizing a sharp, automated punching process or sending out green tape samples to a machinist to laser cut coupons out of the tape.

The use of nanoscale particle powders to further improve green tape density and permit one step sintering of the entire UniCell to reduce processing time and costs should be investigated. The sintering of the electrolyte layers at lower temperatures that have reasonable linear shrinkage rates should be considered, enabling the precise control of grain growth and density at low temperatures where LSM does not react with the YSZ. The linear shrinkage rates of the anode and cathode materials as a function of temperature should be measured via dilatometer analysis. This would permit the minimization of differing sintering shrinkage rates. The inclusion of pore formers in the electrodes would enable the dwelling at high temperatures where complete densification of the electrolyte is obtained but a porous electrode microstructure is preserved.

The potentially negative effects of high concentrations regions of oxygen ion travel through the UniCell channels should be investigated via FEM and EDS analysis. A study of the

effect of the different channel designs on the distribution of gas flow during operation may prove to further improve cell efficiencies.

Since SOFC ceramics fail in a brittle fashion, increasing the sample batch size from the concentric ring tests will improve the statistical significance of data reported. It is recommended to increase the batch size, report the uniaxial strength data and estimate the Weibull distribution parameters for advanced ceramics in accordance with ASTM test method C 1239-00. The further decrease in test fixture weight will reduce the effects of creep during testing. The abrupt failure of the specimen during linear elastic stressing demonstrated zero plastic deformation at room temperatures. However it is expected for ceramics to behave different at elevated temperatures similar to operating conditions. The concentric ring test fixture manufactured of stainless steel would permit high temperature testing.

The UniCell design is very conducive to high performance electrolytes, included ceria and gallate materials as well as electrode infiltration. The UniCell architecture combined with these more advanced materials, may prove a more dramatic route for this concept.

BIBLIOGRAPHY

1. U.S. Department of Energy. *Fuel Cell Handbook (Seventh Edition).* Morgantown, West Virginia : U.S. Department of Energy, November 2004.

2. Electric Power Research Institute. [Online] Electric Power Research Institute, 2003. http://www.epri.com.

3. Wkipedia. Solid oxide fuel cell. *Wikipedia.* [Online] Wikimedia Foundation, Inc., October 2007. http://en.wikipedia.org/wiki/Solid_oxide_fuel_cell.

4. Sammes, Nigel. *Fuel Cell Technology - Reaching Towards Commercialization.* London, UK : Springer-Verlag London Limited, 2006.

5. Todd, Ben. *fuelcellknowledge.org.* [Online] 2003. http://www.fuelcellknowledge.org.

6. *Nonmetallic Materials.* Swiss Federal Institute of Technology - Zurich. ETH-Zurich.

7. Siemens AG. The Principle Behind the Technology. *Siemens Power Generation.* [Online] 2007. http://www.powergeneration.siemens.com/products-solutions-services/products-packages/fuel-cells/principle-behind-technology/.

8. J-W. Kim, A Virkar, K-Z. Fung, K. Mehta and S.C. Singhal. 1999, Journal of the Electrochemical Society, p. 146.

9. Versa Power Systems. Solid Oxide Fuel Cell Technology. [Online] 2007. http://www.versa-power.com/.

10. NexTech Materials. NextCell Advanced Electrolyte Planar Cell. *fuelcellmaterials.com.* [Online] May 2007. http://www.nextechmaterials.com/files/NextCell.pdf. 10-10101-100.

11. Acumentrics. About Fuel Cell Energy, Tubular, and Solid Oxide Generator Systems. *Acumentrics.com.* [Online] 2007. http://www.acumentrics.com/knowledge-center-about-fuel-cells.htm.

12. Siemens AG. Benefits and Features. [Online] 2007. http://www.powergeneration.siemens.com/products-solutions-services/products-packages/fuel-cells/benefits-features/.

13. Transportation Technology R&D Center. Argonne Transportation - TuffCell. *Argonne National Laboratory.* [Online] January 28, 2004. http://www.transportation.anl.gov/research/fuel_cells/tuffcell.html.

14. Adaptive Materials Inc. *AMI - Adaptive Materials Inc.* [Online] 2007. http://www.adaptivematerials.com/.

15. Richard E. Mistler and Eric R.Twiname. *Tape Casting Theory and Practice.* Westerville, Ohio : The American Ceramic Society, 2000.

16. Reed, James S. *Introduction to the Principles of Ceramic Processing.* Alfred, New York : John Wiley & Sons, Inc., 1988.

17. *Non-Aqueous Dispersion Properties of Pure Barium Titanate for Tape Casting.* K.R. Mikeska and W.R. Cannon. 305-21, s.l. : Colloids and Surfaces, 1988, Vol. 29.

18. ProSciTech. Material Safety Data Sheet Butvar B-98. *proscitech.com.* [Online] September 18, 2006. http://www.proscitech.com/catalogue/msds/c060.pdf.

19. Clark-MXR, Inc. Micrmachining Handbook. *Ultrafast lasers for science, industry and micromachining.* [Online] 2007. http://www.cmxr.com/industrial/handbook/index.htm.

20. PhotoMachining, Inc. Contract Laser Microvia Drilling Services. [Online] 2007. http://www.photomachining.com.

21. Ikonics Corporation. Phtoresist Machning Process. *High Precision Machining - Ikonics Industrial Solutions.* [Online] 2007. http://www.ikonicsindustrial.com/process_summary.php.

22. Inframat Advanced Materials LLC. 8 mol% Yttria Stabilized Zirconia (YSZ) Powder Superfine Grade. *Inframat Advanced Materials.* [Online] 2007. http://www.advancedmaterials.us/4039OR-8601.htm.

23. —. 8 mol% Yttria Stabilized Zirconia (YSZ) Nano Powder, 99.9+%, 30-60 nm. *Inframat Advanced Materials.* [Online] 2007. http://www.advancedmaterials.us/4039ON-8601.htm.

24. NexTech Materials. Lanthanum Strontium Manganite (Document No.: 10-10101-101). *Fuel Cell Materials.* [Online] April 2006. http://www.fuelcellmaterials.com/pdf/LSM%205-9-20091.pdf.

25. *C1499-05 Standard Test Method for Monotonic Equibiaxial Flexural Strength of Advanced Ceramics at Ambient Temperature.* ASTM International. 2006, Annual Book of ASTM Standards. Volume 15.01.

26. *Enhanced specific grain boundary conductivity in nanocrystalline yttria stabilized zirconia.* P. Mondal, A Klein, W. Jaegermann, H. Hahn. 1999, Solid State Ionics, pp. 331-339.

27. U.S. Department of Labor. Ethyl Alcohol. *OSHA.* [Online] 2007. http://www.osha.gov/dts/sltc/methods/organic/org100/org100.html.

28. —. Occupational Safety and Health Guideline for Xylene. *OSHA.* [Online] 2007. http://www.osha.gov/SLTC/healthguidelines/xylene/recognition.html.

29. Technical Chemical Company. Material Safety Data Sheet. *technicalchemical.com.* [Online] 12 28, 2001. http://www.technicalchemical.com/msds/2312-6.pdf.

30. Omega Protein, Inc. Material Safety Data Sheet. *buyomegaprotein.com.* [Online] May 26, 2005. http://www.buyomegaprotein.com/pdf/MSDS.pdf.

31. International Programme on Chemical Safety. Concise International Chemical Assessment Document 17 - Butyl Benzyl Phthalate. *Chemical Safety Information from Intergovernmental Organizations.* [Online] 2007. http://www.inchem.org/documents/cicads/cicads/cicad17.htm#PartNumber:2.

32. MarkeTech International. Zirconium Oxide Ceramic - Zirconia, Y2O3 Stabilized. *MatWeb Material Porperty Data.* [Online] 2007. http://www.matweb.com/search/DataSheet.aspx?bassnum=C5MT38&ckck=1.

33. ESL Electro-Science. Partially Stabilized Zirconia Tape 42000. *ElectroScience.* [Online] 2007. http://electroscience.com/pdf/42000.pdf.

34. Hummel, Rolf E. *Electronic Properties of Materials - Second Edition.* Ann Arbor, MI : Edwards Brothers, Inc., 1993.

35. William D. Callister, Jr. *Materials Science and Engineering An Introduction - Fourth Edition.* s.l. : John Wiley & Sons, Inc., 1997.

36. Singhal, S.C. Zirconia Electrolyte Based Fuel Cells. *The Electrochemical Society.* [Online] February 2002. https://www.electrochem.org/dl/ma/201/pdfs/1087.pdf.

37. *C1161-02c Standard Test Method for Flexural Strength of Advanced Ceramics at Ambient Temperature.* ASTM International. 2006, Annual Book of ASTM Standards. Volume 15.01.

38. *C1239-06a Standard Practice for Reporting Uniaxial Strength Data and Estimating Weibull Desitbution Parameters for Advanced Ceramics.* ASTM International. 2006, Annual Book of ASTM Standards. Volume 15.01.

39. *Grain size-dependent electrical properties of rutile (TiO2).* Demetry, Chrysanthe. 1999, Solid State Ionics, pp. 271-279.

40. *Effect of characteristics of YSZ powders on fabrication of anode-supported solid oxide fuel cells.* Yong Jun Leng, Siew Hwa Chan, Khiam Aik Khor, San Ping Jiang, Philip Cheang. 2003, Journal of Power Sources, pp. 26-34.

41. *C1211-02 Standard Test Method for Flexural Strength of Advanced Ceramics at Elevated Temperatures.* ASTM International. 2006, Annual Book of ASTM Standards. Volume 15.01.

42. *Fuel Composition and Diluent Effect on Gas Transport and Performance of Anode-Supported SOFCs.* Virkar, Yi Jianf and Anil V. 2003, Journal of Electrochemical Society, pp. A942-A951.

43. *Physical properties of 8 mol% Ceria doped yttria stabilized zirconia powder and ceramic and their behaviour during annealing and sintering.* A.A. Burkaemskiy, D. Barrier, G. Modolo. 2006, Journal of the European Ceramic Society, pp. 1507-1515.

44. *Correlation between slurry rheology, green density and sintered density of tape cast yttria stabilized zirconia.* Amit Mukherjee, B. Maiti, A. Das Sharma, R.N. Basu, H.S. Maiti. 2001, Ceramics International, pp. 731-739.

45. *Fabrication and Performance of Thin-Film YSZ SOFCs between 600 and 800 Celsius.* C. Wang, W.L. Worrell, S. Park, J.M. Vohs and R.J. Gorte. s.l. : U.S. National Energy Technology Laboratory, 1999. Joint Fuel Cell Technology Review Conference.

46. *Sinter behaviour of LSM.* J.A.M. van Roosmalen, E.H.P. Cordfunke and J.P.P. Huijsmans. 1993, Solid State Ionics, pp. 285-293.

47. *Powder diespersion and aqueous tape casting of YSZ-NiO composite.* S. Ramanathan, K.P. Krishnakumar, P.K. De, S. Banerjee. 2004, Journal of Materials Science, pp. 3339-3344.

48. Sorrell, Sugihara and Nowotny. *Materials for energy conversion devices.* Boca Raton, FL : Woodhead Publishing Limited, 2005.

49. Steven J. Visco, Craig Jacobson and Lutgard C. De Jonghe. *Thin-Film Fuel Cells.* Berkeley, CA : Lawrence Berkeley National Laboratory.

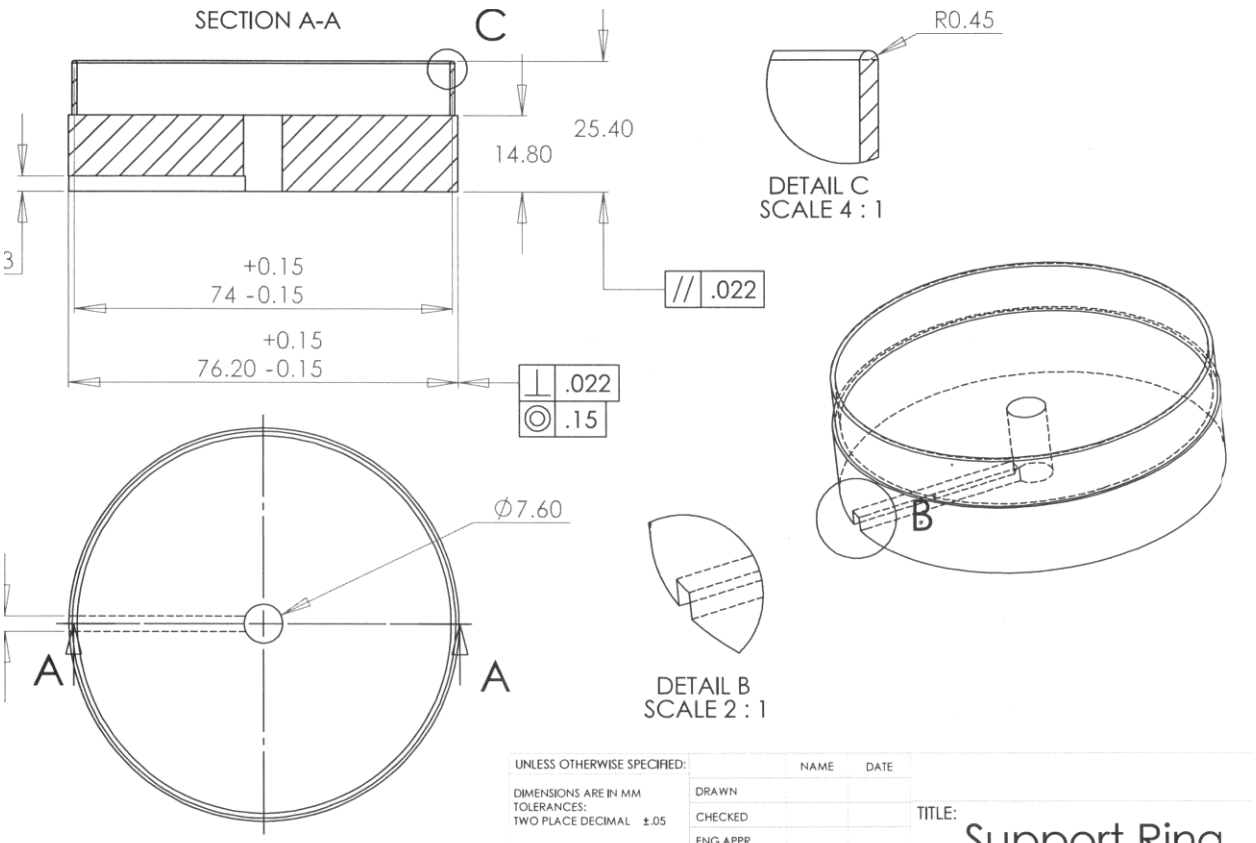
50. US Fuel Cell Council. Fuel Cell Glossary - Second Edition. *US Fuel Cell Conference Web Site.* [Online] May 2000. http://www.usfcc.com/Glossary2.pdf.

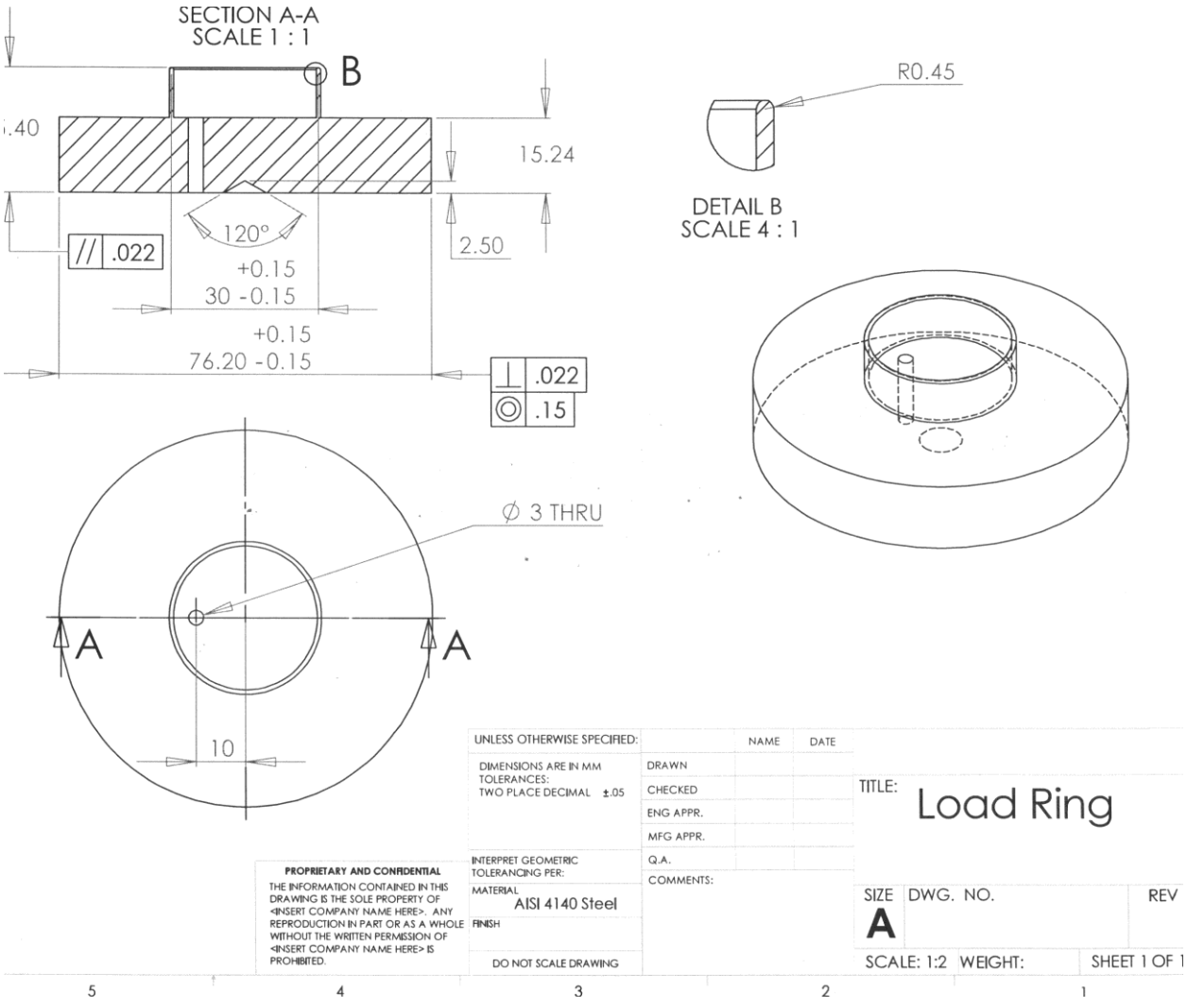
51. *Fuel cell materials and components.* Haile, Sossina M. 2003, Science Direct Acta Materialia, pp. 5981-6000.

52. Carsten Systems Machine Ltd. Tape Csting Systems. [Online] October 7, 2005. http://www.carstensystemsandmachine.com/.

APPENDIX A:

CONCENTRIC RING MACHINE SHOP DRAWINGS


SECTION A-A
C
25.40
14.80
3
+0.15
74 -0.15
+0.15
76.20 -0.15
// .022
.022
.15
Ø7.60
A
A
R0.45
DETAIL C
SCALE 4 : 1
B
DETAIL B
SCALE 2 : 1
UNLESS OTHERWISE SPECIFIED:
DIMENSIONS ARE IN MM
TOLERANCES:
TWO PLACE DECIMAL ±.05
INTERPRET GEOMETRIC TOLERANCING PER:
MATERIAL
AISI 4140 Steel
FINISH
DO NOT SCALE DRAWING
NAME
DATE
DRAWN
CHECKED
ENG APPR.
MFG APPR.
Q.A.
COMMENTS:
TITLE:
Support Ring
SIZE
A
DWG. NO.
REV
SCALE: 1:1
WEIGHT:
SHEET 1 OF 1
PROPRIETARY AND CONFIDENTIAL
THE INFORMATION CONTAINED IN THIS DRAWING IS THE SOLE PROPERTY OF <INSERT COMPANY NAME HERE>. ANY REPRODUCTION IN PART OR AS A WHOLE WITHOUT THE WRITTEN PERMISSION OF <INSERT COMPANY NAME HERE> IS PROHIBITED.
5
4
3
2
1


SECTION A-A
SCALE 1 : 1
B
.40
15.24
120°
2.50
// .022
+0.15
30 -0.15
+0.15
76.20 -0.15
.022
.15
R0.45
DETAIL B
SCALE 4 : 1
∅ 3 THRU
A
A
10
UNLESS OTHERWISE SPECIFIED:
NAME
DATE
DIMENSIONS ARE IN MM
TOLERANCES:
TWO PLACE DECIMAL ±.05
DRAWN
CHECKED
ENG APPR.
MFG APPR.
Q.A.
COMMENTS:
INTERPRET GEOMETRIC TOLERANCING PER:
MATERIAL
AISI 4140 Steel
FINISH
DO NOT SCALE DRAWING
PROPRIETARY AND CONFIDENTIAL
THE INFORMATION CONTAINED IN THIS DRAWING IS THE SOLE PROPERTY OF <INSERT COMPANY NAME HERE>. ANY REPRODUCTION IN PART OR AS A WHOLE WITHOUT THE WRITTEN PERMISSION OF <INSERT COMPANY NAME HERE> IS PROHIBITED.
TITLE:
Load Ring
SIZE
A
DWG. NO.
REV
SCALE: 1:2
WEIGHT:
SHEET 1 OF 1
5
4
3
2
1